

Fractures, Faults, and Hydrothermal Systems of  
Puna, Hawaii, and Montserrat, Lesser Antilles

by

Catherine Lewis Kenedi

Department of Earth and Ocean Sciences  
Duke University

Date: \_\_\_\_\_

Approved:

\_\_\_\_\_  
Emily Klein, Co-Supervisor

\_\_\_\_\_  
Peter Malin, Co-Supervisor

\_\_\_\_\_  
Alan Boudreau

\_\_\_\_\_  
Lincoln Pratson

Dissertation submitted in partial fulfillment of  
the requirements for the degree of  
Doctor of Philosophy in the Department of Earth and Ocean Sciences  
in the Graduate School of Duke University

2010

**ABSTRACT**

**Fractures, Faults, and Hydrothermal Systems of  
Puna, Hawaii, and Montserrat, Lesser Antilles**

**by**

**Catherine Lewis Kenedi**

**Department of Earth and Ocean Sciences  
Duke University**

**Date:\_\_\_\_\_**

**Approved:**

\_\_\_\_\_  
Emily Klein, Co-Supervisor

\_\_\_\_\_  
Peter Malin, Co-Supervisor

\_\_\_\_\_  
Alan Boudreau

\_\_\_\_\_  
Lincoln Pratson

**An abstract of a dissertation submitted in partial fulfillment of  
the requirements for the degree of  
Doctor of Philosophy in the Department of Earth and Ocean Sciences  
in the Graduate School of Duke University**

**2010**

**Copyright by  
Catherine Lewis Kenedi  
2010**

## **Abstract**

The focus of this work is to use geologic and geophysical methods to better understand the faults and fracture systems at Puna, in southeastern Hawaii, and southern Montserrat, in the Lesser Antilles. The particular interest is understanding and locating the deep fracture networks that are necessary for fluid circulation in hydrothermal systems. The dissertation first presents a study in which identification of large scale faulting places Montserrat into a tectonic context. Then follow studies of Puna and Montserrat that focus on faults and fractures of the deep hydrothermal systems.

The first chapter consists of the results of the SEA-CALIPSO experiment seismic reflection data, recorded on a 48 channel streamer with the active source as a 2600 in<sup>3</sup> airgun. This chapter discusses volcaniclastic debris fans off the east coast of Montserrat and faults off the west coast. The work places Montserrat in a transtensional environment (influenced by oblique subduction) as well as in a complex local stress regime. One conclusion is that the stress regime is inconsistent with the larger arc due to the influence of local magmatism and stress.

The second chapter is a seismic study of the Puna hydrothermal system (PHS) along the Kilauea Lower East Rift Zone. The PHS occurs at a left step in the rift, where a fracture network has been formed between fault segments. It is a productive geothermal field, extracting steam and reinjecting cooled, condensed fluids. A network of eight borehole seismometers recorded >6000 earthquakes. Most of the earthquakes are very small (< M.2), and shallow (1-3 km depth), likely the result of hydrothermal fluid reinjection. Deeper earthquakes occur along the rift as well as along the south-dipping fault plane that originates from the rift zone.

Seismic methods applied to the PHS data set, after the initial recording, picking, and locating earthquakes, include a tomographic inversion of the P-wave first arrival data. This model indicates a high seismic velocity under the field that is thought to be an intrusion and the heat source of the hydrothermal system. A shear wave splitting study suggested the PHS fracture system is largely oriented rift-parallel with some orthogonal fractures. Shear wave splitting data also were used in a tomographic inversion for fracture density. The fracture density is high in the PHS, which indicates high permeability and potential for extensive fluid circulation. This has been confirmed by high fluid flow and energy generation. The high fracture density is consistent with the interpretation of a transfer zone between the rift segments where a fracture mesh would be expected. In Puna the transfer zone is a relay ramp.

The results from the PHS are used as an example to examine the proposed hydrothermal system at St. George's Hill, Montserrat. In southern Montserrat, hot springs and fumaroles suggest a deep hydrothermal system heated by local magmatism. A magnetotelluric study obtained resistivity data that suggest focused alteration under southeastern Montserrat that is likely to be along fault segments. Several faults intersect under SGH, making it the probable center of the hydrothermal system. At Puna, and also Krafla, Iceland, where faults interact is an area of increased permeability, acting as a model to be applied to southern Montserrat. The conclusion is that in both Puna and Montserrat large faults interact to produce local areas of stress transfer that lead to fracturing and permeable networks; these networks allow for high-temperature hydrothermal circulation.

**Dedication**

For Chris, the past and the future, and for Peter, the future. Thank you for helping me live in the present.

## Contents

Abstract.....	iv
List of Figures .....	x
Acknowledgements .....	xv
Introduction.....	1
1. Contrasts in morphology and deformation offshore Montserrat: New insights from the SEA-CALIPSO marine cruise data .....	7
1.1 SEA-CALIPSO reflection profiling and the geologic/tectonic setting .....	7
1.2 Data collection and processing .....	11
1.3 Volcaniclastic fans and faulting off the eastern shelf .....	11
1.4 Exposed and buried faults off the western shelf .....	15
1.5 Tectonic synthesis and relation to onshore deformation and volcanism .....	17
2. Microseismicity and 3-D Mapping of an Active Geothermal Field, Kilauea Lower East Rift Zone, Puna, Hawaii .....	20
2.1 Introduction .....	21
2.2 Geologic context .....	23
2.3 Network setup.....	25
2.4 Local seismology .....	26
2.5 Shear wave splitting.....	29
2.6 Double difference relocation .....	33
2.7 Seismic tomography.....	34
2.8 Discussion .....	37
2.9 Conclusions .....	38

<b>3. Applications from the fracture dominated, high-temperature hydrothermal system of Puna, Hawaii, for St. George's Hill, Montserrat .....</b>	<b>40</b>
3.1 Introduction .....	40
3.1 A confirmed fracture dominated hydrothermal system at Puna, Hawaii.....	44
3.1.1 Geologic setting.....	44
3.1.2 Geologic structure .....	48
3.1.3 Faults at Puna .....	49
3.1.4 Seismicity and fracture mapping at Puna Hydrothermal System .....	50
3.1.4.1 Shear Wave Splitting Analysis.....	51
3.1.4.2 Fracture Density .....	53
3.1.5 Transfer zone at Puna .....	56
3.1.6 Puna hydrothermal system in context: Krafla, Iceland .....	59
3.1.6.1 Seismicity .....	61
3.1.6.2 Fractures.....	62
3.2 Evidence for a Fracture Dominated Hydrothermal System at St. George's Hill, Montserrat .....	64
3.2.1 Geologic and tectonic setting.....	64
3.2.2 Seismicity and fracture mapping at St. George's Hill .....	70
3.2.2.1 Seismicity.....	71
3.2.2.2 Resistivity.....	73
3.2.3 3-D Tomography .....	75
3.2.4 Permeability at fault intersections: Transfer Zones.....	77
3.2.4.1 Probable location of hydrothermal system on Montserrat.....	78



<b>Appendix A: 3-D Seismic velocity tomography of Montserrat from the SEA-CALIPSO offshore/onshore experiment.....</b>	<b>80</b>
Introduction.....	81
The seismic tomography experiment .....	81
Data.....	82
Seismic tomography method.....	82
Results .....	83
Discussion .....	84
Acknowledgments.....	85
References .....	85
Figure captions.....	88
<b>References .....</b>	<b>93</b>
<b>Biography .....</b>	<b>102</b>

## List of Figures

Figure 1 (continued): A. Tectonic model of Lesser Antilles, modified from Feuillet et al. (2002). Faults and extension directions described in Feuillet et al. (2002). White arrows: Motion between North American, South American, and Caribbean plates (DeMets et al., 2000; Weber et al., 2001). White half arrows: Sinistral and dextral motion along the trench. Thin black arrow: GPS movement at Aves Ridge. ....	10
Figure 2 (continued): Seismic reflection profiles and annotated interpretations of radial Lines 7 and 9. Solid lines: Strong reflectors and sediment packages. Short dashed lines: Faults. Thin dashed line: Bottom multiple. Intersection with Lines 2 and 23 indicated at top. ....	13
Figure 3 (continued): Seismic reflection profiles and annotated interpretations of Lines 2 and 23, parallel to the east coast. Description as in Fig. 2. Intersection with Lines 7 and 9 indicated at top. Vertical lines at the top: Boundaries between the major volcanic centers. ....	15
Figure 4 (continued): Seismic reflection profiles and annotated interpretations of Lines 15 and 21, off the west coast. Description as in Fig. 2. ....	17
Figure 5: Topographic map of the Puna Borehole network area. Red squares mark station locations. The black dot is Puna Geothermal Venture. The large black rectangle is the target zone for the 3-D inversion. The small black rectangle is the area of good ray coverage shown in detail in the 3-D plots. ....	24
Figure 6: A. Inside of the 3-component borehole seismometer. Top geophone is vertical; middle and bottom geophones are horizontal and orthogonal. Geophones are Figure 6 (continued) the small cylinders; the large conical shapes are gimbaled counterweights to control for borehole tilt and contribute to damping. 6B. Installation of a seismometer into a standard diameter HQ borehole. Top half of the instrument is a tiltmeter. ....	25
Figure 7: Map view of Puna seismic array stations and earthquakes. Black triangles are seismic stations. Earthquake locations are marked by dots colored according to depth. The size of the dots indicates the magnitude, ranging from M-0.2 to M2.0. ....	27
Figure 8: Plot of the number of earthquakes of a given magnitude according to the Gutenberg-Richter relationship. The slope of the plot represents the B-value, 1.48. The value of $R = -0.997$ . ....	28

Figure 9: The upper diagram shows the original seismogram, with no shear wave splitting identifiable. The lower diagram shows the seismogram after 56° rotation. Shear wave splitting is visible.....	29
Figure 10: Rose diagrams indicating the fast shear wave polarization directions. Each bin is 5 degrees wide. The length of the bin reflects the number of shear wave splits in the bin. A total of 1500 shear wave splitting observations were made, most of them by stations close to the center of the earthquake cluster. Black triangles are seismic stations. Earthquake locations are marked by dots colored .....	30
Figure 11: Polar coordinate projection (azimuth and angle) of shear wave splitting polarization. Each circle represents all shear wave splitting observations for one station. The circumference of each circle represents a 45° incident angle from the vertical. Azimuth marks the direction toward the hypocenter. The location of each line represents the azimuth and the incident angle of one shear wave splitting observation. The orientation of each line is the direction of the fast shear wave polarization for that observation. Stations P01, P02, P03, P04, and P05 are plotted in the correct geographical location. ....	32
Figure 12: Map and Cross section views of events that have been double difference relocated. Figures (12A) and (12B) are both map views with 12B showing a detailed view of the area. Figure (12B) shows the area used to generate the projected cross sections in figures (12C) and (12D). ....	33
Figure 13: Hit-count map of the target zone. Images are horizontal slices at depths of 1.5, 2.0, 2.5, and 3.0 km. Colors indicate log10 number of rays that pass through each 100m x 100m x 100m volume. The thin line within each map marks the PGV lease.....	35
Figure 14: The 3-D tomographic inversion for P-wave velocity presents data in horizontal slices at 1.5, 2, 2.5, and 3 km depth. The figures show Vp perturbation, the change from the average velocity at each depth. Reds represent slower velocities and blues represent faster velocities. X and Y axes are km from a chosen origin.....	36
Figure 15: The 3-D tomographic inversion for Vp/Vs. Horizontal slices are at 1.5, 2, 2.5, and 3 km depth. Red represents slower ratios and blues represent higher ratios. X and Y axes are km from a chosen origin. ....	37
Figure 16. Hill (1977) mesh model for earthquake swarms and Sibson (1996) model for fracture permeability. The model includes interlinked shear, extensional, and extensional-shear fractures. Diagram represents an extensional normal-fault stress	

regime when upright, a compressional thrust-fault regime when viewed sideways, and a strike-slip regime in plan view..... 42

Figure 17: A. Satellite view of the island of Hawaii. Mauna Loa is the most massive volcano in the world, and Kilauea has grown on its southern flank. Note the rift systems of Mauna Loa and Kilauea, visible by the pattern of lava flows emanating from them. Image modified from <http://coralreefs.wr.usgs.gov/hawaii.html>..... 45

Figure 18 (continued): Geologic map of the LERZ around the PHS. Pink flows are emplaced since 1790. Orange units are 200-400 years old. Green units are 400-750 years old. Blue units are 750 to 1500 years old. Black circles/ellipses mark craters, cones, and fissures. Normal fault symbols mark normal faults. The yellow star is the location of the Puna Geothermal Ventures power plant. Red triangles are seismic stations. Modified from Moore and Trusdell (1991)..... 48

Figure 19: Earthquake depth and size along the Kilauea East Rift Zone at the Puna Hydrothermal System. The dashed line is the LERZ. Red squares are seismic stations. Colored dots are earthquakes; color indicates depth. Black dots are deeper than 5.5 km. The black shape represents the lease of the power plant. This figure has been updated from Fig. 7 in Chapter 2 to include earthquakes through June, 2009..... 51

Figure 20: Cartoon illustrating the mechanism of shear wave splitting. .... 52

Figure 21: Rose diagrams of shear wave splitting data at the seismograph stations. Colored dots are earthquakes; color indicates depth. Stations 6 and 7 (see Figure 19) are not included due to lack of shear wave splitting data. This figure has been updated from Fig. 10 in Chapter 2 and to include earthquakes through June, 2009..... 53

Figure 22: Plots of crack density based on shear wave splitting tomography. Red is higher fracture density; blue is lower fracture density. X and Y axis labels are kilometers from an assigned origin. The black outline is the lease of the Puna Geothermal Venture power station. .... 55

Figure 23. A. Cartoon illustrating the structure of a relay ramp. The fading circle illustrates the area between faults that is the most affected by fault-related stresses. B. A photograph of a relay ramp on the Hilina Fault System. From Parfitt and Peacock (2001). .... 57

Figure 24. DEM of the lower east rift zone. In blue is the lease boundary of the Puna Geothermal Venture. The primary fault dips SE from the ERZ. In red are contours marking depth of the antithetic fault as documented by drilling.....	58
Figure 25. Geologic and structural model of the Krafla hydrothermal system. Caldera faults have a NW-SE trend while faults within the volcanic zone have a N to NNE trend. Welded tuff and rhyolite/dacite deposits occur at the margins of the caldera. From Onacha (2006). ....	61
Figure 26. The proposed structural cross section of the Krafla hydrothermal system. Subsurface NW-SE trending faults occur in older rocks, and younger fissure swarms trend in the NE-SW direction. The fissures are associated with dyke swarms that control lateral movement of hydrothermal fluids. From Onacha (2006).....	63
Figure 27 (continued): A. Tectonic model of Lesser Antilles, modified from Feuillet et al. (2002). Faults and extension directions described in Feuillet et al. (2002). White arrows: Motion between North American, South American, and Caribbean plates (DeMets et al., 2000; Weber et al., 2001). White half arrows: Sinistral and dextral motion along the trench. Thin black arrow: GPS movement at Aves Ridge.....	67
Figure 28: Oblique aerial view of Montserrat from the SW. The grey land cover is ash, mud, and pyroclastic debris from multiple dome collapse and lahar events since 1995. Dashed black lines are faults. BVF Belham Valley Fault. RHF Richmond Hill Fault. SGH is St. George's Hill, GH is Garibaldi Hill, RH is Richmond Hill. ....	68
Figure 29: View of southern Montserrat from the west. Curving lines illustrate the ridges descending from the tops of the hills. CH is Centre Hills, BVF is Belham Valley Fault, SGH is St. George's Hill, GH is Garibaldi Hill, SHV is Soufriere Hills Volcano, RH is Richmond Hill, RHF is Richmond Hill Fault. ....	70
Figure 30: Seismicity under southern Montserrat, August 1995. Clusters occurred under SHV, in a NE linear trend from SHV, and under SGH. Depths range from ~2-6 km. ....	72
Figure 31: Resistivity map from Magnetotelluric survey. 11A. Resistivity at 1000 m depth; 11B. Resistivity at 4000m depth. Red indicates lower resistivity and blue indicates higher resistivity. Straight lines indicate faults. From Ryan et al. (2009).....	74
Figure 32: A. Vp tomography results as perturbation from the average velocity at each depth. Blue is faster velocities; red is slower velocities. Map view at 2 km depth. B, C. 3D isosurfaces of velocity anomalies. The blue surfaces define anomalies that are >6% faster	

than average. The red surfaces define anomalies that are >6% slower than average. B is the map view, C is viewed from the southwest. ....76

## **Acknowledgements**

Above all, I thank Peter Malin, whose absolute patience and faith in me made this possible.

I thank Eylon Shalev for his assistance and kindness. I am grateful for Eylon's presence at each step of the way, for field work, paper writing, and insightful discussions.

To the people of Montserrat with gratitude for welcoming us, now the second generation of scientists basing careers on efforts to understand their ever-active volcano. I greatly appreciate the generosity, humor, and friendliness I've received in my visits. Thanks to the staff of the Montserrat Volcano Observatory for assistance and patient cooperation.

A big thank you to the staff of the Puna Geothermal Venture for being gracious and helpful hosts. Special thanks to Bill Teplow and Mike Kaleikini for generously sharing previous work and data.

Thanks to the staff of the Hawaiian Volcano Observatory, especially Jim Kauahikaua, Frank Trusdell, Paul Okubo, and Don Swanson, for cooperation and helpful discussions.

Many thanks to Barry Voight and Steve Sparks for their patience and mentoring.

Much gratitude to the professors and scientists whose love of their fields and excellence in teaching got me started on the track of geology and volcanology: Jelle Zeilinga de Boer, Wesleyan University; John Brady, Bob Burger, Bob Newton, and Brian White, Smith College; Mike Rhodes, University of Massachusetts; Don Swanson, Hawaiian Volcano Observatory.

Thank you to friends: Annie Zaino for everything from shear wave picking to writing advice to home-saving help; Stephen Onacha for encouragement and help with higher math; Beatriz Cabrera Martin for years of help beyond the call of duty.

Finally, I thank my parents, Gus and Mary Ann Lewis, and parents-in-law, Anna Kenedi Gorga and Raymond Gorga, for endless tolerance and support, and bottomless love.



## **Introduction**

Fractures, including faults, represent one physical manifestation of stresses in the Earth. Fractures form when rock is forced beyond its elastic limit, i.e. its ability to deform, and breaks. In faults the rocks on either side of the fault are displaced with respect to each other. In this dissertation the particular focus is what happens where faults interact, both at fault intersections and the region between adjacent faults. The stresses where faults interact are localized and different from the regional stress system but at all scales, stresses can be assessed based on fault orientation.

On a large scale, faults can be used to fit an area into its tectonic context. In the case of Montserrat, Lesser Antilles, this dissertation and other works have used on- and offshore faulting to interpret Montserrat as part of a transtensional environment within the regional extensional setting (Feuillet et al., 2010; Kenedi et al., 2010b). On the island scale, a large individual fault, the Belham Valley Fault, BVF, dominates southern Montserrat and has affected the pattern of volcanism, aligning vents within the Soufriere Hills volcano complex. The BVF also has uplifted local blocks, establishing the current island morphology. At a more local scale, one of the blocks, St. George's Hill, is at the junction of smaller faults that may indicate a fracture network and high temperature hydrothermal system at depth. At each scale, faults are the critical element from which to base the structural and stress interpretation.

The region in between adjacent faults is called the transfer zone, where stresses from each fault affect the central area. Transfer zones are considered highly permeable due to the fracture mesh that occurs as a result of imposed stresses. Again, the size and manifestation of the transfer zone depends on the scale of the faulting. At the regional

scale, Montserrat is in a transfer zone between two large fault systems. The manifestation of the large scale fracturing appears to be increased magmatism. At the local scale, I propose a fracture system in the transfer zone of southeastern Montserrat based on the findings in Puna, Hawaii. In Puna the transfer zone takes the form of a relay ramp and is highly permeable, as seen in the reliable circulation of hydrothermal fluids used to generate geothermal energy.

Montserrat and Hawaii are located in different tectonic settings but both support high-temperature hydrothermal systems. In the case of the Puna hydrothermal system (PHS), sub-surface temperatures and the ability of the hydrothermal system to maintain heat and fluid circulation have been well documented as a result of industrial efforts associated with the production of geothermal electricity. However, the deep fracture geometry has not been well understood, and attempts to expand production have failed as a result. At Montserrat the hydrothermal system has been studied using the fluids in hot springs and fumeroles (Chiodini et al., 1996), and field mapping has identified fault traces (Chiodini et al., 1996; Harford et al., 2002). But again, the fracture geometry at depth has not been analyzed.

A fracture network that enables fluid circulation is as critical an element of a hydrothermal system as are heat and fluid. Hydrothermal fluids are mineral rich, so both cooling and degassing results in crystal precipitation and fracture infilling. Fractures may be maintained or opened by fault activity, making proximity to faults a critical factor for long-lived fluid circulation (Curewitz and Karson, 1997; Rowland and Sibson, 2004).

The geologic structure at the PHS is dominated by a rift step in which two normal fault segments are offset; it has been documented that such a gap is dominated by

stresses from the interacting faults that cause increased fracturing (Curewitz and Karson, 1997). The resulting fracture network determines local fracture permeability and thus hydrothermal circulation. One goal of this dissertation is mapping subsurface fractures in hydrothermal systems, as has been tested at Puna and at Krafla, Iceland, and as a recommendation for further testing at St. George's Hill, Montserrat.

This work, among other studies, has shown that mapping subsurface fractures can be done by recording, locating, and analyzing microearthquake data (Kenedi et al., 2010a; Lucas et al., 2010; Onacha, 2006; Rial, 2005; Shalev et al., 2008). The most effective seismic array includes borehole seismometers, as the rock at depth insulates the seismometer from surface noise and makes it possible to see and locate microearthquakes from the seismogram (Kenedi et al., 2008). The most important element of using the seismogram for further analysis is clear identification of both the P- and the S-wave for each event at each station. Reducing noise increases the ability to identify these phases and thus increases the accuracy of earthquake location.

Following earthquake location, microearthquake analysis with respect to fracture mapping includes shear wave splitting data. Due to variation in elastic properties between rock and fluid, shear waves split into fast and slow moving waves when travelling through aligned fluid-filled fractures. Because the fast wave travels parallel to the fractures, shear wave splitting results can be used to map the fracture orientation (Crampin, 1993). In addition, the shear wave splitting result includes the time delay between the fast and the slow shear wave. The delay increases with the number of fractures so is related to fracture density; shear wave splitting data are tomographically inverted to obtain fracture density (Lou and Rial, 1997; Shalev et al., in preparation).

Fracture density is an indicator of permeability in rock (REF). It is a critical factor in evaluating a hydrothermal system for use in geothermal energy production, which requires high fluid flow to overcome the fundamental lack of efficiency of the generation process (on average 10-25%).

The other tomographic inversion method used at the Puna hydrothermal field inverted P-wave arrival data to show variations in seismic velocity (Shalev et al., 2008). The initial velocity information was checked against earthquake locations from the Hawaiian Volcano Observatory seismic array but the large majority of earthquakes recorded by the borehole seismic array were not recorded by surface seismometers. Thus a new velocity model was established (Shalev et al., 2008). The main finding was a zone of high seismic velocity under the PHS, which is attributed to the presence of an intrusion. The intrusion is now associated both with a dacitic magma (Teplov et al., 2008) and with the heat source for the PHS.

Below, I briefly summarize each chapter and provide background for the work.

The work at Montserrat, described in Chapter 1, was initially focused on the active volcano, Soufrière Hills (SHV). I participated in a multi-institution, onshore-offshore seismic experiment designed to image the magmatic structure under the volcano (Voight et al., 2010, and works in the special section of Geophysical Research Letters, "SEA-CALIPSO Arc Volcano Imaging on Montserrat"). During the experiment, the research vessel that towed the airgun also towed a hydrophone streamer that collected seismic reflection data. These data provided information about the structure of volcanic debris fans as well as faulting offshore (Kenedi et al., 2010b). The offshore faulting data, combined with previously published work, enables us to better constrain

the locally shifting stress system. The stresses appear to be under the influence of both regional tectonics and the local magmatic system, as revealed in faulting onshore Montserrat.

The seismic array at Puna, described in Chapter 2, was installed as a monitoring network for seismicity in the hydrothermal system. This provided a remarkable scientific opportunity to record earthquakes at an active geothermal field where there had never been a thorough seismic study. We installed borehole seismometers that could record much smaller earthquakes than would be possible with surface seismometers. Whereas the existing seismic array, operated by the Hawaiian Volcano Observatory, could locate earthquakes  $\geq M2.5$ , the borehole network obtained useable data for earthquakes  $\geq M-0.5$  (Kenedi et al., 2010a). These data have been used to resolving fault geometries at depth as well as to identify a possible magma intrusion and heat source for the hydrothermal system.

Chapter 3 consists of a comparison of the two field areas and an examination of the indicators that support the presence of a hydrothermal system on Montserrat. Here I discuss the fault geometry at both Puna and near St. George's Hill (SGH). The Puna hydrothermal system (PHS) lies within a step between large normal faults, and I present evidence that the step consists of a structural feature called a relay ramp. The region near SGH involves several faults, at least one of which is a connector between the two largest faults. In both cases, the fault interaction indicates a subsurface fracture mesh that supports local permeability and fluid circulation.

This dissertation includes work in two tectonic settings, using a variety of geophysical methods. The next step will be to quantify the relationship between fractures

and permeability. The goal of the dissertation is a better understanding of the local deep fracture networks that affect global hydrothermal systems.

# **1. Contrasts in morphology and deformation offshore Montserrat: New insights from the SEA-CALIPSO marine cruise data**

During the December 2007, SEA-CALIPSO experiment we collected seismic reflection profiles offshore of Montserrat. Off the east coast, we imaged deep fans of volcanoclastic debris from three volcanoes progressively active from ~2 Ma to present. Near-shelf sedimentation rates of 8-9 cm/ka are approximated following cessation of local volcanic activity. The fans were deposited on sediments with apparent dips towards the ESE-trending Montserrat-Havers fault system (MHFS) in southern Montserrat. The MHFS encloses the Soufrière Hills volcano, has elevated crustal blocks at Roche's Bluff, St. Georges Hill, and Garibaldi Hill, and extends off the west coast. In two western profiles, the N-dip of a fault supports a N-dip interpretation for a major component of MHFS, the Belham Valley fault. We propose that local deformation is affected by stress redistributions consistent with a right-stepping, sinistral *en-echelon* fault system, but the interplay of transtension and magmatism has resulted in complex and evolving stress regimes.

## ***1.1 SEA-CALIPSO reflection profiling and the geologic/tectonic setting***

The December 2007, SEA-CALIPSO experiment (**S**eismic **E**xperiment with **A**irgun-source – **C**aribbean **A**ndesitic **L**ava **I**sland **P**recision **S**eismo-geodetic **O**bservatory) at Montserrat, Lesser Antilles, was an onshore-offshore seismic study of the crust and magmatic system under Montserrat and the Soufrière Hills volcano (SHV) (Paulatto et al., 2010; Shalev et al., 2010; Voight et al., 2010). The experiment included a 48 channel, 600 m streamer, and 2600 in<sup>3</sup> airgun seismic reflection survey that explored

local submarine deposits and faults and expanded knowledge based on previous seismic and bathymetric studies (e.g. Feuillet et al., 2001; Feuillet et al., 2002). We present key results from our survey and discuss their implications on the local tectonic and volcanic interactions.

Three andesitic volcanic centers dominate Montserrat: Silver Hills (~1-2 Ma), Centre Hills (~0.4 – 1 Ma), and Soufrière Hills - South Soufrière Hills (~0.3 Ma to present) (Fig. 1) (Harford et al., 2002; Le Friant et al., 2008). Since 1995, SHV activity has included dome building and collapses that produced onshore and offshore pyroclastic and debris flows and deposits (Deplus et al., 2001; Le Friant et al., 2009; Le Friant et al., 2004; Loughlin, 2010; Trofimovs et al., 2006).



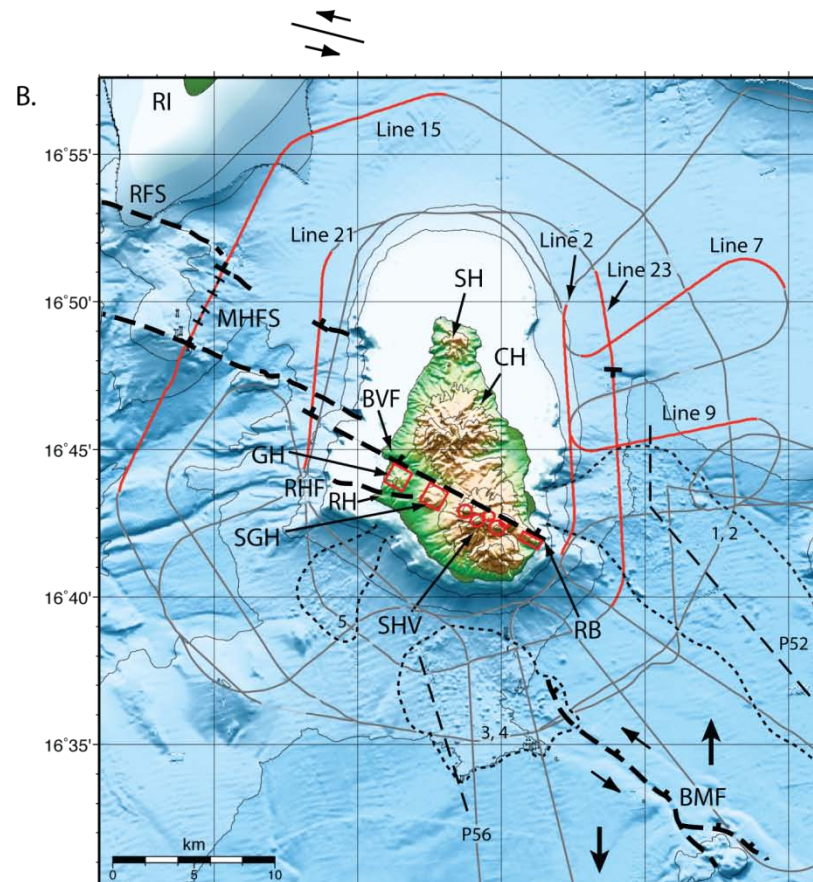
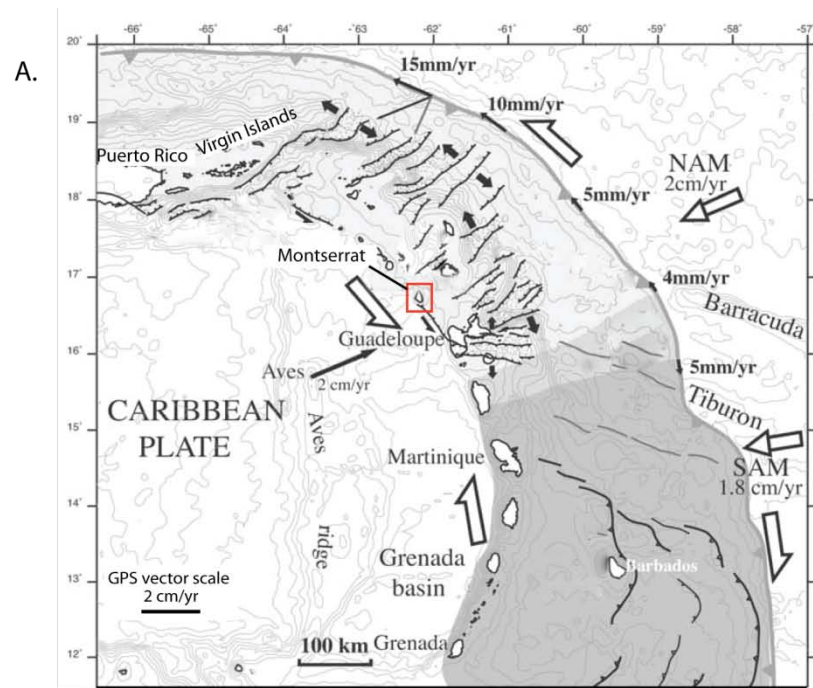


Figure 1.

Figure 1 (continued): A. Tectonic model of Lesser Antilles, modified from Feuillet et al. (2002). Faults and extension directions described in Feuillet et al. (2002). White arrows: Motion between North American, South American, and Caribbean plates (DeMets et al., 2000; Weber et al., 2001). White half arrows: Sinistral and dextral motion along the trench. Thin black arrow: GPS movement at Aves Ridge.

B. Montserrat bathymetry and tectonic model. Grey curved line: Track of the RRS James Cook. Red Lines (7, 9, 2, 23, 15, 21) are discussed in this paper. Red circles: Volcanic centers. Red squares: Tectonic uplifts. Black fault symbols: Normal faults from profiles, apparent dip as indicated. Thick dashed lines: Major fault of the fault systems, including BVF and possible extension to RB. Large black arrows: Extension direction (Feuillet et al., 2001). Dotted lines: Gravity flow deposits 1 – 5 of (Le Friant et al., 2004). Thin dashed lines: Cross sections (P52, P56) along deposits from (Le Friant et al., 2004). The fault to the north inferred from 1985-1986 Redonda earthquake mechanisms (Feuillet et al., 2002; Girardin et al., 1991). BMF, Bouillante-Montserrat fault system; BVF, Belham Valley fault; CH, Centre Hills; GH, Garibaldi Hill; MHFS, Montserrat-Havers fault system; RB, Roche's Bluff; RFS, Redonda fault system; RH, Richmond Hill; RHF, Richmond Hill fault; RI, Redonda Island; SGH, St. Georges Hill; SH, Silver Hills; SHV, Soufrière Hills Volcano. Bathymetry map from Institut de Physique du Globe de Paris and M. Paulatto, NOCS.

On and west of SHV, young andesitic domes (<300 ka) and structurally uplifted areas (Harford et al., 2002) are aligned due to normal faulting as part of the extensional Montserrat-Havers fault system (MHFS) (Feuillet et al., 2010). The MHFS includes an ESE-trending lineament interpreted as the Belham Valley fault (BVF) (Harford et al., 2002) (Fig. 1B). Normal faulting continues to the SE of Montserrat with a right step to the Bouillante-Montserrat fault system (BMF) (Fig. 1B). Extension with ~N-S trend is prevalent in the region, which Feuillet et al. (2010) suggests is accommodated as oblique shear along a series of *en echelon*, mainly NE-dipping normal fault systems including the BMF, MHFS, and the Redonda fault system (RFS) (Fig. 1). We propose that these systems also accommodate minor local shear that has resulted in rotation of older sediments and deformation of the footwall of the BVF and related faults.

## ***1.2 Data collection and processing***

As part of the SEA-CALIPSO experiment, the RRS James Cook collected offshore reflection profiles (Fig. 1B). The eight GI airgun array was fired every 60 s with streamer signals sampled every 2 ms. The shot interval was 139 m. The data were bandpass filtered between 4 Hz and 64 Hz, stacked, and migrated using sediment velocities from semblance analysis. A low source frequency and long shot interval were selected to maximize the onshore tomography data and were thus less optimal for the reflection study. Six sections are shown in Figs 2 – 4 (red profile lines, Fig. 1B). Time to depth conversions used an average sediment velocity of 2200 m/sec (Paulatto et al., 2010).

## ***1.3 Volcaniclastic fans and faulting off the eastern shelf***

The reflection profiles off the eastern shelf are dominated by chaotic sediment packages, interpreted as accumulations of volcaniclastic debris. In the profiles, debris is visible as eastward tapering lenses that extend offshore from Silver Hills and Centre Hills (Lines 7 and 9; Figs. 1B and 2). The debris from Silver Hills (Line 7) extends ~10 km from the shelf and overlies strata that step down towards Montserrat. From Centre Hills as well (Line 9), debris onlaps layered sediments that dip westward, from 1.5 s two-way travel time (twt) at km 12 to 2.2 s twt at km 5 (Fig. 2). The apparent dip (Line 9) and downward fault-step pattern (Line 7) towards the island are consistent with either island subsidence or with rotation on the hanging wall of the MHFS faults (Figs. 1,2).

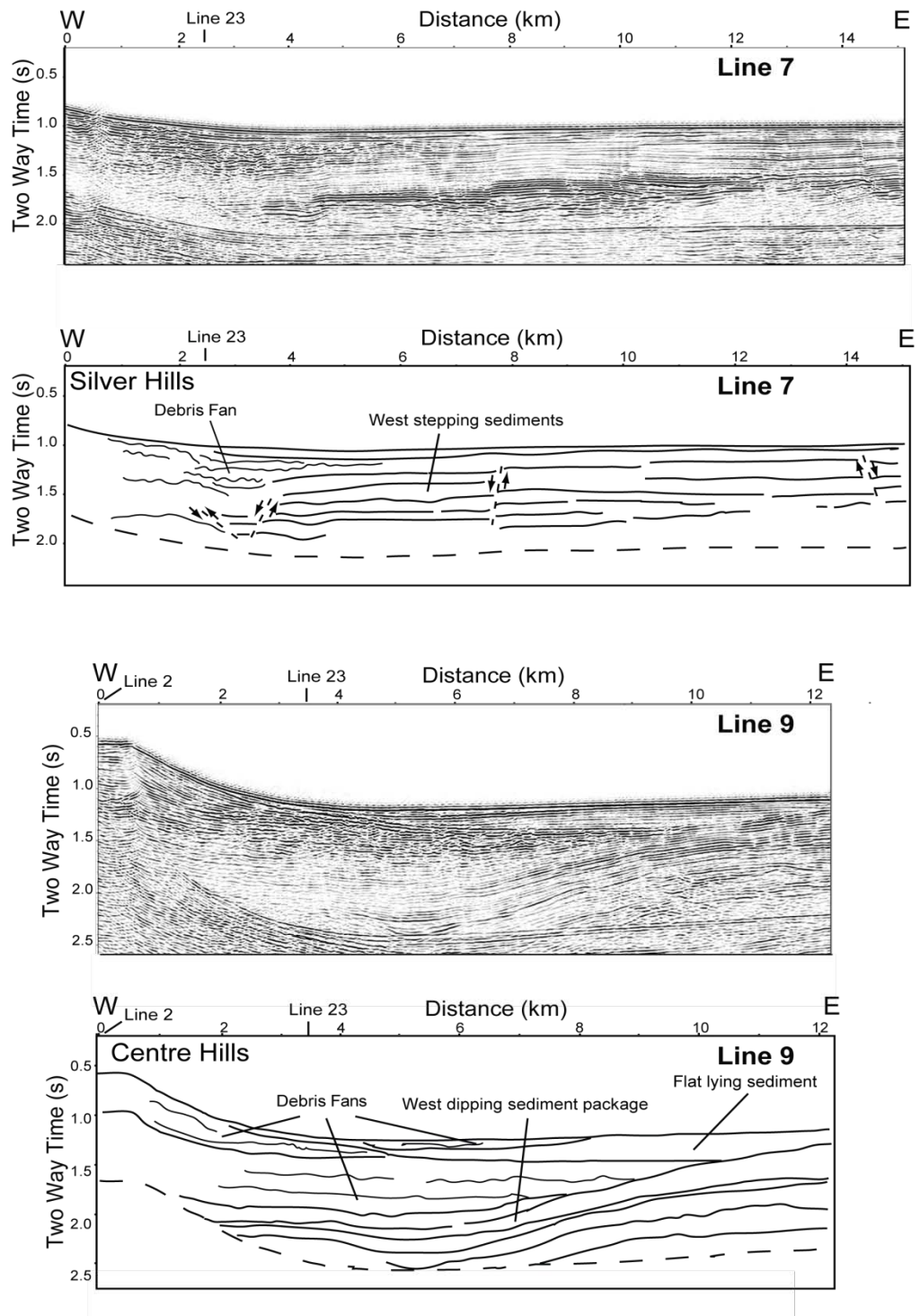


Figure 2.

**Figure 2 (continued): Seismic reflection profiles and annotated interpretations of radial Lines 7 and 9. Solid lines: Strong reflectors and sediment packages. Short dashed lines: Faults. Thin dashed line: Bottom multiple. Intersection with Lines 2 and 23 indicated at top.**

From Centre Hills the debris lenses have accumulated in stacks, the largest being ~10 km long (Fig. 2). The lenses are onlapped by and alternate with sub-horizontal strata. We interpret the lenses as submarine fans from emplacements of volcanoclastic flows, caused largely by lava dome collapses and deposited over several hundred ka. Coarse submarine fans have formed in this way during the current volcanism, producing tapering units extending as much as 8 km offshore (Le Friant et al., 2010; Le Friant et al., 2009).

Where fans are overlain by flat-lying sediment, sedimentation rates can be estimated. We recognize that these rates could be influenced by multiple factors, including minor flows, remobilized deposits, and tephra fallout but assume that fundamentally flat sediment accumulation marks the cessation of the main volcanic source. Off Silver Hills a large fan is covered by ~80 m of flat sediments. Silver Hills became extinct at ~1 Ma (Harford et al., 2002), yielding a sedimentation rate of ~8 cm/ka. Off Centre Hills the sediments are ~44 m thick. The Centre Hills became extinct at ~500 ka suggesting a rate of ~9 cm/ka. Le Friant et al. (2008) report hemipelagic sedimentation rates at a site 60 km offshore as 1-3 cm/ka. At a site ~16 km offshore Trofimovs et al. (2009) report a rate of 4–7 cm/ka. Our higher rates are consistent with a persistent, near-shore sediment source.

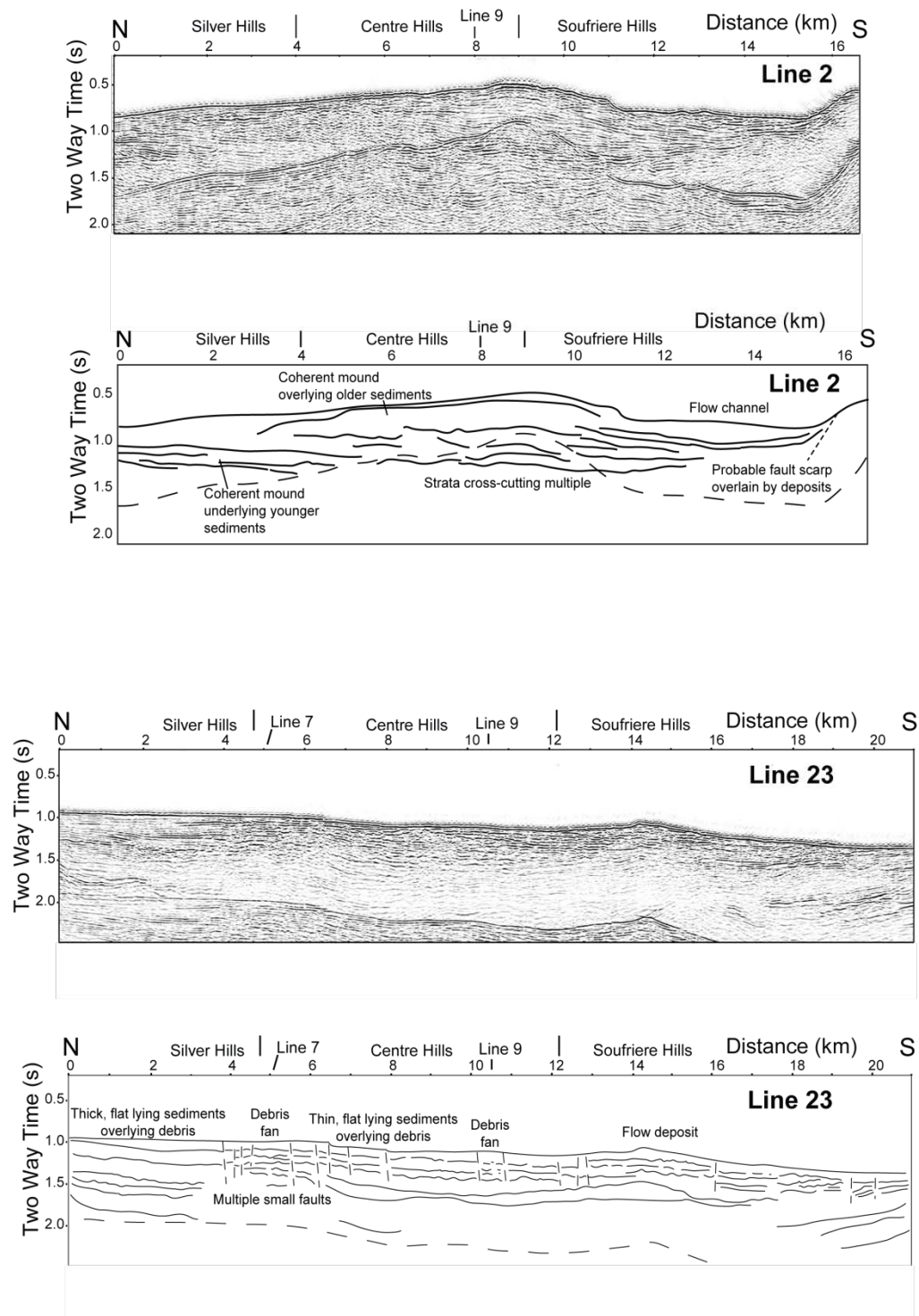


Figure 3.

Figure 3 (continued): Seismic reflection profiles and annotated interpretations of Lines 2 and 23, parallel to the east coast. Description as in Fig. 2. Intersection with Lines 7 and 9 indicated at top. Vertical lines at the top: Boundaries between the major volcanic centers.

The N-S reflection profiles off the eastern shelf cut across the debris fans. Approximately 1-2 km offshore (Line 2, Fig. 3) a mounded feature is visible just below the sea floor between km 6 and km 11. SHV flow deposits 4-5 km off the shelf are indicated by the mound on Line 23 between ~kms 10 and 20. A 6 km-wide channel is visible in Line 2 at km 11 to 15, which we identify as an embayment associated with a previously described gravity flow (Le Friant et al., 2004) (Fig. 1B). The southern slope of the embayment is consistent with the fault scarp north of Roche's Bluff (Fig. 1B and Feuillet et al. (2010)) which subsequently has been modified by landsliding.

#### ***1.4 Exposed and buried faults off the western shelf***

North-dipping fault scarps offset the ocean floor on profiles approximately 6 and 14 km off the west coast (Lines 21 and 15, Figs. 1B and 4). The western scarp offset at km 10 of Line 15 is at least 40 m. The MHFS fault scarp and S-tilted footwall block are clear features as well on nearby profile gwa058 of Feuillet et al. (2010). To the north several faults break the ocean floor, indicating recent activity. A normal fault-bounded step in the morphology near km 16 on Line 15 is associated with the Redonda fault system (RFS) (Fig. 1B). Further north, buried scarps have created basins of folded, syn-rift sediments. Beyond km 23, faulting is buried by ~100 m of flat, basin-filling sediments.

In the south, both profiles reveal complex footwall deformation. At km 4-10 of Line 15 a series of piggy-back basins have formed on the tilted footwall, which is an ascending slope over ~1300 m of elevation. On the elevated footwall of Line 21 (~km 1), a small graben is infilled by subhorizontal sediments (Fig. 4).



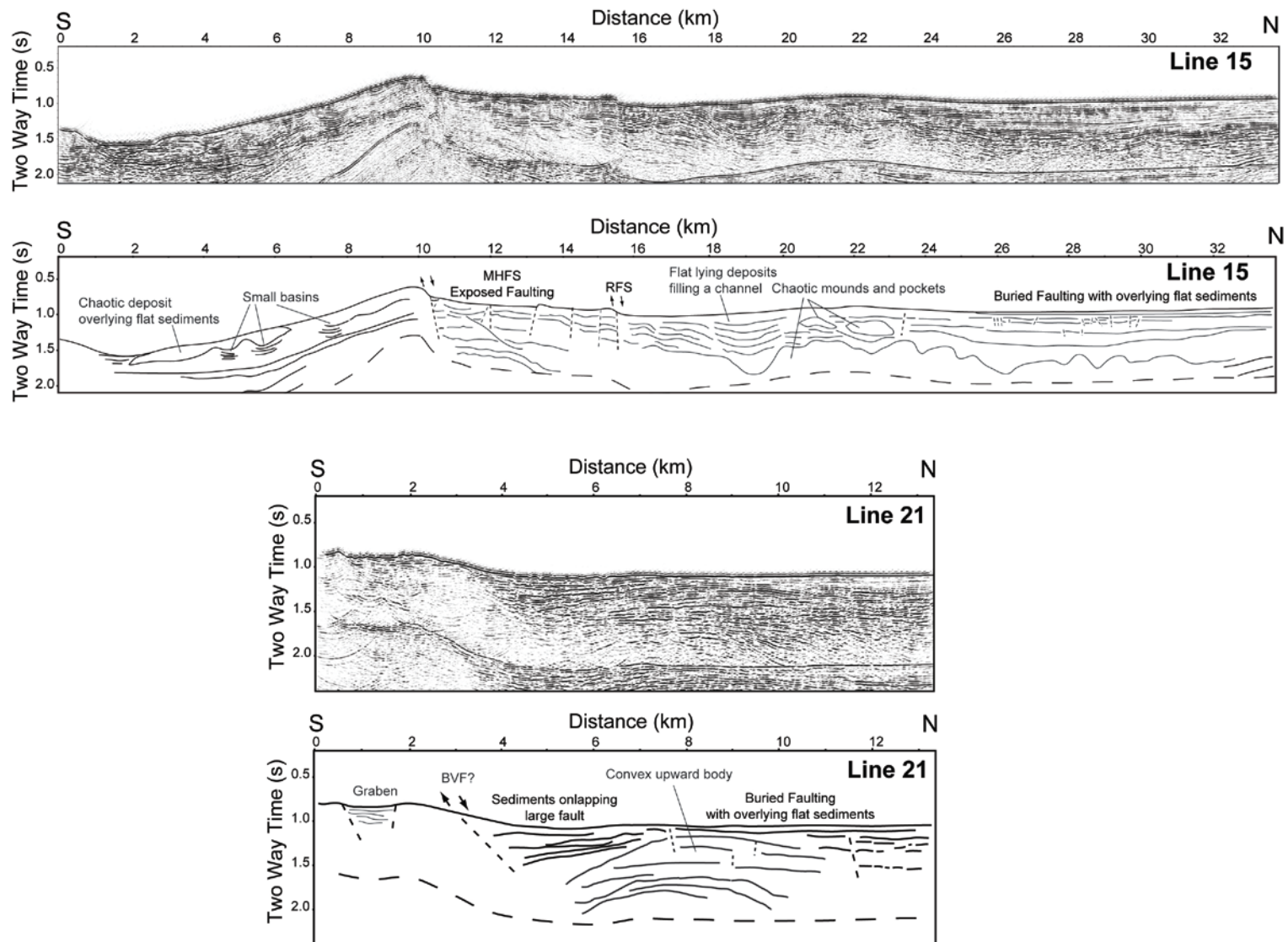


Figure 4.



Figure 4 (continued): Seismic reflection profiles and annotated interpretations of Lines 15 and 21, off the west coast. Description as in Fig. 2.

At km 3 on Line 21, sediments appear to dip to the south and onlap onto a major N-dipping normal fault (Fig. 4). This fault is not the same as the principal scarp fault of Line 15, but is *en-echelon* and south of it by ~2 km (Fig. 1B and Feuillet et al. (2010), Fig. 2). The fault may coincide with an along-strike projection of the Belham Valley fault (BVF, Fig. 1).

### ***1.5 Tectonic synthesis and relation to onshore deformation and volcanism***

A new tectonic interpretation of southern Montserrat can be proposed by integrating our data with older studies and the work of Feuillet et al. (2010). We agree with the regional model of Feuillet et al. (2010) that the major fault systems (RFS, MHFS and BMF) are mainly normal and arranged in a right-stepping *en echelon* structure, and also that on the large scale, this section of the arc accommodates regional left lateral shear. We disagree with the interpretations of the onshore features discussed in Feuillet et al. (2010) and add a discussion of the SHV feeder dike in relation to the complexity of local tectonic and magmatic stresses.

Feuillet et al. (2010) re-introduce the old idea, e.g. Rea (1974), that Garibaldi and St. Georges Hills are volcanic cones and suggest they were fed by vents in a fissure parallel to the BVF. However the field evidence does not support this hypothesis. St. Georges, Garibaldi, and Richmond Hills are composed mainly of block-and-ash-flow and pumice-and-ash flow deposits, and epiclastic beds (Harford et al., 2002). The deposit lithofacies are not compatible with vent or near-vent andesite eruption products but most likely have been sourced from SHV. However, while the lithofacies are similar to those of modern lava-dome flank environments where original bedding dips <8°,

exposed beds on Garibaldi Hill have dips up to 50° (Harford et al., 2002). In addition, 3-D tomography (Shalev et al., 2010) indicates low *P*-wave velocity material under St. Georges and Garibaldi Hills, quite unlike the high velocity cores under SHV and Centre Hills. Thus we conclude that the morphology of these hills is not primary; they are fault-bounded tectonic uplifts that have been deformed by (mostly) normal faults, and deposits have been tilted beyond the sedimentary slope limits.

A closely related issue is the BVF, which, in contrast to Feuillet et al. (2010) but following Harford et al. (2002), we interpret as a N-dipping normal fault. This is consistent with our interpretation of Garibaldi and St. Georges Hills as tectonic uplifts; in addition, these onshore blocks seem analogous to the prominent elevated footwalls seen offshore on Lines 15 and 21 (Fig. 4; cf. Feuillet et al. (2010), Fig. 3, profiles gwa 055 and 058). The N-dipping fault in our marine profile Line 21 (Fig. 4, ~km 3), is aligned with the BVF as an along-strike projection, and the north-dip on the offshore profile supports a similar interpretation for the BVF. Finally, 3-D tomography (Shalev et al., 2010) indicates that the contact of the *P*-wave velocity anomaly boundary under St. Georges Hill dips (very roughly) 50° N.

Regionally, southern Montserrat is part of a transtensional regime with extensional overprinting. Transtensional deformation zones involve rotation, local compression, and uplift (Dewey et al., 1998), which is consistent with the uplifted blocks and also westward-dipping sediments off the east coast. Locally, southern Montserrat includes a right-step between the MHFS and the BMF, *en echelon* normal fault systems in sinistral slip; thus uplift may have been encouraged by a minor contractional component (Cunningham and Mann, 2007; Deng et al., 1986).

The interplay of the transtention, contraction, and magmatism has resulted in evolving stress regimes around SHV and the BVF and related faults, as demonstrated by (Miller et al., 2010). Estimates of the orientation of the SHV feeder dike include a NNE trend based on 1995 seismic data (Miller et al., 2010), and a NNW trend based on 1997 ground tilt data (Hautmann et al., 2009). A way of reconciling these data is to have a dike oriented ~N, which is compatible with a northerly trend of magma-transport-related hybrid earthquakes under SHV (Miller et al., 2010, Fig. 2). A northerly dike trend implies a local E-W axis of minimum compression, which is approximately orthogonal to the MHFS-BMF regional trend of N-S extension (Feuillet et al., 2010; Feuillet et al., 2001). Stresses appear to have been subjected to strong local reorientation. This could be due to some combination of varying pressures caused by the propagation of dikes and evolution of the magma storage system (Gudmundsson, 2006) and to being within a complex fault step (Oglesby, 2005).

Based on marine reflection profiles and related onshore data, we conclude that on Montserrat the interplay among local faulting, volcanism, and stresses is very complex. The regional transtensional system of *en echelon* faults (Feuillet et al., 2010) has influenced volcanism, while the local fault step suggests both a component of compression and complicated, evolving stress regimes and fault movements.

## **2. Microseismicity and 3-D Mapping of an Active Geothermal Field, Kilauea Lower East Rift Zone, Puna, Hawaii**

The local fault and dike structures in Puna, southeastern Hawaii, are of interest both in terms of electricity production and volcanic hazard monitoring. The geothermal power plant at Puna has a 30MW capacity and is built on a section of the Kilauea Lower East Rift Zone that was resurfaced by lava flows as recently as 1955 and 1960.

The Puna Borehole Network was established in 2006 in order to provide detailed seismic data about the Puna geothermal field. The array consists of eight 3-component borehole seismometers. The instrument depths range from 24 to 210 m (80 to 690 ft); five stations with 2 Hz geophones and three with 4.5 Hz geophones.

The large majority of events were  $< M_{0.5}$  and occurred at depths between 2 and 3 km. The size, location, and depth of the microearthquakes suggest that power plant activity affects local seismicity. Earthquake depths increase from NE to SW, trending up the rift zone towards the Kilauea summit. Depths also increase from the study area to the SE, consistent with active normal faulting along Kilauea's south flank. Shear wave polarization indicates that the active, fluid-filled fracture system trends SW-NE, consistent with the orientation of the LERZ. Double difference relocation suggests an intersecting network of fractures with both NE and approximately NW trends.

3-D tomographic analyses of P-wave velocity, S-wave velocity, and the  $V_p/V_s$  ratio are also presented. An area of anomalously fast P-wave velocity at the relatively shallow depth of 2.5 km may be evidence for a dense, gabbroic intrusion. This intrusion may underlie and be the parent of a body of dacitic melt that was discovered under the geothermal field during drilling.

## ***2.1 Introduction***

The Puna geothermal system is located along the volcanically active Lower East Rift Zone (LERZ) of Kilauea Volcano, on the island of Hawaii, USA. Exploration for geothermal resources on the LERZ started in the 1960's; the geothermal power plant, Puna Geothermal Ventures (PGV), has been operating since 1993. The 30MW field supplies approximately 30% of the electricity needs of the Big Island of Hawaii. By working with PGV, we gained access to this active resource.

The seismicity of the Puna geothermal system has not been well described until now, when a borehole seismic network has allowed us to record small local microearthquakes. At geothermal systems around the world, both natural and induced seismicity have been documented extensively, and the majority of these earthquakes are small. Because the PGV geothermal plant is in a populated and seismically noisy area, borehole instruments reduce the surface noise and are more effective at recording geothermal seismicity. Having recorded and located >4000 microearthquakes, we applied the data to three analytical components: Shear wave splitting, double difference earthquake location, and 3-D tomography.

Shear wave splitting analysis is a widely used means of determining fracture orientation. The method is based on the principal that shear waves polarize into a faster and a slower wave when they encounter aligned fractures (Crampin, 1981). The particle motion of the faster wave generally aligns in the direction of fracture orientation. Fluid saturated fractures in geothermal areas include both micro- and macro-faults, from which strong shear wave polarization can occur (Crampin and Peacock, 2005). In the Puna geothermal area, the major fluid conduits appear to be large fractures, making it of great interest to understand their orientation and location. Shear wave splitting has been

used successfully in geothermal areas to identify the direction of primary and secondary stress-aligned fractures (Lou et al., 1997; Tang et al., 2008).

The double difference algorithm of earthquake relocation (Waldhauser, 2001; Waldhauser and Ellsworth, 2000) resolves earthquake locations from a cloud or cluster to a plane or linear feature as would be expected for a fault. The method correlates hypocenters based on P- and S-wave arrival times and/or waveforms correlation and relocates them with respect to other “related” earthquakes. This eliminates the uncertainties associated with the velocity model and picking errors. The method has been used to identify seismogenic structure in both magmatic systems (e.g. Prejean et al., 2002; Prejean et al., 2003) and geothermal systems in trying to resolve “clouds” of earthquakes associated with fluid flow and injection (e.g. Clarke et al., 2009; Lippitsch et al., 2005).

A third method for visualizing the structure of geothermal systems is 3-D seismic tomography. In geothermal areas, methods of tomographic inversion have been used to improve knowledge of local velocity structure (De Matteis et al., 2008) and have a proposed use to monitor changes in geothermal and magmatic reservoirs (Chiarabba and Moretti, 2006; Gunasekera et al., 2003). The method has been documented extensively with respect to magmatic systems (see the review by Lees (2007) and references therein), including Kilauea, but has not been applied along the Lower East Rift Zone, nor with the localized focus of our seismic network.

In 3-D tomography, the resolution of the inversion increases with the number of seismic stations; the resolution is determined by the number of raypaths between the hypocenter and the seismic receiver that cross through each volume of a designated 3-D grid. As the number of receivers increases, so does the number of raypaths from the

earthquake; with increasing raypaths, the volumes within the 3-D grid can be decreased and the resolution increases.

In this study we use microseismicity to investigate the fault and fracture system in the Puna geothermal field. We use the locations of >4000 microearthquakes to improve the local velocity model, identify fault and fracture orientations, and use 3-D tomography to locate zones of high and low seismic velocities. Along this segment of the LERZ, water, magmatism, and fractures have coincided to create a permeable, steam-rich, high-temperature environment. The goal of our work is resolving the inner structure of this system.

## ***2.2 Geologic context***

Kilauea Volcano is a long, narrow structure built on the shoulder of the neighboring volcano Mauna Loa; Kilauea has a summit crater, the site of both effusive and explosive volcanism, from which two major rift systems extend. The Puna geothermal field is located on the Lower East Rift Zone (LERZ), approximately 40 km east of the summit. The local geology consists of basalt flows underlain by hyaloclastites and injected by basaltic dikes (Trusdell et al., 1993). Volcanic activity has included fissure eruptions with fountaining and lava flows; the LERZ has been resurfaced by lava flows over the last 300 years (Moore and Trusdell, 1991). The lava flows in the area of the geothermal system are from 1955 (Moore and Trusdell, 1991). This section of the LERZ contains an apparent “jog” in the rift (Figure 5). Two lines of cones and craters extend from this “jog,” both oriented SW-NE, but offset by approximately 1.5 km. The geothermal system is within the offset, which is encompassed in the borehole network among stations P02, P01, P03, and P05 (Figure 5).

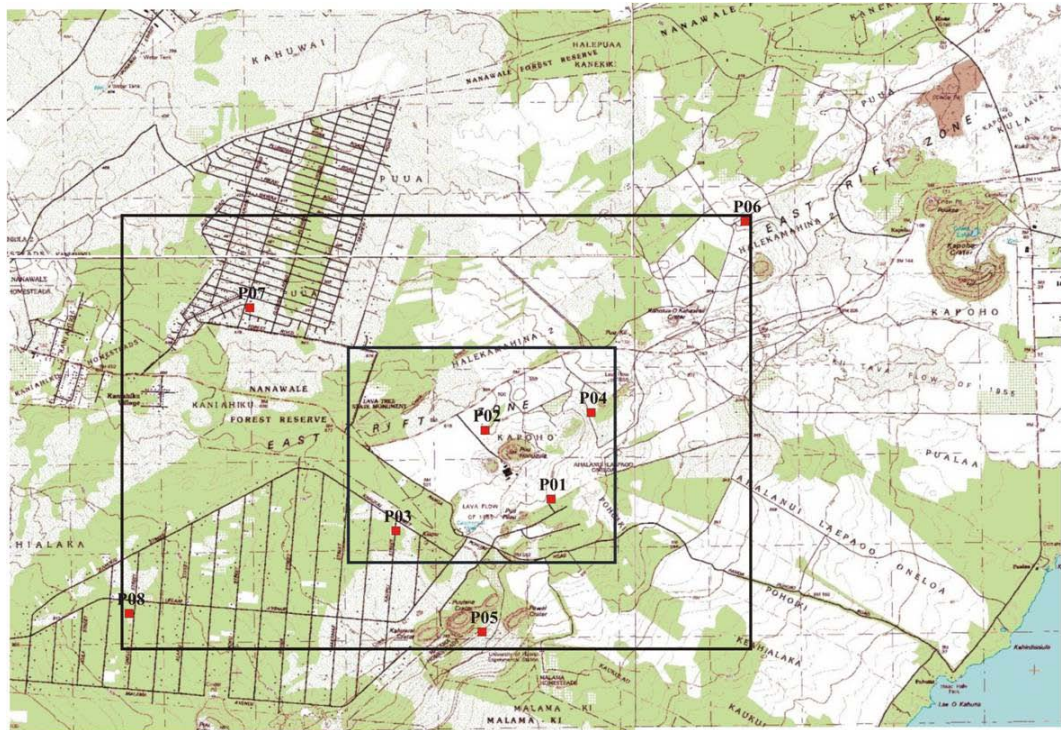


**Figure 5: Topographic map of the Puna Borehole network area. Red squares mark station locations. The black dot is Puna Geothermal Venture. The large black rectangle is the target zone for the 3-D inversion. The small black rectangle is the area of good ray coverage shown in detail in the 3-D plots.**

The most extraordinary geologic aspect of the Puna geothermal field is the confirmed presence of dacitic magma at approximately 2.5 km depth (Marsh et al., 2008; Teplow et al., 2008). The magma was discovered during routine drilling at PGV. The drill team inadvertently drilled into active magma, which repeatedly oozed up the well bore while the drill bit was withdrawn and relowered; drilling was stopped when clear glass chips came out as cuttings. The magma demonstrates both the unpredictable nature of this system and, perhaps, an explanation for the local high heat levels. Much work remains in terms of discovering the source of the magma, and we intend our contribution to be towards understanding the structure that encouraged the magma to accumulate and differentiate under the Puna geothermal field.



### ***2.3 Network setup***

The Puna Borehole Network consists of eight 3-component seismographs centered on the geothermal field in two concentric rhombs (Figure 5); the design maximizes both coverage for locating earthquakes and angles to calculate shear wave splitting data. Two stations are located at PGV; others are on private property where owners were approached by PGV personnel and kindly agreed to allow us to set up a permanent station. The station depths range from 30 – 210 meters. The instruments have been designed to work in HQ-type boreholes, diameter ~100mm; seven of the boreholes were drilled for the array, and the eighth hole was an existing water well. The latter (P04) is the deepest and hottest borehole, with a temperature of 90°C.



**Figure 6: A. Inside of the 3-component borehole seismometer. Top geophone is vertical; middle and bottom geophones are horizontal and orthogonal. Geophones are**

Figure 6 (continued) the small cylinders; the large conical shapes are gimbaled counterweights to control for borehole tilt and contribute to damping. 6B. Installation of a seismometer into a standard diameter HQ borehole. Top half of the instrument is a tiltmeter.

Five instruments consist of gimbaled 2 Hz geophones (Figure 6A), whereas the other three instruments (P01,P02 and P04) consist of gimbaled 4.5 Hz geophones. Two of the stations (P01 and P02) also include a tiltmeter and an accelerometer. Acquisition units are Reftek 130 recorders from which data cards are collected and uploaded. Data is continuously recorded at a sampling rate of 200 samples/sec; data cards are collected every 10 days. Following upload, the events are identified by a triggering program and are located using HYPOINVERSE-2000 (Klein, 2002) after P and S arrivals are picked manually.

## ***2.4 Local seismology***

The array has recorded about 6000 earthquakes since June, 2006 (Figure 7). First arrivals were picked by hand then earthquakes were located using HYPOINVERSE-2000 (Klein, 2002). Seismicity occurs in a northeast-trending linear swath consistent with the orientation of the Kilauea Lower East Rift Zone. The majority occurs under the geothermal plant, at depths from 1.5 to 3.5 km; this is consistent with geothermal production and injection at these depths. Earthquakes at depths of 3.5 – 5.5 km occur throughout the system but are most visible up-rift towards Kilauea summit. Earthquakes of increasing depth occur to the southeast of the rift; this is consistent with the presence of a large normal fault of northeasterly strike and southeasterly dip. Such a fault has been suggested in field mapping but not described in detail; the presence of the fault would be consistent with the southerly movement of the south flank of Kilauea along the dominant plane underlying the Hilina Fault System (Parfitt and Peacock, 2001).

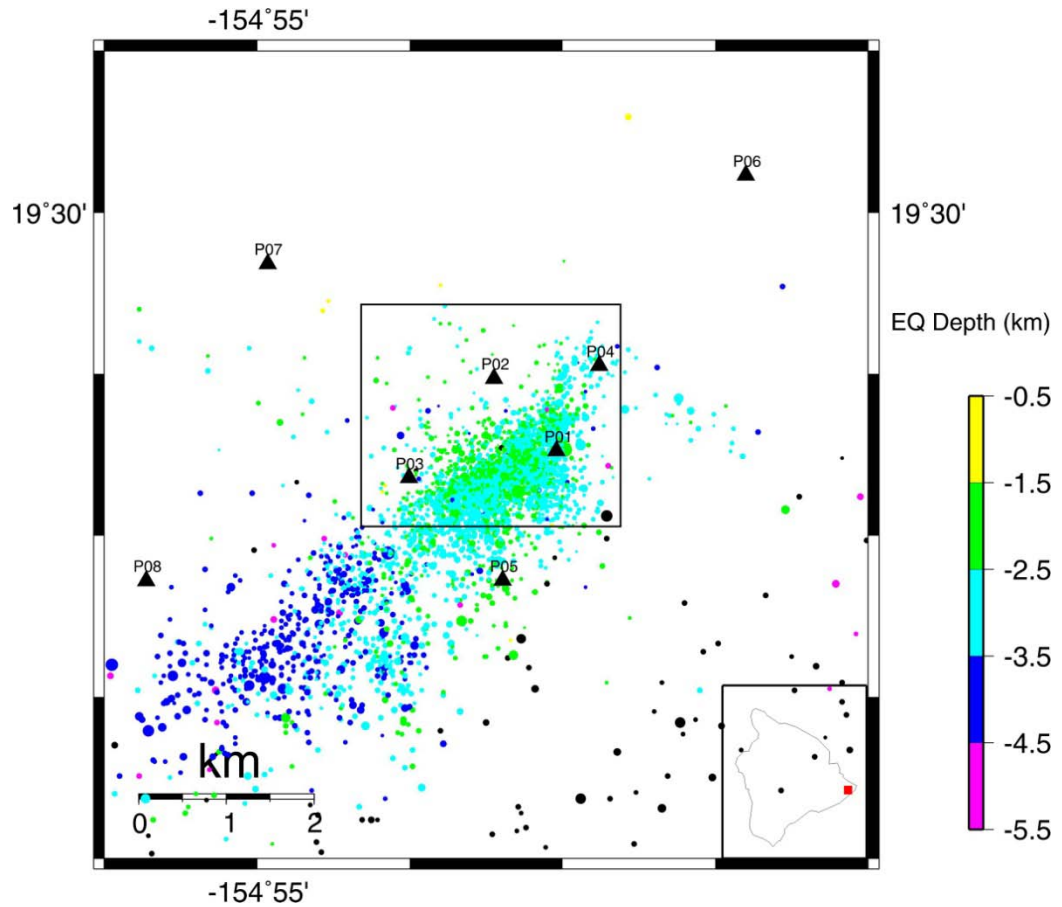


Figure 7: Map view of Puna seismic array stations and earthquakes. Black triangles are seismic stations. Earthquake locations are marked by dots colored according to depth. The size of the dots indicates the magnitude, ranging from M-0.2 to M2.0.

The Magnitude frequency distribution is usually described by the “B-value” based on the Gutenberg-Richter relationship:

$$\text{Log}_{10}(N) = A - B \cdot M$$

Where N = number of events with Magnitude  $\leq M$  and B= slope of the distribution

Figure 8 shows the B-value plot for all events  $-0.2 < \text{Mag} < 2.0$  located within 5 km from the center of the detailed target zone with B-value = 1.48. The increase in slope

at magnitude below 0.5 indicates that there is an increase in the number of events smaller than  $M_{0.5}$ ; 95% are of magnitude  $<0.5$ . This may be attributed to reinjection of geothermal fluid. Without this jump in the number of smaller events, the B-value is 1.3.

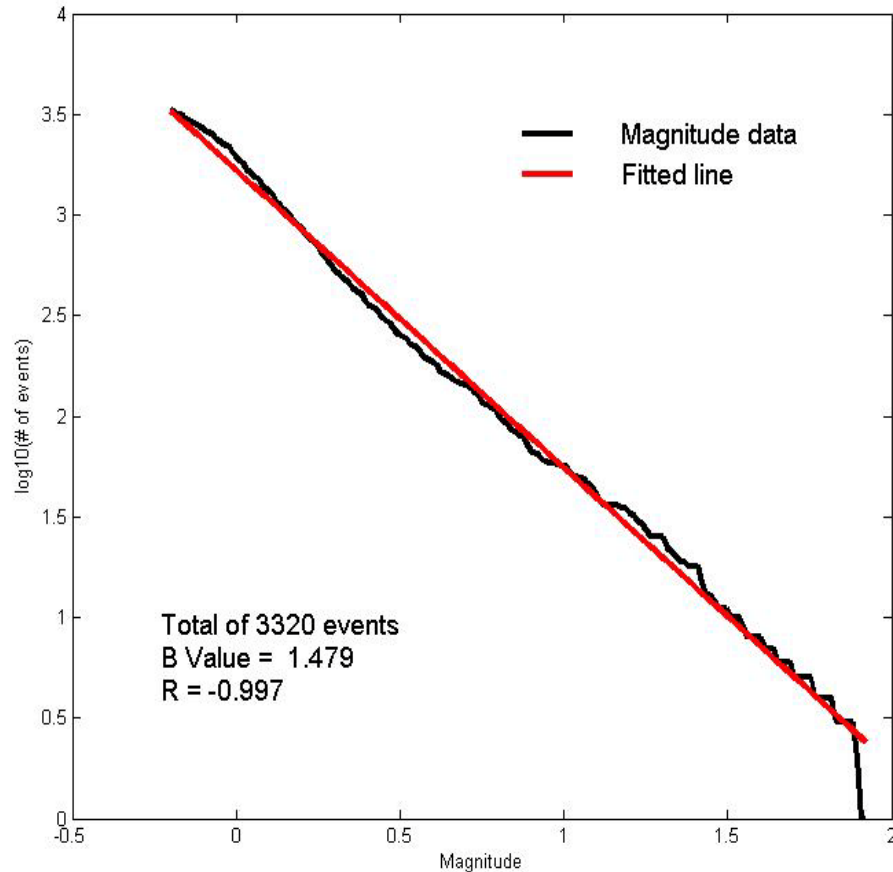


**Figure 8: Plot of the number of earthquakes of a given magnitude according to the Gutenberg-Richter relationship. The slope of the plot represents the B-value, 1.48. The value of  $R = -0.997$ .**

Seismic moments for the events were computed using the spectral method of Andrews (1986). Magnitudes were calibrated with events also detected by the Hawaiian

Volcano Observatory (HVO). The lowest useable detection threshold for the PGV network is M-0.2.

## ***2.5 Shear wave splitting***

Shear wave splits were picked automatically after the S-waves had been identified by hand. Figure 9 shows an example of a shear wave split before and following rotation.

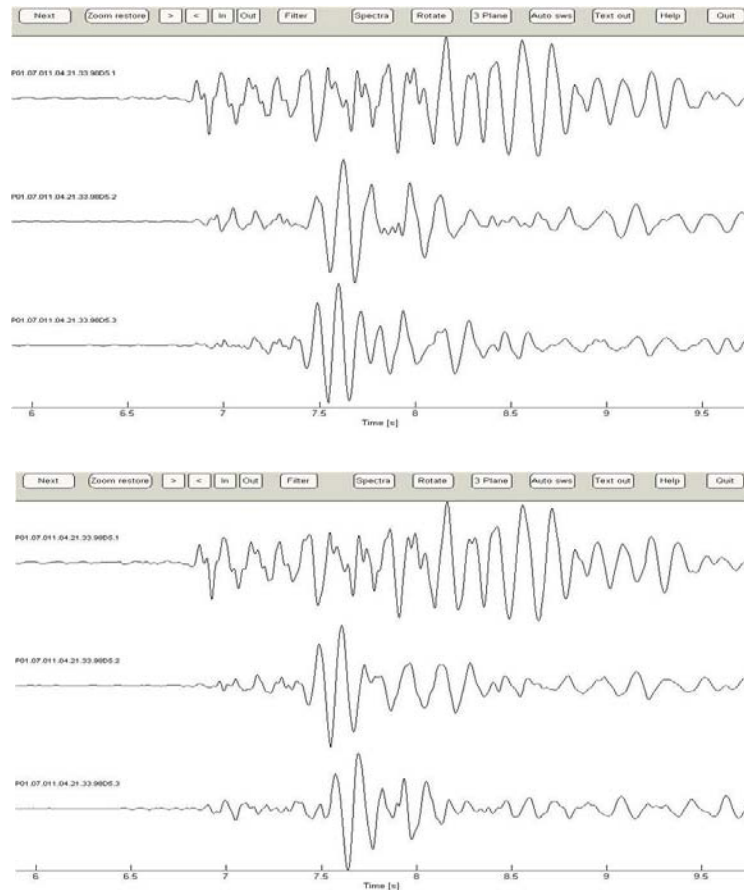


**Figure 9: The upper diagram shows the original seismogram, with no shear wave splitting identifiable. The lower diagram shows the seismogram after 56° rotation. Shear wave splitting is visible.**

The dominant fracture orientation is consistent with the Kilauea East Rift Zone, i.e. trending NE (Figure 10). Rose diagrams indicate the dominant direction of fast shear-wave motion, which is generally SW-NE at the geothermal field. The slight

variation of stations P4 and P5 from the general trend can be attributed to errors in station orientations derived from local seismicity. A lack of earthquakes to the northeast of the field prevented processing of shear wave splits at station P06, so it is not clear whether the northward fracture orientation continues. At P01, immediately above the largest concentration of earthquakes, there was a secondary orientation of fast shear-waves, trending W-E. This indication of a secondary fracture system is consistent with results we got from double difference relocations.

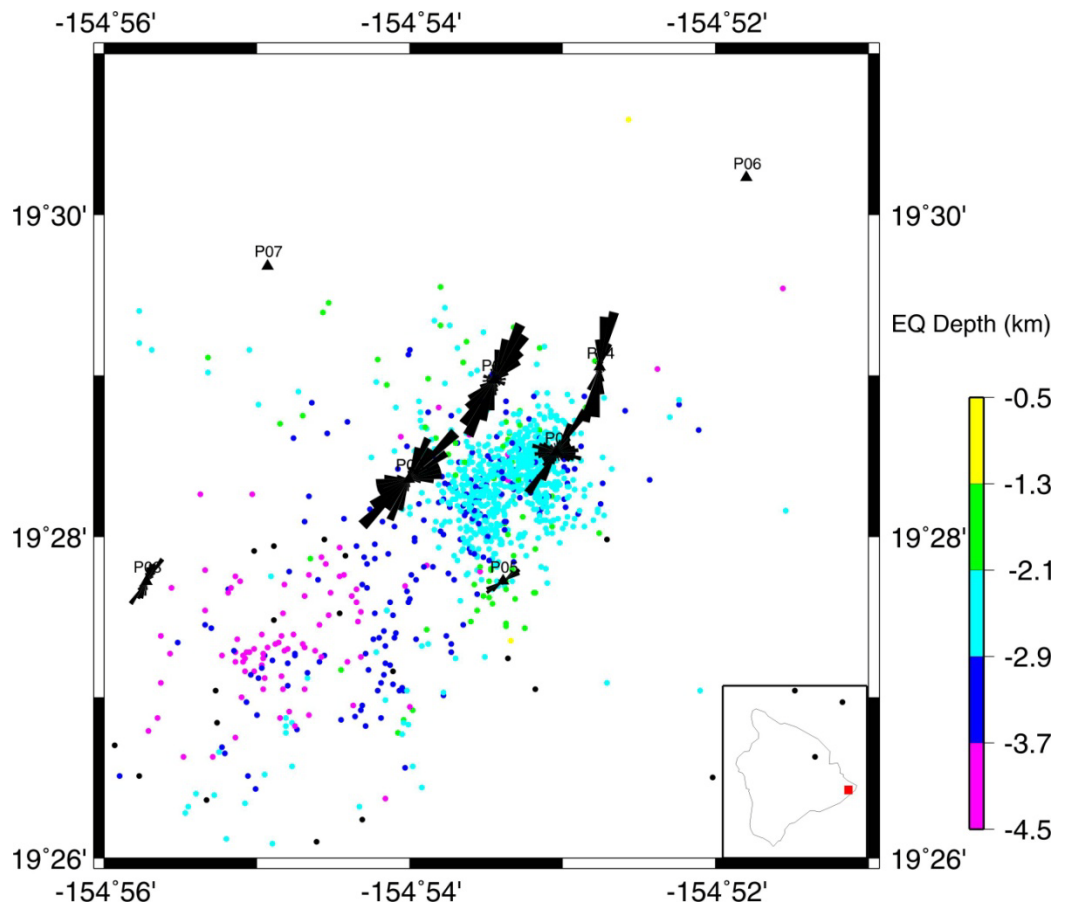


**Figure 10: Rose diagrams indicating the fast shear wave polarization directions. Each bin is 5 degrees wide. The length of the bin reflects the number of shear wave splits in the bin. A total of 1500 shear wave splitting observations were made, most of them by stations close to the center of the earthquake cluster. Black triangles are seismic stations. Earthquake locations are marked by dots colored**

Figure 10 (continued). according to depth. The size of the dots indicates the magnitude, ranging from M-0.2 to M2.0.

The individual fast shear wave orientations at five stations are portrayed in Figure 11, a polar coordinate projection. Each line is one observation, showing the azimuth and incident angle of the hypocenter to the projected half space. This figure shows the level of complexity of the fracture system, where within a limited area fractures may be oriented in several different directions. The trend of the rift zone is clear, as are orientations in an E-W direction.

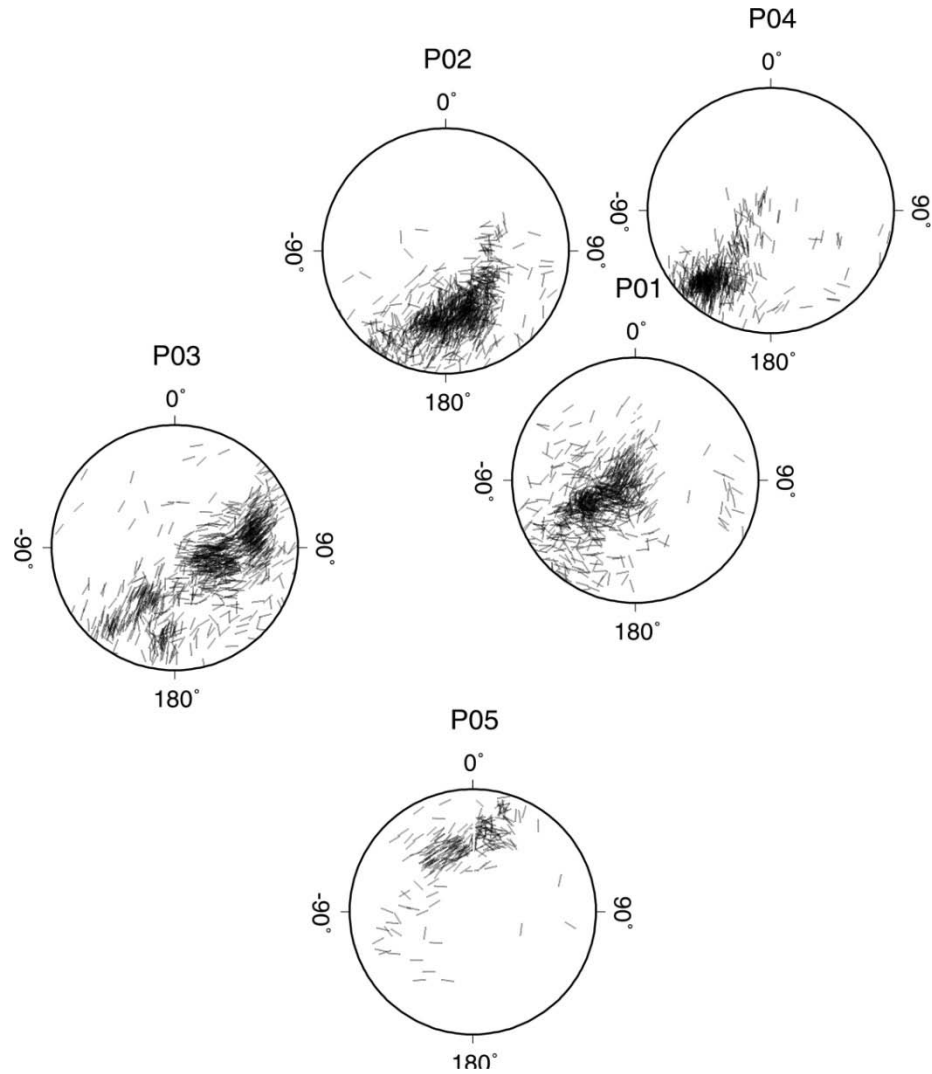


**Figure 11: Polar coordinate projection (azimuth and angle) of shear wave splitting polarization. Each circle represents all shear wave splitting observations for one station. The circumference of each circle represents a 45° incident angle from the vertical. Azimuth marks the direction toward the hypocenter. The location of each line represents the azimuth and the incident angle of one shear wave splitting observation. The orientation of each line is the direction of the fast shear wave polarization for that observation. Stations P01, P02, P03, P04, and P05 are plotted in the correct geographical location.**



## 2.6 Double difference relocation

All of the earthquakes detected over the recording period were relocated using the double difference algorithm of Waldhauser (2001). Currently catalog-type data is used; it is on-going work to develop the correlation data and thus improve the current result. The absolute location of the earthquake cluster has not been adjusted, so this data set can be considered an indication of structural features rather than exact fracture locations. A comparison between the HYPOINVERSE-2000 and the double difference locations (Figure 12) shows improvement in resolution.

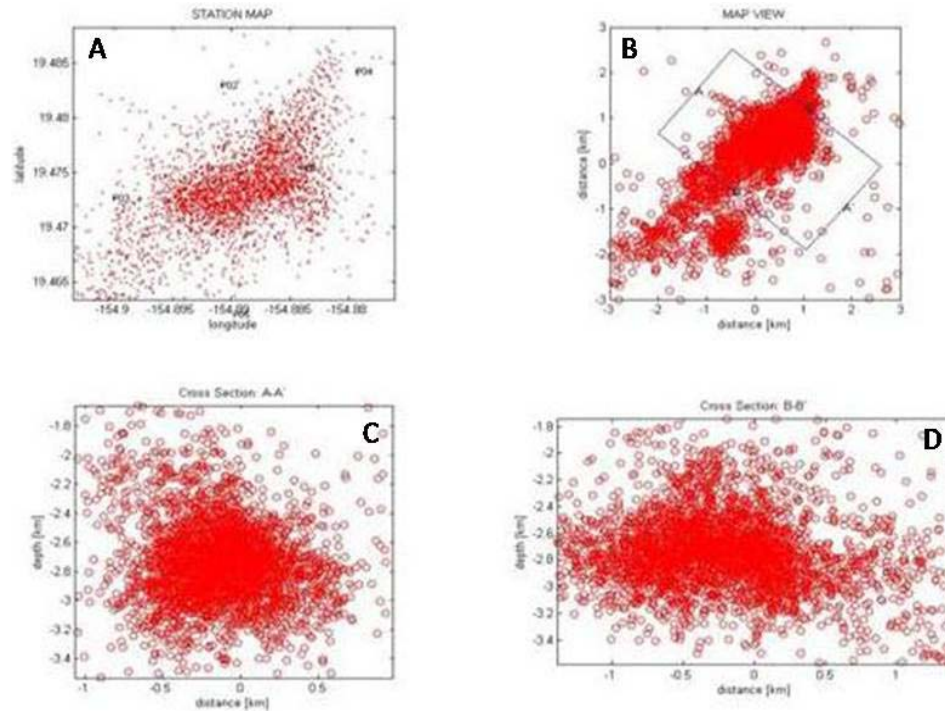


Figure 12: Map and Cross section views of events that have been double difference relocated. Figures (12A) and (12B) are both map views with 12B showing a detailed view of the area. Figure (12B) shows the area used to generate the projected cross sections in figures (12C) and (12D).

Two broad types of patterns can be identified in the earthquake locations: Rift parallel and rift perpendicular. The dominant rift parallel structures trend in the same

NE direction as those of the Kilauea rift zone (Figure 12). The secondary rift perpendicular structures are observed throughout the study area but are most strongly observable in the main body of the cluster and in the projected cross section figure (12D).

## ***2.7 Seismic tomography***

Tomographic inversion followed the method described in Shalev and Lees (2004) and Lees and Shalev (1992). The preliminary velocity model was based on earthquake locations from the Hawaiian Volcano Observatory. This model was iteratively revised using the earthquakes from the current data set. Earthquakes were located and iteratively relocated in conjunction with the velocity model.

For the 3D inversion, events were used that were recorded at all eight network stations. The volume used was 2 km x 2 km x 4 km, centered at 19° 28' 42.3N, 154° 53' 17.6W. The volume extended from 200m above sea level to a depth of 4 km. The volume was parameterized with a grid of constant-slowness cubic cells with sides of 100m.

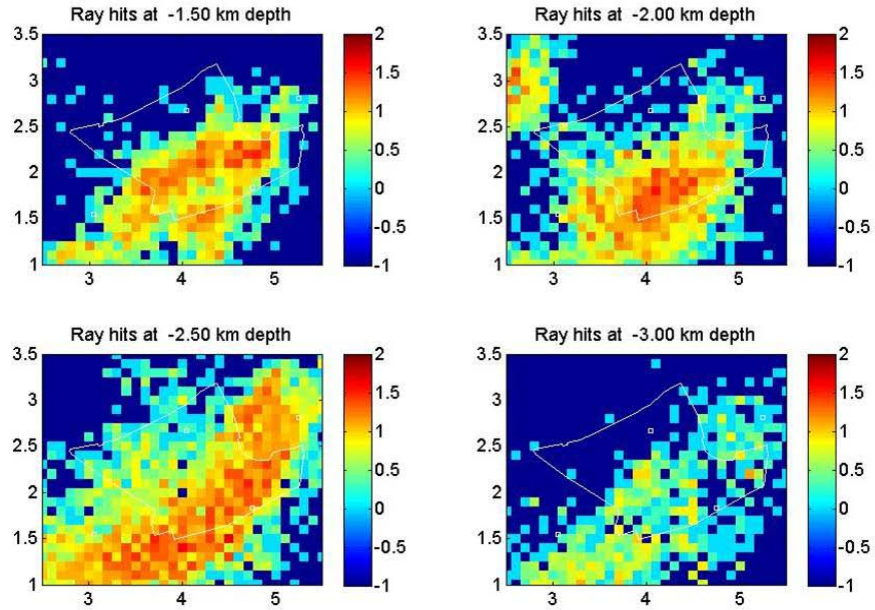


**Figure 13: Hit-count map of the target zone. Images are horizontal slices at depths of 1.5, 2.0, 2.5, and 3.0 km. Colors indicate log10 number of rays that pass through each 100m x 100m x 100m volume. The thin line within each map marks the PGV lease.**

Figure 13 shows the number of rays that passed through cubic volumes within the target area. The ray coverage was consistently best in the central to southern areas of the target, with the most hits at 2.5 km depth.

Vp is slower than average under the central geothermal field at 1.5 and 2 km depth; at 2.5 km and 3 km depth Vp is exceptionally fast (Figure 14).

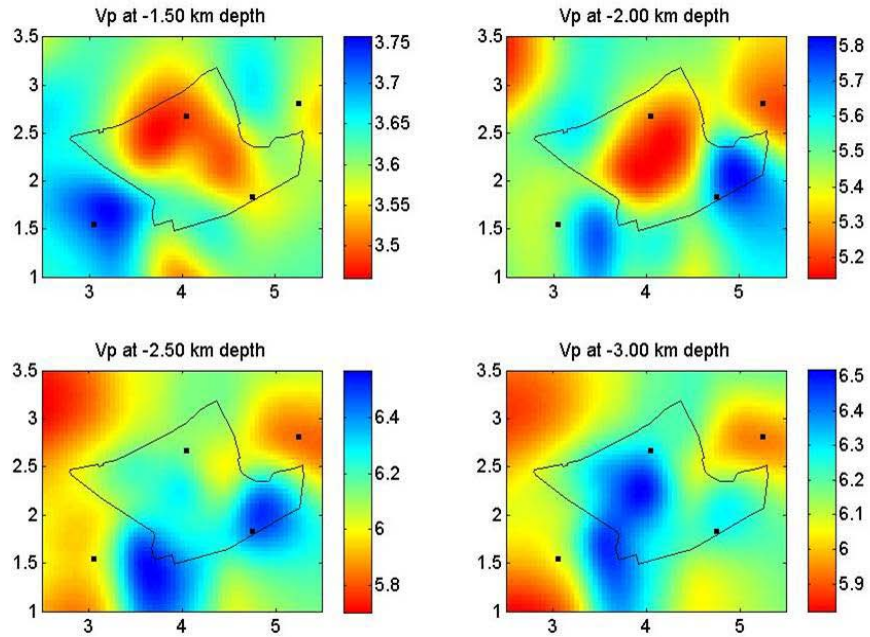


**Figure 14:** The 3-D tomographic inversion for P-wave velocity presents data in horizontal slices at 1.5, 2, 2.5, and 3 km depth. The figures show Vp perturbation, the change from the average velocity at each depth. Reds represent slower velocities and blues represent faster velocities. X and Y axes are km from a chosen origin.

Figure 15 shows the Vp/Vs inversion. At 1.5 and 2km depth, Vp/Vs is slower than the average for the depth to the east and faster to the west. At 2.5 and 3km depth, Vp/Vs is faster to the south. Because of the fast P-wave velocities at 2.5-3 km depth, it is likely that the high Vp/Vs values are more strongly affected by P-wave than S-wave velocity.

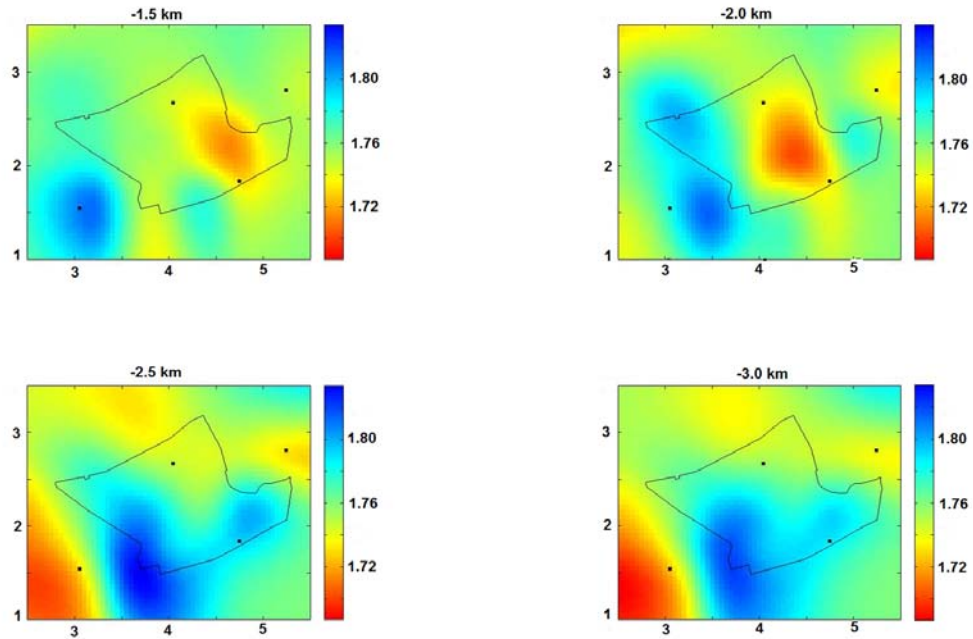


Figure 15: The 3-D tomographic inversion for  $V_p/V_s$ . Horizontal slices are at 1.5, 2, 2.5, and 3 km depth. Red represents slower ratios and blues represent higher ratios. X and Y axes are km from a chosen origin.

## 2.8 Discussion

Hydrothermal areas commonly occur in zones of fault propagation and interaction (e.g. Curewitz and Karson, (1997) and references therein). The Puna geothermal area is located in a “jog” between the ends of two rift segments separated by approximately 1.5 km; this area may be a transfer zone, where the interaction between fault tips has caused increased fracturing and permeability. The dominant structure underlying the system consists of normal faulting, with northeasterly strike, parallel to the Kilauea East Rift Zone and dipping to the south. By contrast, our double difference results are consistent with the shear wave splitting results and indicate cross-cutting fractures approximately orthogonal to the NE trend. At Krafla, Iceland, a magnetotelluric

survey (Onacha, 2006) and shear wave splitting (Tang et al., 2008) also have observed fractures orthogonal to the dominant rift/normal faulting direction.

Secondary fractures approximately orthogonal to the dominant normal fault strike have been addressed in two similar models, Hill (1977) and Rowland and Sibson (2004). Hill (1977) describes the formation of dikes and conjugate faults as related to earthquake swarms from dike intrusions. Rock permeability increases as dikes develop and open in the  $\sigma_2$  direction. Rowland and Sibson (2004) describe a similar model to explain permeability in the rift system at Taupo Volcanic Zone, New Zealand. As in any system, normal faulting at the Kilauea LERZ must be accompanied by secondary movement to accommodate stress.

The tomographic results showing high P-wave velocity at ~2km corresponds to a region just below where Puna Geothermal Ventures drilled into a body of active dacitic melt. The melt itself appears to be too small to be seen with the resolution of our array; future work includes analyzing for a melt-related S-wave shadow. Since P-wave velocities increase underneath the melt body, we hypothesize that the high-velocity body is an intruded gabbro, an intrusive rock of basaltic composition but with higher crystallinities and higher seismic velocities ( $V_p = \sim 6.7\text{km/sec}$ ). The presence of the magma body is an astonishing scientific opportunity, and proposals are being submitted to the US National Science Foundation and Department of Energy to try to obtain funding for further drilling and research.

## ***2.9 Conclusions***

1. In the Puna geothermal field, the dominant pattern of seismicity aligns parallel to the Kilauea Lower East Rift Zone. The majority of earthquakes occurs at 2-3 km depth, possibly associated with activity at the geothermal production plant.

2. Secondary fractures approximately orthogonal to the primary faulting are indicated by shear wave splitting analysis and double difference earthquake location. Further work to improve double difference locations includes correlating waveforms and calculating absolute locations of fractures. In addition, we are analyzing many small, linear features chronologically by video. With step by step hypocenter chronology, we can isolate swarms and see the pattern of features along which they occur.

3. 3-D tomography indicates the presence of a high-velocity zone under the central geothermal field. The zone underlies a dacitic melt body at ~2km depth; it is possibly a gabbroic intrusion that was the source of the melt.

### **3. Applications from the fracture dominated, high-temperature hydrothermal system of Puna, Hawaii, for St. George's Hill, Montserrat**

#### ***3.1 Introduction***

The fundamental requirements for a hot, persistent hydrothermal system are heat, fluid, restraining boundaries, and permeability for fluid circulation. In volcanic areas, the heat comes from magmatic intrusions, e.g. dikes or sills, which may or may not result in a surface eruption. Fluids may be meteoric, sea water, or deep crustal/juvenile magmatic waters. Restraining boundaries may be the cap rock, or “clay cap,” consisting of altered rocks above a hydrothermal system that alter to clays and form an impermeable layer (e.g. Jones and Dumas, 1993). Lateral boundaries on a hydrothermal system are commonly faults, in which the core of gouge may form an impermeable layer when perpendicular to fluid flow. Faults and fractures, however, also may be the primary conduits for hydrothermal flow and thus the key to permeability in low-permeability rocks (Rowland and Sibson, 2004; Sibson, 1996).

In contrast to a system in which the permeability is governed by the composition of the rock itself, in a fracture dominated system fluid flow and permeability are governed by a fracture network (Rowland and Sibson, 2004). This paper uses the definition of fractures from the Glossary of Normal Faults (Peacock et al., 2000): Fractures include such approximately planar discontinuities as dykes, faults, joints, and veins. Fractures thus encompass both features in which voids open parallel to  $\sigma_2$ , perpendicular to the primary stress direction ( $\sigma_1$ ), and faults, in which displacement occurs along a fault plane.



The permeability of massive igneous rock is  $<10^{-16} \text{ m}^2$ , too low to support convective fluid circulation, so fractures are required to maintain high-temperature systems that are almost always associated with volcanic regions (Rowland and Sibson, 2004). Fracturing can increase permeability to a range of  $10^{-15} - 10^{-11} \text{ m}^2$ , within the range of convective/advective flow (Rowland and Sibson, 2004). The number of fractures in a system increases the permeability by increasing the number of fracture intersections; for  $n$  fractures in a unit volume of rock, the permeability of the rock with  $n$  fractures is proportional to  $n!$  (Leary et al., 2010). Faulting appears to be critical for maintaining permeability in hydrothermal systems by providing a dynamic element: Fractures in hydrothermal systems are easily filled by mineral precipitation, and active faulting interferes with precipitate accumulation or reopens fractures that have been sealed (Curewitz and Karson, 1997).

A model for permeability associated with faulting has been developed from a model for fracture mesh associated with earthquake swarms (Hill, 1977) (Figure 16). The model explains the occurrence of earthquakes in swarms as due to sequential slip of multiple microfractures in a network (Hill, 1977).

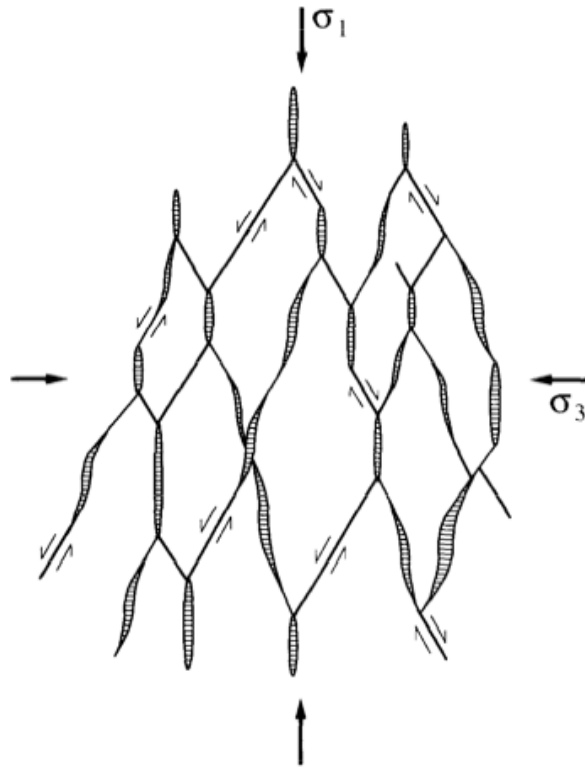


Figure 16. Hill (1977) mesh model for earthquake swarms and Sibson (1996) model for fracture permeability. The model includes interlinked shear, extensional, and extensional-shear fractures. Diagram represents an extensional normal-fault stress regime when upright, a compressional thrust-fault regime when viewed sideways, and a strike-slip regime in plan view.

Subsequently Sibson (1996) applied the model to fracture permeability. In the Sibson model, slip along the microfractures creates openings at the fault intersections that are perpendicular to the dominant faulting direction, i.e. extension fractures (Figure 16) (Sibson, 1996). The extension fractures allow fluid flow throughout the system, thus increasing the local permeability.

For the geothermal industry, the test of the permeability of a hydrothermal system is whether high temperature fluids can be drawn from the system in great enough

volume to generate sufficient electricity to retrieve the extensive capital investment. At the Puna Geothermal Venture (PGV), in southeast Hawaii, production has been active since 1993 and provides 25-30 megawatts of electricity to the island of Hawaii. The plant is built on only 2 km<sup>2</sup> but has thirteen wells, including both production and injection wells. All of the fluid extracted from the ground is reinjected, a process that likely contributes to the constant shallow microseismicity discussed below and in Chapter 2 (e.g. Eberhart-Phillips and Oppenheimer, 1984). In terms of this study the history of drilling and production at the PGV has been a critical check on the analyses. It is confirmed by production history that the most productive wells originate in the southwest corner of the PGV lease, as indicated by the fracture density analysis presented here. In addition, as discussed below, the presence of molten dacite was related to the high velocity P-wave tomographic results to indicate an intrusion and associated magma body. Ground truthing the geophysical methods has increased confidence that they will be effective in exploring other sites, including southeastern Montserrat.

This chapter presents geological and geophysical data to examine the hydrothermal fracture network of Puna, Hawaii. The structure at Puna is compared to Krafla, Iceland, another hydrothermal system that is an actively producing geothermal resource. These examples are used to evaluate how the structural setting and geophysical methods can be applied to identifying the hydrothermal system in southeastern Montserrat. On Montserrat the published evidence for a high temperature hydrothermal system includes surface manifestations of hot springs and related water chemistry (Chiodini et al., 1996). Based on the evidence from Hawaii and Iceland I suggest that the location of the hydrothermal system, e.g. the region of high temperature and

permeability, can be more specifically identified by the geologic structure around St. George's Hill, where there is a confluence of several faults.

### ***3.1 A confirmed fracture dominated hydrothermal system at Puna, Hawaii***

#### **3.1.1 Geologic setting**

The island of Hawaii is the last in the series of volcanic islands and seamounts in the Hawaiian-Emperor chain. The volcanism is associated with a mantle plume, or “hot spot,” that has resulted in the outpouring of voluminous ocean island basalt. Hawaii itself consists of five coalescing volcanoes, ranging in age from northernmost Kohala, 0.45 – 0.06 Ma to Kilauea, erupting since 1983 (Figure 17A).

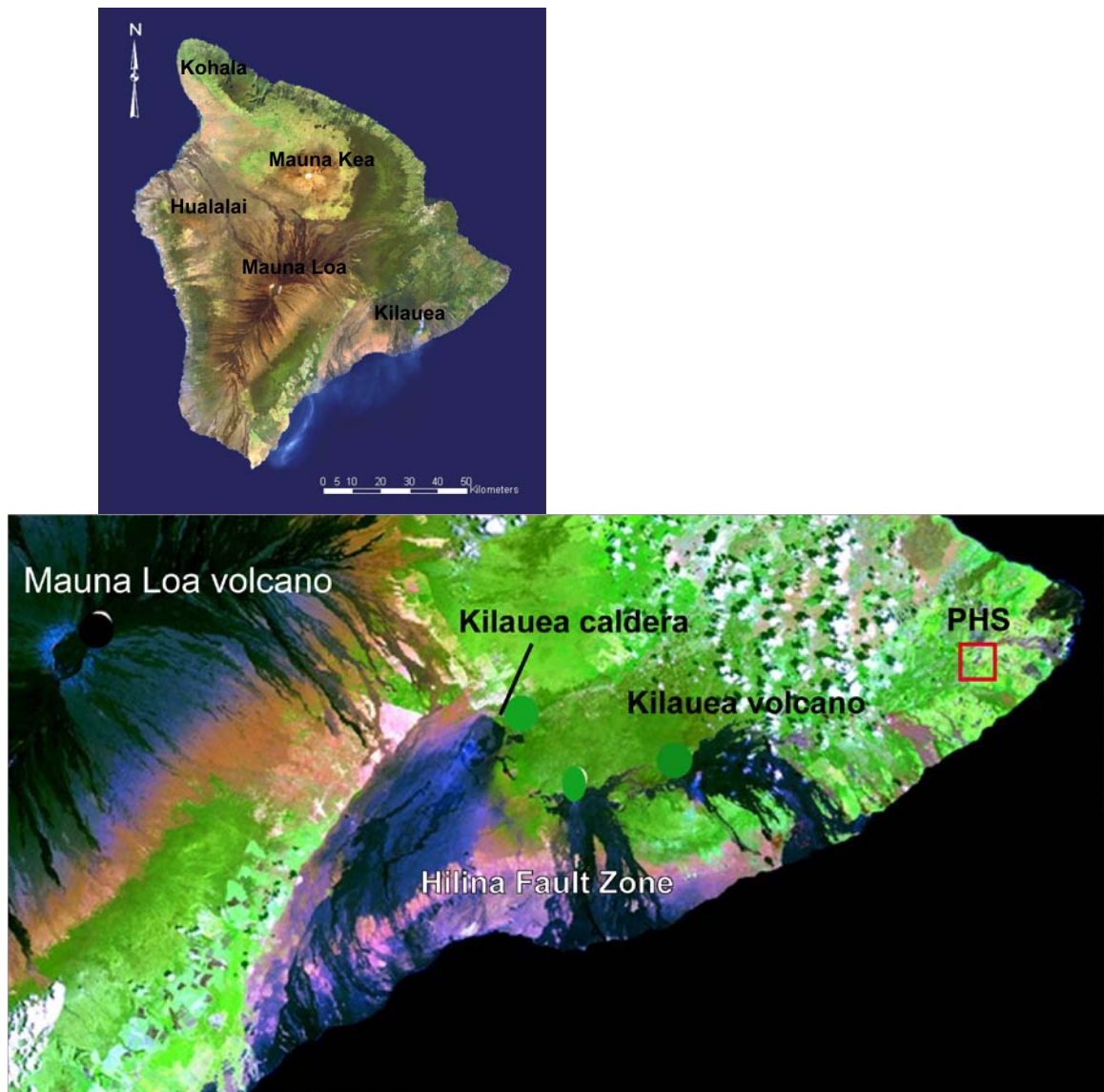


Figure 17: A. Satellite view of the island of Hawaii. Mauna Loa is the most massive volcano in the world, and Kilauea has grown on its southern flank. Note the rift systems of Mauna Loa and Kilauea, visible by the pattern of lava flows emanating from them. Image modified from <http://coralreefs.wr.usgs.gov/hawaii.html>.

17B. Landsat image of Kilauea volcano. The clearly visible black/grey shapes are lava flows along the East Rift Zone. The area of the Puna hydrothermal system (PHS) is marked by the red square. Image modified from <http://satftp.soest.hawaii.edu/space/hawaii/images/bigisle/kilauea.tm.706x375.jpg>

Kilauea has the structure of a shield volcano, a stack of lava flows that have accumulated as a massive mountain with gently sloping flanks (Figure 17B). The apex of the volcano consists of a caldera, from which some eruptions originate and under which is the conduit from which magma is sourced. Kilauea has been constructed as two major rift zones radiating from the caldera, the southwest and the east rift zones (ERZ). Puna, the site of the known hydrothermal system, is at the far end of the ERZ, called the lower east rift zone (LERZ) (Figure 17B). The ERZ continues offshore to the east as the Puna Ridge.

Figure 18.

**Figure 18 (continued): Geologic map of the LERZ around the PHS. Pink flows are emplaced since 1790. Orange units are 200-400 years old. Green units are 400-750 years old. Blue units are 750 to 1500 years old. Black circles/ellipses mark craters, cones, and fissures. Normal fault symbols mark normal faults. The yellow star is the location of the Puna Geothermal Ventures power plant. Red triangles are seismic stations. Modified from Moore and Trusdell (1991).**

The Puna hydrothermal system (PHS) is located along the LERZ in an area that has been largely resurfaced by lava flows in the last 400 years (Moore and Trusdell, 1991) (Figure 18). An actively producing geothermal power plant, Puna Geothermal Venture (PGV), is located on flows from 1955; the intrusion associated with the 1955 flows is thought to be the heat source for the hydrothermal system. The presence of the intrusion has been suggested by a high velocity zone in P-wave tomography (Shalev et al., 2008). The connection between the intrusion and the 1955 flows is suggested by isotope geochemistry analysis done on samples of dacitic melt obtained when standard drilling inadvertently penetrated the molten dacitic body (Marsh et al., 2008; Teplow et al., 2008).

### **3.1.2 Geologic structure**

Kilauea formed as a long, narrow structure on the south-dipping shoulder of the adjacent Mauna Loa flank (Figure 17B) (Lipman et al., 2006). The dominant fault structure is a series of south-dipping normal faults that have formed complex fault systems south of the caldera and along the upper ERZ. Faulting and land movement along the upper south flank of Kilauea, including the Hilina and Koa'e fault systems, has been documented extensively due to their relevance to both magmatism and the high threat of earthquake hazard (Delaney et al., 1998; Morgan et al., 2003; Owen et al., 1995; Parfitt and Peacock, 2001).



It has been less well documented what the fault system does along the LERZ. Normal faulting with rift-parallel strike has been mapped along the LERZ and extends as far as Puna (Moore and Trusdell, 1991; Parfitt and Peacock, 2001). Movements along the LERZ have been recorded in GPS surveys and reflect generally southward movement (Delaney et al., 1998; Owen et al., 1995) although it is not as clear as at the upper ERZ that there is flank movement associated with south-dipping faults.

### **3.1.3 Faults at Puna**

Prior to this work, faults at Puna were documented in two ways, geologic mapping and drilling. Geologic mapping shows that the dominant faulting in the area is normal faulting with a northeasterly strike and southeasterly dip (Moore and Trusdell, 1991) (Figure 18). In addition to a major, southeast-dipping normal fault, in this area there are several smaller faults, all northeast trending, parallel to the ERZ (Moore and Trusdell, 1991) (Figure 18). Most faults on both the northwest and on the southeast sides of the rift dip southeast (Figure 18), reflecting the inclination of Kilauea's flanks to slump seaward (Morgan et al., 2003).

At the PHS, segments of the LERZ are connected by a left step. While the entire area is encompassed by the broad ERZ, the step is clearly defined in terms of eruptive features including fissures, cones, and craters (Figure 18). The upper segment comes in from the west, from up rift towards the Kilauea summit and ends abruptly at Puhoi crater (Figure 18). Two kilometres to the north, a segment starts at Pu'u Honuaula and extends to the northeast, along which are located numerous craters, cones, and fissures. The PGV power plant is at Pu'u Honuaula. The segments are each associated with the dominant normal faulting.

The notable exception to the local dominance of southeast dipping normal faulting is a large, almost vertical antithetic fault that cuts through the PHS at the PGV. There is no evidence for this fault at the surface, but drilling operations at the PGV have encountered it at multiple depths. In addition, drilling has penetrated multiple northwest dipping fractures in which there are voids up to 10 m deep (Bill Teplow, personal communication). The antithetic fractures are the source of high fluid flow that provides the greatest productivity in the geothermal field.

Until 2006, geologic mapping and drilling were the only sources of information about the fracture system at the PHS. As discussed in Chapter 2, in 2006 we installed an array of eight borehole seismometers to record local seismicity. The microearthquake data, analyzed with shear wave splitting (SWS) and SWS tomography for crack density, have greatly improved our understanding of the fracture network.

### **3.1.4 Seismicity and fracture mapping at Puna Hydrothermal System**

Until now, seismic data at the LERZ have been limited but have suggested a major south-dipping fault; Owen and Burgmann (2006) show earthquakes deepening from the LERZ towards the ocean. The seismic data we have gathered also support the presence of an earthquake-producing, south-dipping fault that dips downward from the LERZ (Figure 19). As discussed in Chapter 2, the majority of earthquakes at the PHS are shallow and most likely associated with production and fluid reinjection at the geothermal plant. Deeper earthquakes occur under the shallow swarms, and the depths increase to the southeast, orthogonal to the rift orientation.

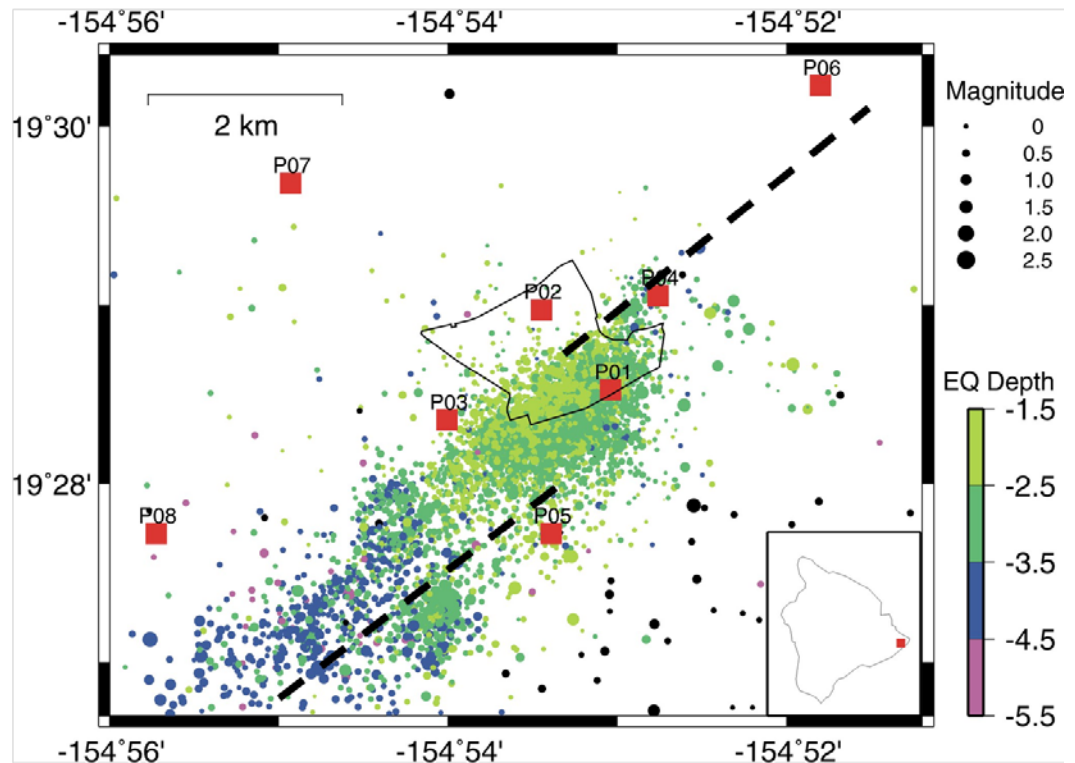


Figure 19: Earthquake depth and size along the Kilauea East Rift Zone at the Puna Hydrothermal System. The dashed line is the LERZ. Red squares are seismic stations. Colored dots are earthquakes; color indicates depth. Black dots are deeper than 5.5 km. The black shape represents the lease of the power plant. This figure has been updated from Fig. 7 in Chapter 2 to include earthquakes through June, 2009.

#### 3.1.4.1 Shear Wave Splitting Analysis

Shear wave splitting analysis is based on the physical characteristic of shear waves that they split into orthogonal waves when they travel through rock with anisotropic elastic properties. The split s-waves are polarized from a single s-wave; polarization occurs when the wave hits a boundary with new elastic properties such as a series of fluid filled fractures (Figure 20). In a fracture set the elastic constants are larger parallel to the fractures, through coherent rock, than in the compositionally varied

material perpendicular to the fractures. Therefore waves travel faster parallel to the fractures than perpendicular to them.

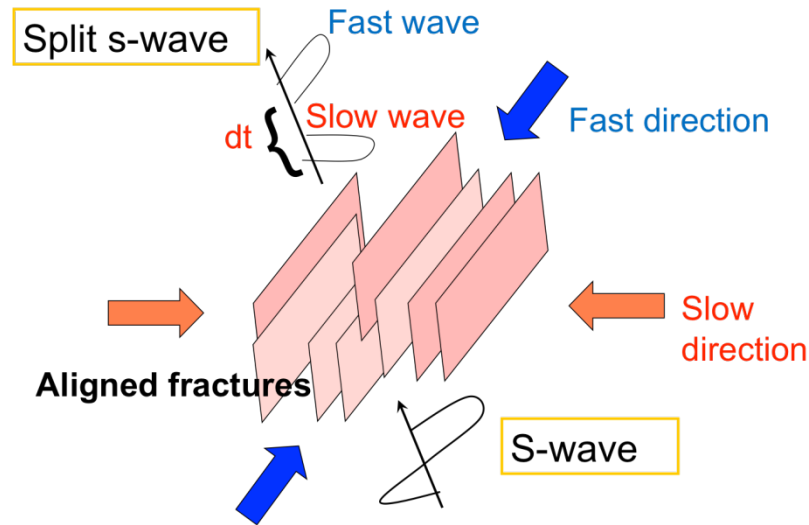


Figure 20: Cartoon illustrating the mechanism of shear wave splitting.

Two forms of information can be learned from a shear wave splitting analysis: 1. The dominant local fracture direction, based on the direction of the fast shear wave, and 2. The fracture density, or number of fractures in the designated volume, based on the time separation between the arrival of the fast and slow waves. As the fracture density increases, the delay of the slow wave behind the fast wave increases. In this study, I present both shear wave splitting data that indicates the dominant fracture direction under the PHS and also a fracture density study based on shear wave splitting tomography.

The shear wave splitting data indicate that at depth, between where the earthquakes occur and the recorders, the majority of earthquakes occur in a trend parallel to the rift (Figure 21). In Figure 21, rose diagrams indicate the bearing of the fast

direction of shear wave motion at each seismograph. The dominant fast shear wave direction at the central stations is northeast, parallel to the rift. The dominant direction at station P04, in the far northeast, is northerly, which is discussed below.

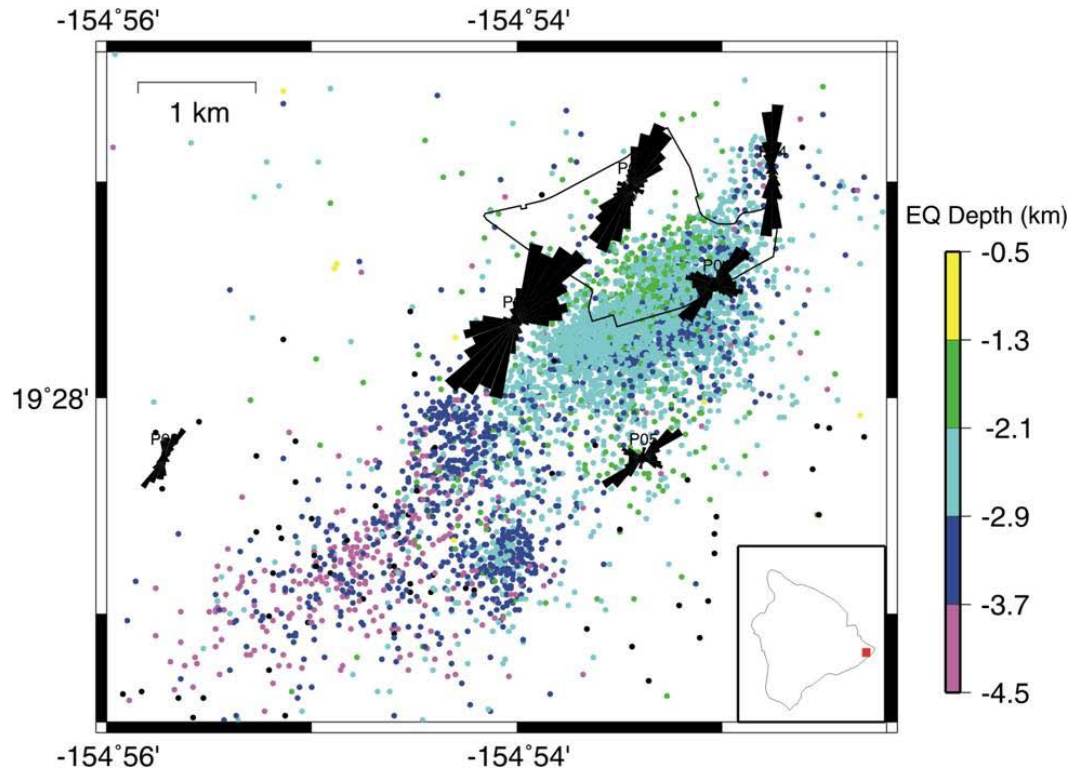


Figure 21: Rose diagrams of shear wave splitting data at the seismograph stations. Colored dots are earthquakes; color indicates depth. Stations 6 and 7 (see Figure 19) are not included due to lack of shear wave splitting data. This figure has been updated from Fig. 10 in Chapter 2 and to include earthquakes through June, 2009.

### 3.1.4.2 Fracture Density

The fracture density analysis identifies regions in which there are more or fewer open/ fluid filled fractures per unit volume. The method is to invert shear wave splitting

data in order to create a 3-dimensional, subsurface fracture density map. It is based on the principle that the time delay between the fast and the slow shear waves is related to the fracture density in the rock (Lou and Rial, 1997; Shalev et al., in preparation). One assumption of the inversion is that in the hydrothermal field fractures are largely vertical, fluid filled, and aligned parallel with a common strike. These assumptions are supported by previous studies of shear wave splitting behavior (Crampin and Lovell, 1991; Li, 1996).

At Puna, the region of highest fracture density is the south of the PHS at a depth of 1.5 – 2 km (Figure 22). This finding is consistent with the highest concentration of microearthquakes (Figure 19) as well as with the step in the rift (Figure 18).

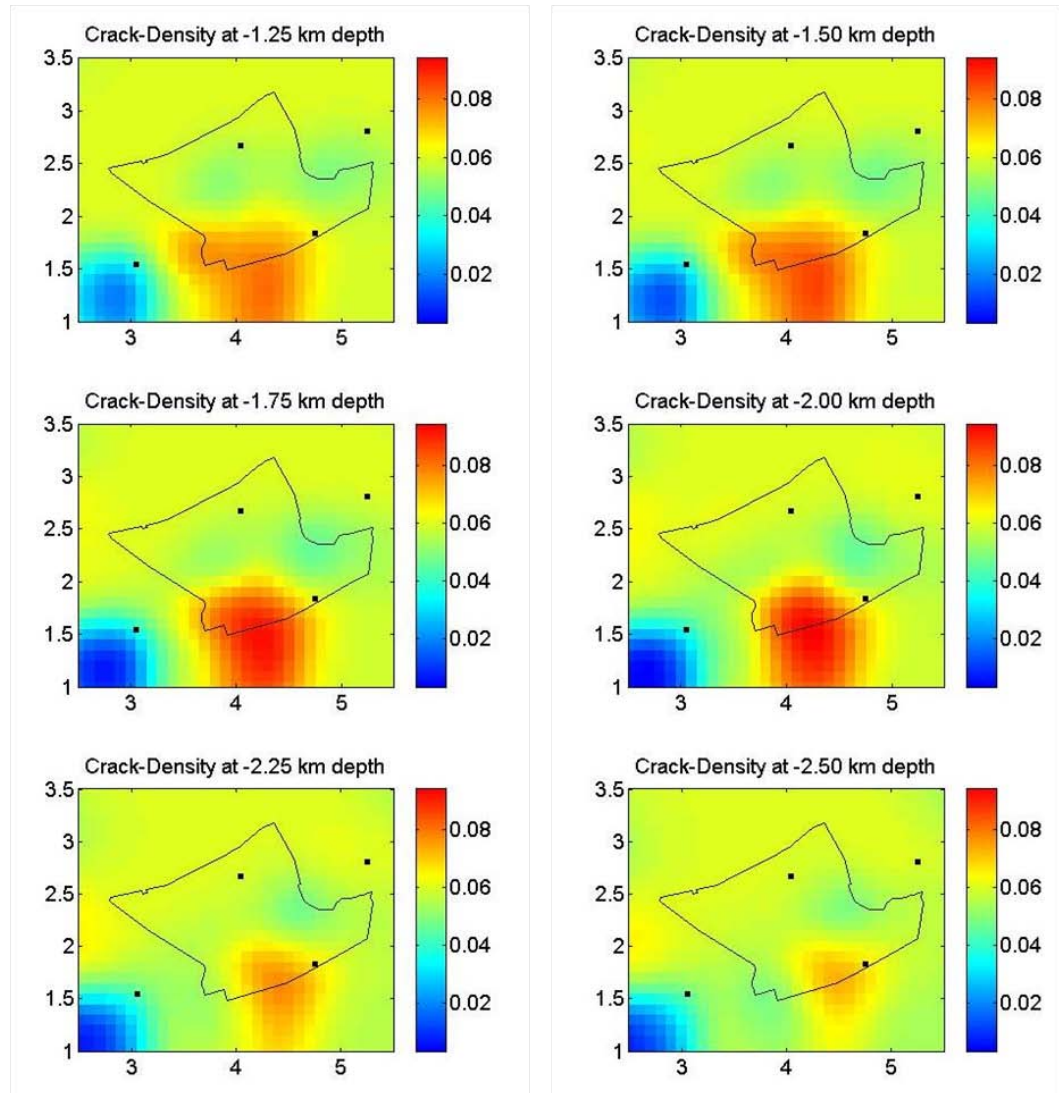


**Figure 22: Plots of crack density based on shear wave splitting tomography. Red is higher fracture density; blue is lower fracture density. X and Y axis labels are kilometers from an assigned origin. The black outline is the lease of the Puna Geothermal Venture power station.**

The region of high fracture density is also consistent with the areas of highest fluid production at the PGV (William Teplow, PGV consulting geologist, personal communication). The production records are proprietary to the PGV parent company, Ormat, so tables and diagrams are not included in the dissertation. However, it is

indicated that wells that penetrate the area where we calculate the greatest fracture density have higher fluid flow than wells elsewhere in the PGV lease. Having these data is a critical check and confirmation of the fracture density inversion method.

### **3.1.5 Transfer zone at Puna**

The PHS is between two rift segments, represented by craters, cones, and fissures as well as by southeast dipping normal faulting. The southern segment is marked by large, southeast-dipping fault scarps. Along the northern segment there are no large scarps, but field mapping has identified numerous normal faults (Figure 18) (Moore and Trusdell, 1991). At PHS, the faulting is offset by a north-south trending left step of ~ 2 km distance, and the PHS is located in the hanging wall of the northern fault segment (Figure 18). The geometry suggests that the PHS may be located in a relay ramp between the two fault segments.

A relay ramp connects the hanging wall of one normal fault to the footwall of a parallel normal fault that overlaps in map view and has the same dip (Peacock et al., 2000) (Figure 23A). Figure 23B is a photograph of a relay ramp at the Hilina fault system (HFS), south of Kilauea caldera (Figure 17B). Figure 23A illustrates the area of increased stresses in between the faults; the stresses are higher in the middle of the circle but fade moving away from the center.



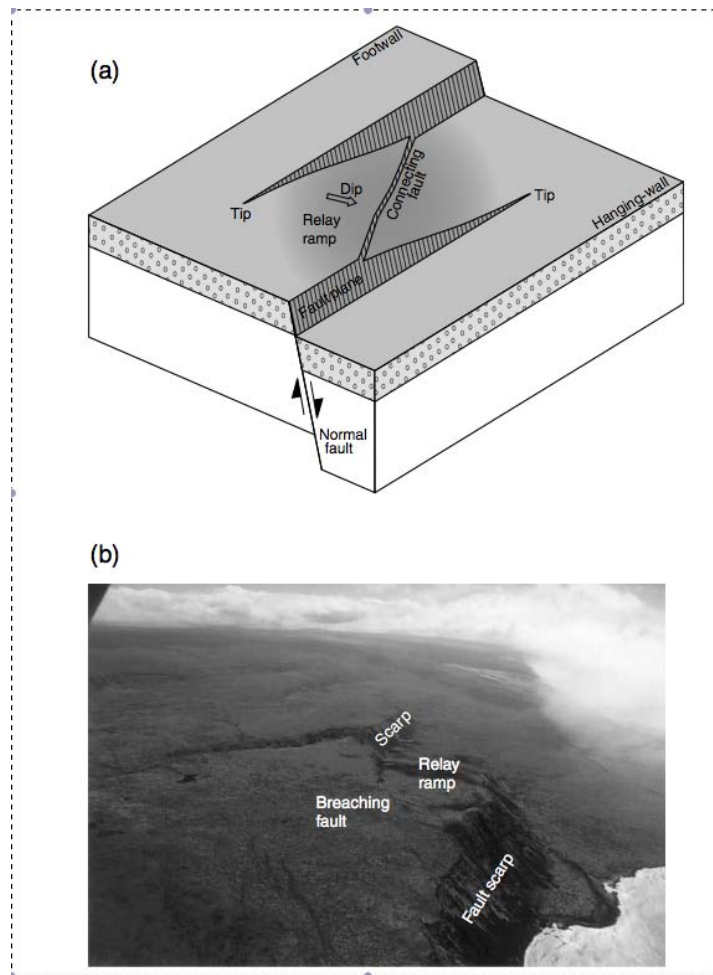


**Figure 23. A. Cartoon illustrating the structure of a relay ramp. The fading circle illustrates the area between faults that is the most affected by fault-related stresses. B. A photograph of a relay ramp on the Hilina Fault System. From Parfitt and Peacock (2001).**

In this particular case, the scarps are connected by a breaching fault, which is thought to be a late stage development of the relay ramp (Peacock and Parfitt, 2002). Earlier in the development of the ramp is the formation of cracks that are parallel to the main faults. It is likely that the cracks will connect through to the main fault of which the relay ramp is on the hanging wall, thus forming antithetic faults (Parfitt and Peacock, 2001).

One reason to suspect a relay ramp on the ERZ is that there are abundant relay ramps in various stages of development on the south flank of Kilauea at the Hilina and Koa'e fault systems (Parfitt and Peacock, 2001; Peacock and Parfitt, 2002). While the ERZ is a different structural regime and scale than the massively faulted HFS, they share the fundamental process of extension on the downward-sliding Kilauea flank.

At the PHS there are various pieces of evidence for a relay ramp. The first is the step in faulting, with overlapping but offset fault tips of normal faults, both dipping southeast (Figure 18 and 24). Also, drilling at the Puna Geothermal Venture has penetrated a large antithetic fault, shown in Figure 24, which is consistent with relay ramp formation (Peacock and Parfitt, 2002).

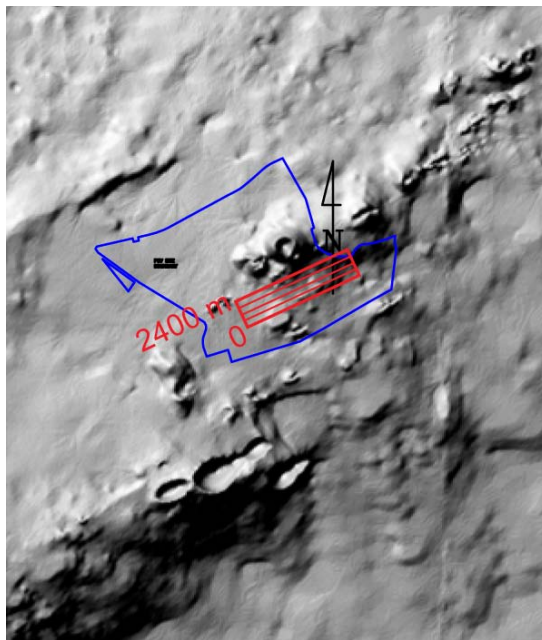


**Figure 24. DEM of the lower east rift zone. In blue is the lease boundary of the Puna Geothermal Venture. The primary fault dips SE from the ERZ. In red are contours marking depth of the antithetic fault as documented by drilling.**

In addition, there is no evidence in the field (at the surface) or in seismic data (at depth) that suggests a transform or strike-slip faulting across the PHS. Acocella et al.

(2005) showed that the size and extent of rifting influences the structures in the transfer zone. Wide extension zones such as back arc basins are more likely to form transfer faults whereas narrow rifts such as on Kilauea form relay ramps (Acocella et al., 2005).

### **3.1.6 Puna hydrothermal system in context: Krafla, Iceland**

Like Hawaii, Iceland is a largely basaltic volcanic island. Iceland is the only subaerial section of the Mid-Atlantic Rift (MAR) and marks the boundary between the North American and European plates. Thus Iceland is spreading, and Icelandic volcanism is centered along the rift zones that run through the middle of the island. The question of why Iceland has been uplifted to create an island is a debate in the literature; it has been accepted that in addition to the MAR, Iceland overlies a mantle plume that has sufficiently increased the volume of magmatism to form the island (Davies, 1999). It is also argued that there is not sufficient evidence for a “hot spot” under Iceland and that increased volume of melt can be explained by extension and decompression melting of recycled crust (Foulger and Anderson, 2005). Whether or not a plume exists, Iceland is a close analogue to Hawaii, consisting largely of basaltic lava with the dominant geologic structure in each place consisting of normal faulting due to extension by rifting.

Iceland has a long tradition of using geothermal resources and has a broad distribution of both low and high temperature geothermal fields, with high temperature resources concentrated in the rifts (Saemundsson and Johannesson, 2003). Fracture-controlled geothermal fields dominate both low and high temperature systems (e.g. Khodayar et al., 2010). The dominant normal faulting strike is approximately NE, parallel to the MAR, but extensive normal faults and fractures have been mapped with approximately orthogonal strike (Clifton and Einarsson, 2005; Einarsson and Eiriksson,

1982). In addition, unlike on Hawaii, there is extensive strike-slip and transform faulting.

In addition to its having been uplifted subaerially, another unusual geologic feature of Iceland is the presence of ~10-12 % silicic volcanism (Flude et al., 2010). This section will discuss one Icelandic volcanic center, Krafla, that consists of an ~100k yr old rhyolitic caldera that has been largely filled in by basaltic lava flows and which contains three productive geothermal fields (Armannsson et al., 1987) (Figure 25). I will compare the seismicity and structures of Krafla and Puna in order to create a geologic context and to emphasize methods particularly useful for exploring hydrothermal systems.

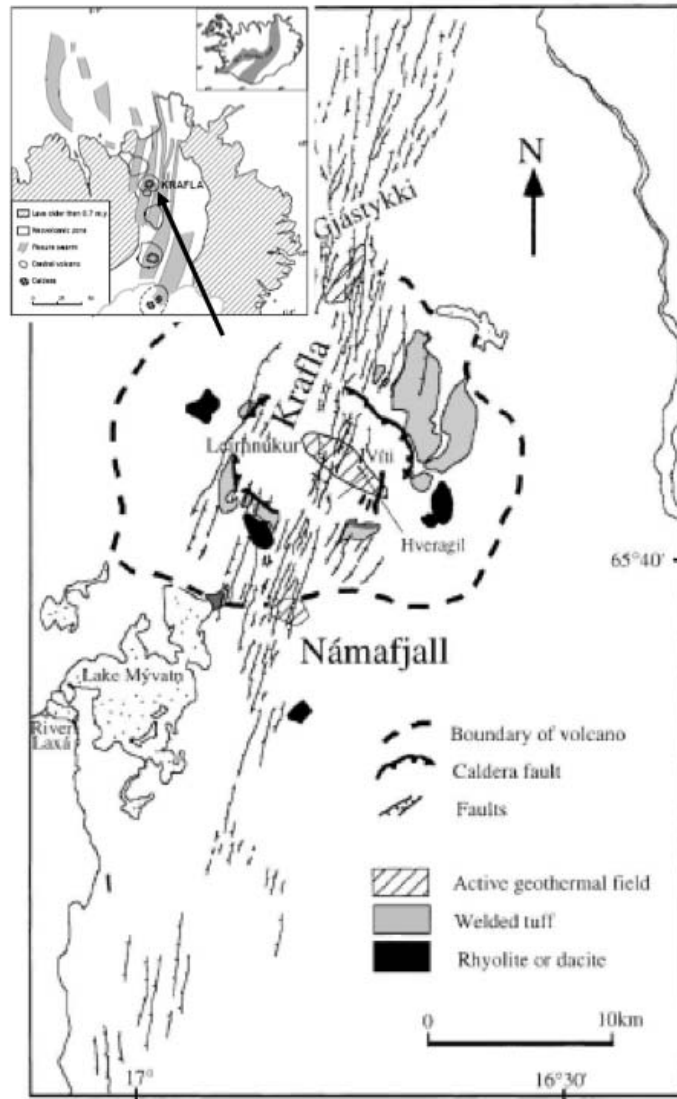


Figure 25. Geologic and structural model of the Krafla hydrothermal system. Caldera faults have a NW-SE trend while faults within the volcanic zone have a N to NNE trend. Welded tuff and rhyolite/dacite deposits occur at the margins of the caldera. From Onacha (2006).

### 3.1.6.1 Seismicity

In terms of seismicity, Puna and Krafla both have high levels of shallow seismicity (<3000 m) as compared to two other hydrothermal systems, Longonot, Kenya, and Casa Diablo, California (Onacha, 2006). This is of interest in terms of the

comparison with southern Montserrat as well, where background seismicity is low (see discussion below). Onacha (2006) suggests three reasons why Longonot and Casa Diablo might have lower seismicity than Krafla: 1. They are not near an active volcanic center, 2. They are further from an active tectonic region, and 3. They are not actively producing geothermal fields so are not removing steam, nor injecting hydrothermal fluids.

In Krafla the microearthquakes concentrated around the injection well, suggesting that injection of cool fluids from geothermal power generation generates microseismicity. This is consistent with locations of earthquakes in Puna, where there is a heavy concentration of microearthquakes at shallow depths where injection takes place. The third suggestion for lower seismicity is heavily indicated for Montserrat, which is a volcanic center in an active tectonic region but does not have geothermal power production.

#### **3.1.6.2 Fractures**

Like Puna, Krafla appears to have two directions of fracturing (Onacha, 2006), consistent with a permeable fracture mesh. The work done on Krafla included geologic mapping as well as a seismic array to record microearthquakes (MEQ) and a magnetotelluric (MT) study (Onacha, 2006). The combination of geophysical methods improved results over what was achieved at Puna in terms of fitting the results to the complex tectonic environment at Krafla. Adding the MT data allowed Onacha (2006) to discuss the depth of the fractures in more detail than possible at Puna, arguing that rift parallel fractures (NE trending) are shallower than older NW trending fractures. This information was then applied to the greater tectonic environment, suggesting that deeper fractures are associated with three major lineaments that extend off northern

Iceland. The interaction of these faults with the shallower fractures may allow for the upwelling of deep heated fluids (Figure 26).

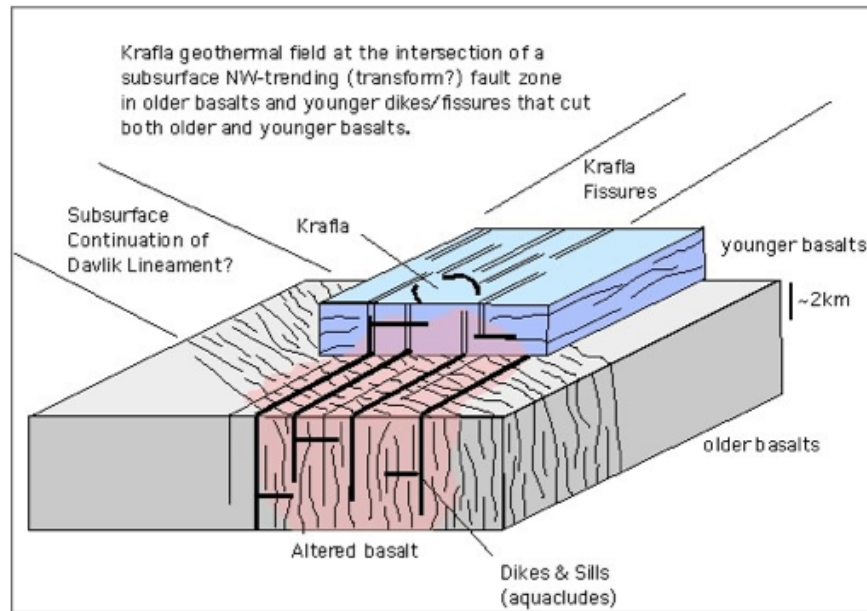


**Figure 26. The proposed structural cross section of the Krafla hydrothermal system. Subsurface NW-SE trending faults occur in older rocks, and younger fissure swarms trend in the NE-SW direction. The fissures are associated with dyke swarms that control lateral movement of hydrothermal fluids. From Onacha (2006).**

The hydrothermal system at Puna is structurally consistent with the system at Krafla. In each case, a network of fractures and faults leads to increased permeability that has been confirmed by highly productive geothermal power generation. While Puna is a small system located at a rift step between two normal faults, Krafla is a large caldera located along an extensively faulted rift zone. In each case, fractured rock due to the interaction of faults provides pathways for vertical fluid flow from the magmatic heat source.

The geophysical studies of the Puna hydrothermal system have indicated that, consistent with the majority of hydrothermal systems on Iceland (Khodayar et al., 2010),

fractures are the means by which hot fluid circulates through the system. Based on shear wave splitting results the majority of fractures are aligned along the Kilauea East Rift Zone down to depths of at least 4.5 km. In addition there are fractures approximately orthogonal to the ERZ as indicated with shear wave splitting. This is consistent with the location of the PHS on a rift step, an area generally known to have increased fracturing due to stresses from the adjacent faults.

In the next section, I will discuss the evidence for a high temperature hydrothermal system in southern Montserrat based on the findings from Puna and Krafla. Montserrat acts as a case study to examine the requisite fault geometry for high fracture permeability.

### ***3.2 Evidence for a Fracture Dominated Hydrothermal System at St. George's Hill, Montserrat***

Documented evidence of the existence of a hydrothermal system in southern Montserrat has been limited to the description of hot springs and fumaroles on Soufrière Hills volcano (SHV) and at Richmond Hill (e.g. Chiodini et al., 1996). Hot springs are part of the human history of Montserrat; before its destruction by the current eruption, the Montserrat Springs Hotel on Richmond Hill offered warm spring bathing to guests. In this paper, I discuss geophysical evidence for a high-temperature hydrothermal system; such a system is currently under intense scrutiny for its potential to provide Montserrat with geothermal electricity. I argue that in southern Montserrat fluid circulation is enabled by fault interactions and the associated fracture permeability.

#### **3.2.1 Geologic and tectonic setting**

Montserrat is a volcanic island located in the northeastern Lesser Antilles, the arc that has resulted from the subduction of the Atlantic under the Caribbean Plate (Figure



27A). On Montserrat three andesitic volcanic centers have been active, Silver Hills (~ 1-2 Ma), Centre Hills (~0.4-1 Ma), and Soufrière Hills – South Soufrière Hills (~0.3 Ma to present) (Figure 27B and Figure 28). The centers build by repeated dome building and collapse, accumulating piles of pyroclastic and debris flows and deposits. As discussed in chapter 3, these deposits accumulate in large wedges offshore from direct flows and erosion and also as major collapse features; it is estimated that at least 50% of erupted products are transported offshore (Le Friant et al., 2004).

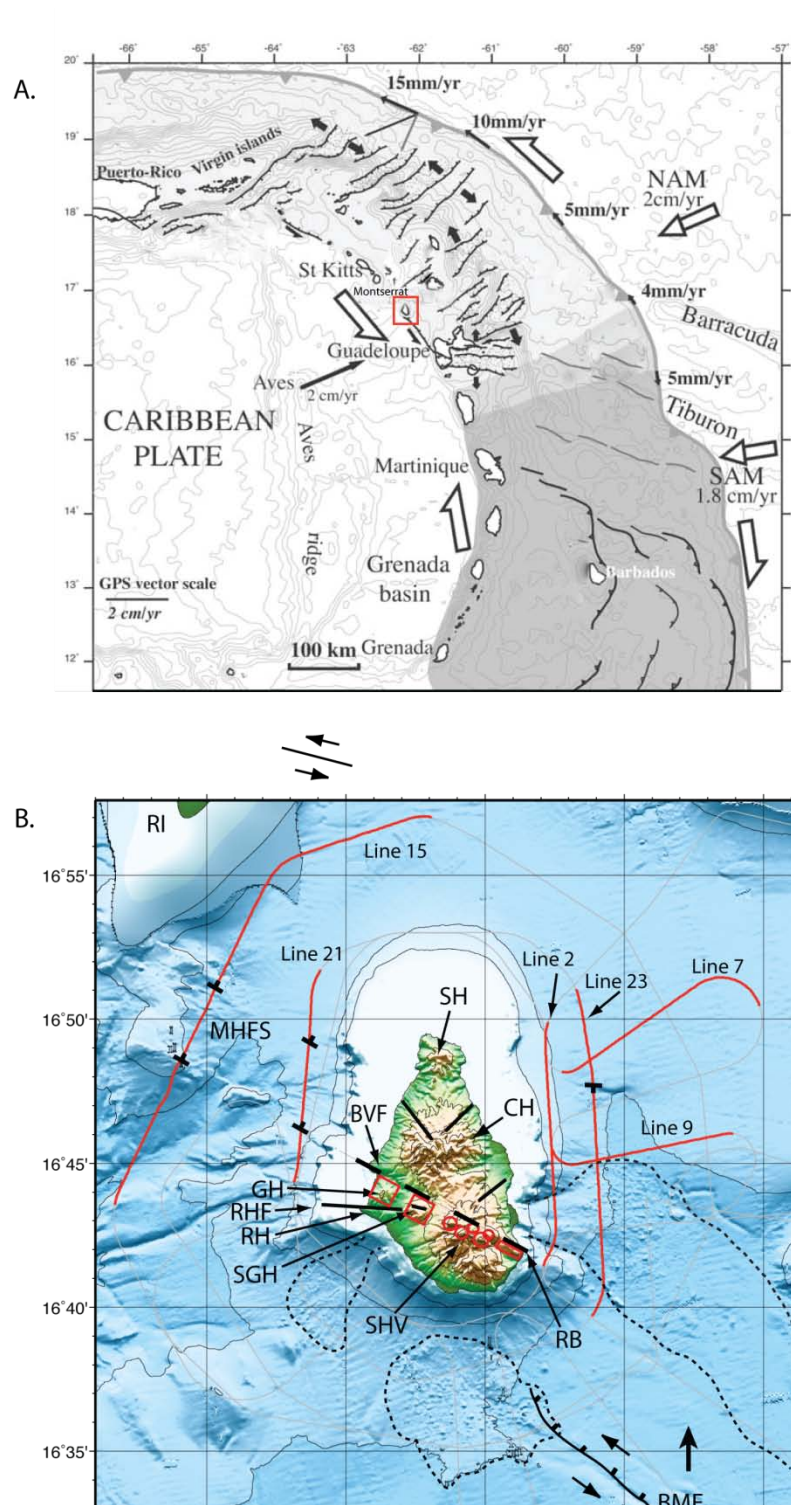


Figure 27.

**Figure 27 (continued): A. Tectonic model of Lesser Antilles, modified from Feuillet et al. (2002). Faults and extension directions described in Feuillet et al. (2002).**

**White arrows: Motion between North American, South American, and Caribbean plates (DeMets et al., 2000; Weber et al., 2001). White half arrows: Sinistral and dextral motion along the trench. Thin black arrow: GPS movement at Aves Ridge.**

**B. Montserrat bathymetry and tectonic model. Grey curved line: Track of the RRS James Cook. Red Lines are discussed in chapter 3. Red circles: Volcanic centers.**

**Red squares: Tectonic uplifts. Black fault symbols: Normal faults from profiles, apparent dip as indicated. Thick dashed lines: Major fault of the fault systems, including BVF and possible extension to RB. Large black arrows: Extension direction (Feuillet et al. 2001). Dotted lines: Gravity flow deposits as described in Le Friant et al.**

**(2004). The fault to the north is inferred from 1985-1986 Redonda earthquake mechanisms (Girardin et al., 1991; Feuillet et al., 2002). BMF, Bouillante-Montserrat fault system; BVF, Belham Valley fault; CH, Centre Hills; GH, Garibaldi Hill; MHFS, Montserrat-Havers fault system; RB, Roche's Bluff; RFS, Redonda fault system; RH, Richmond Hill; RHF, Richmond Hill fault; RI, Redonda Island; SGH, St. Georges Hill; SH, Silver Hills; SHV, Soufrière Hills Volcano. Bathymetry map from Institut de Physique du Globe de Paris and M. Paulatto, NOCS**

The tectonic setting of Montserrat is complicated due to its location at the upper arc, where oblique subduction causes large scale left-lateral shear accommodated by regional extension and arc-perpendicular normal faulting (Feuillet et al., 2001)(Figure 27A). Feuillet et al. (2010) have shown that Montserrat is at the southern edge of the Havers-Montserrat Fault System (HMFS), part of a series of regional right-stepping en echelon normal fault systems.



**Figure 28:** . Oblique aerial view of Montserrat from the SW. The grey land cover is ash, mud, and pyroclastic debris from multiple dome collapse and lahar events since 1995. Dashed black lines are faults. BVF Belham Valley Fault. RHF Richmond Hill Fault. SGH is St. George's Hill, GH is Garibaldi Hill, RH is Richmond Hill.

Montserrat is in a step between the Bouillante-Montserrat fault system and the HMFS, which may cause increased fracturing, permeability, and magmatism. The extensional faulting of southern Montserrat appears to have influenced the location of volcanism, as the volcanic centers of SHV align in a WNW-ESE trend. The faulting has influenced the topography of the region, causing the major uplifts of St. George's and Garibaldi Hills along the Belham Valley Fault (BVF) (Harford et al., 2002; Kenedi et al., 2010b).

The BVF is the most prominent fault trace on Montserrat (Figure 27B and 28). It is a WNW-trending, NNE-dipping normal fault that appears to extend offshore where it appears on marine seismic reflection profiles (Kenedi et al., 2010b) (Figure 4, Chapter 1). Figure 27B includes a sketch of other observed fault traces on Montserrat, which appear as NW and NE trending conjugate sets. The trend of the BVF is more WNW than the other traces, which has led to conjecture about the locally dominant stresses (see discussion, Chapter 1).

The presence of deep faulting in conjugate sets is supported by both field observation and geophysical evidence. Gravity data indicate a NNW-striking fault through Centre Hills (Hautmann et al., 2010). Seismicity occurred on a NE-striking trend through SHV connected to the 1995 initiation of the SHV eruption (Aspinall et al., 1998) (Figure 30).

The Richmond Hill fault (RHF, Figure 27B and 29) trends approximately west and dips north (Feuillet et al., 2010), with Garibaldi Hill and perhaps St. George's Hill (SGH) on its hanging wall. The RHF is significant for its interaction with the BVF, as the region between the two faults is the most likely center of the hydrothermal system.

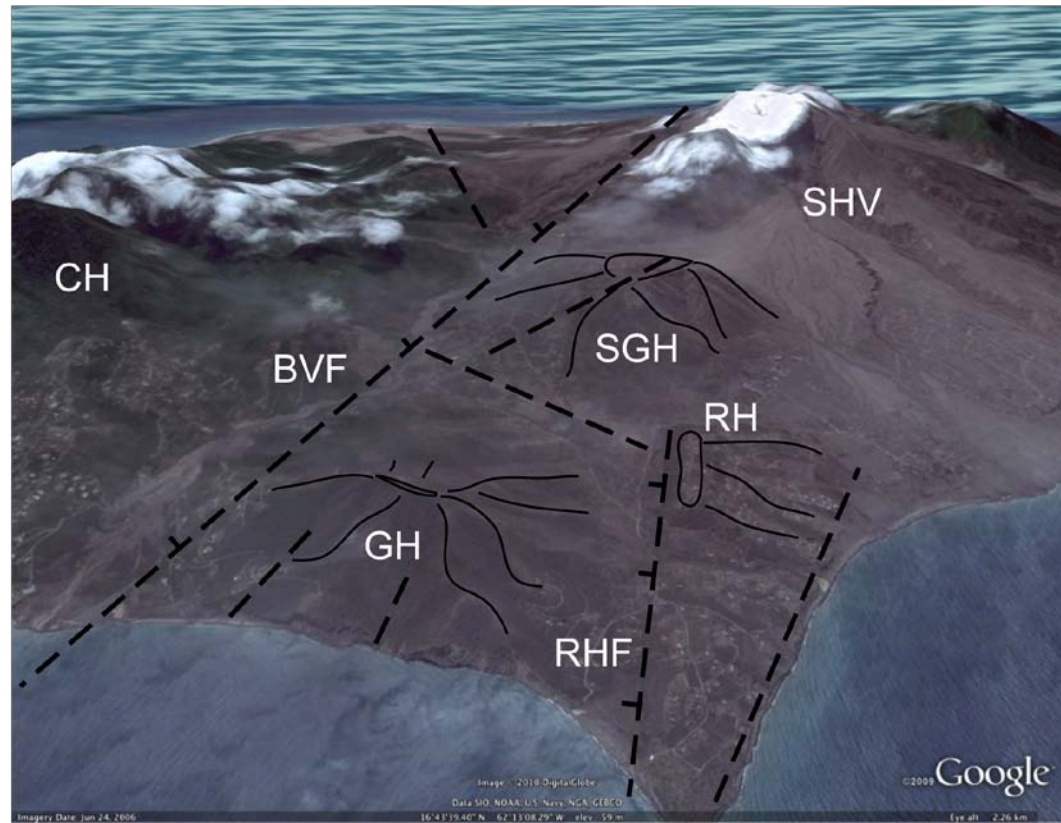


**Figure 29: View of southern Montserrat from the west. Curving lines illustrate the ridges descending from the tops of the hills. CH is Centre Hills, BVF is Belham Valley Fault, SGH is St. George's Hill, GH is Garibaldi Hill, SHV is Soufriere Hills Volcano, RH is Richmond Hill, RHF is Richmond Hill Fault.**

Figure 29 is a close-up view of the Belham Valley (and associated fault line), Garibaldi Hill, Richmond Hill, SGH, and SHV. The Richmond Hill fault (RHF) is visible as a north-facing scarp south of SGH. There is also a linear structure on top of SGH, which has been mapped as normal faulting (Feuillet et al., 2010).

### **3.2.2 Seismicity and fracture mapping at St. George's Hill**

Detailed seismic studies as described at the Puna hydrothermal system have not been completed around SGH. Attempts at a shear wave splitting study (e.g. Ryan et al., 2009) have been unsuccessful due to imperfect placement of the seismic stations not

deployed for the purpose. For shear wave splitting analysis the azimuth from the earthquake to the seismograph must be less than 15 degrees. in order to record the split shear wave. Using seismometers from the network of the Montserrat Volcano Observatory as well as the SEA-CALIPSO experiment did not yield sufficient data. The consequence is that a fracture density study is not possible, as it depends on shear wave splitting results.

The application of findings from Puna to Montserrat is possible through the demonstration that the region where faults interact/intersect is also the region of increased permeability and fluid circulation. In Puna the area of highest fracture density is demonstrated by the consistently high performance of production wells in that area compared to outside it. The area is located on the rift where normal faulting steps to the left, creating an area with increased stresses and fracturing. I now examine southeastern Montserrat, in the area under St. George's Hill, and show that an analogous situation exists.

#### **3.2.2.1 Seismicity**

Frequent seismic swarms have been mapped in southern Montserrat and specifically under the uplifted St. George's Hill (SGH). Swarms occurred under SGH in 1897-98, 1933-37 (Powell, 1938), 1966-67 (Shepherd et al., 1971), and 1995-1997 (Aspinall et al., 1998)(Figure 30). The 1995-1997 swarms have been relocated with a new velocity model and are thought to have occurred at depths of ~2 – 4 km (Miller et al., 2010).



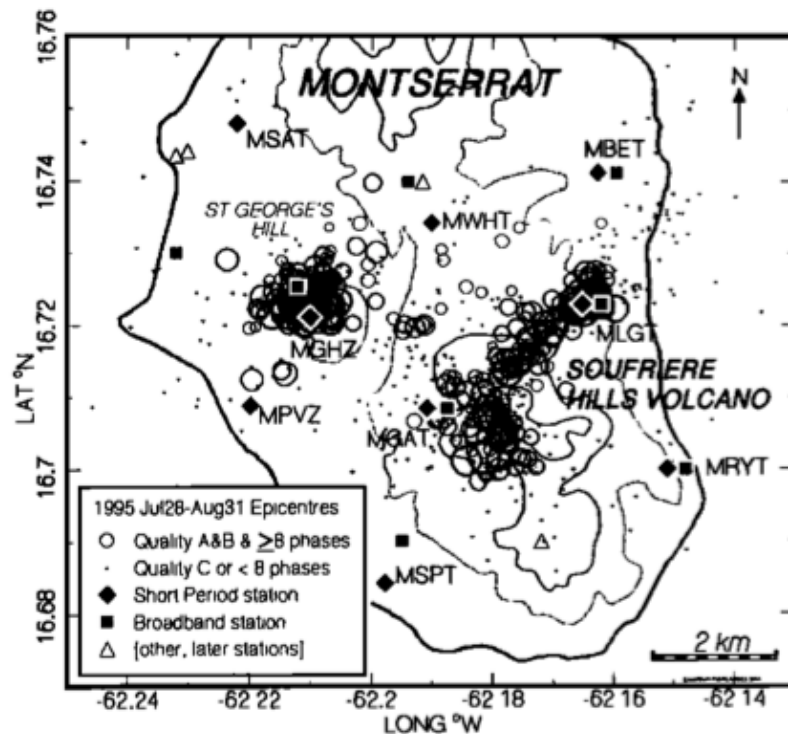


Figure 30: Seismicity under southern Montserrat, August 1995. Clusters occurred under SHV, in a NE linear trend from SHV, and under SGH. Depths range from ~2-6 km.

Other than the swarms, seismicity is focused at the SHV and associated with the ongoing eruption (e.g. Roman et al., 2008). Recent studies using seismicity to resolve patterns of local stress have resulted in a complex picture suggesting that stresses are affected by both the magmatic system and the location of Montserrat in a tectonic step (Kenedi et al., 2010b; Miller et al., 2010). Other than the swarms, the seismicity under SGH is relatively low, as recorded by surface seismometers from the Montserrat Volcano Observatory array. For an effective study of the seismicity under SGH, a targeted borehole seismic array is required, as installed at Puna.



### **3.2.2.2 Resistivity**

Resistivity is a measure of how strongly a material opposes the flow of electric current; in hydrothermal systems, resistivity is primarily associated with the cation exchange capacity of fluids and clays. It has been shown that resistivity values are linked to the permeability and temperature at different depths of the fluid circulation system (Onacha, 2006).

Resistivity can be measured with a combined set of magnetotelluric (MT) and time domain electromagnetic (TDEM) methods. In MT, the apparent resistivity is obtained from the scaled ratio of the time varying, local electric field to the magnetic field. TDEM provides a control by generating a time varying magnetic field and electric current from an artificial source.

A recent MT/TDEM study on Montserrat (Ryan et al., 2009) produced resistivity data at the ground surface, 500, 1000, and 4000 meters below sea level (mbsl); I present the deeper results due to the increased relevance for the high temperature system (Figure 31). West and southwest of SGH at 1000 mbsl there are trends of low resistivity that coincide with the trace of local northwest and northeast trending faults. Faults relate to resistivity in terms of the material within them; low resistivity may be associated with low permeability, clay-rich alteration products from hydrothermal activity and also with open fractures containing sea water or hydrothermal fluids.

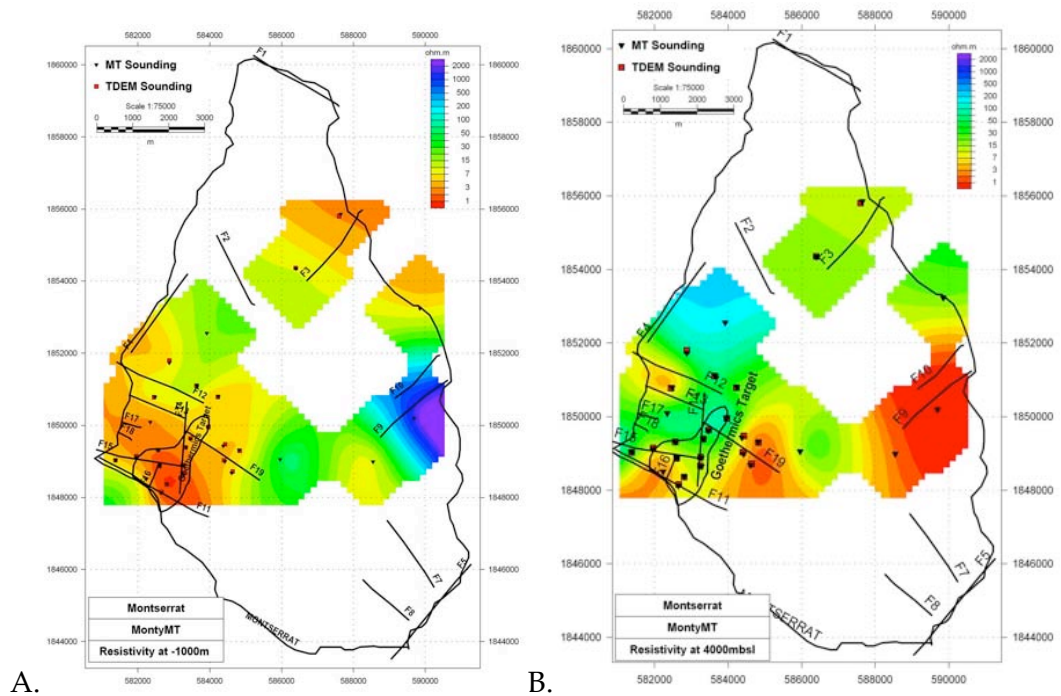


**Figure 31: Resistivity map from Magnetotelluric survey. 11A. Resistivity at 1000 m depth; 11B. Resistivity at 4000m depth. Red indicates lower resistivity and blue indicates higher resistivity. Straight lines indicate faults. From Ryan et al. (2009).**

The active hot spring system on Richmond Hill suggests that at shallow levels, faults act as outflow zones. This would suggest active flow and permeable, fluid-rich faults. It does not preclude the inevitable accumulation of altered material, but in a system that is affected by active faulting, there will be a constant shift of fluid pathways as some become closed by mineral precipitation and others open to accommodate the local stress. The other aspect of the hot springs being located on Richmond Hill is that it is consistent with other areas, including Puna, where the hot springs emerge some distance away from the central hydrothermal system.

At 4000 mbsl the results suggest a heat source for the volcano, with very low resistivities specifically located under SHV. In addition, resistivities are low directly under SGH, suggesting a heat source for the hydrothermal system. The higher resistivities in the region of intersecting faults indicate that 4000 mbsl is deeper than the main system and consists of more coherent rock. This result is also indicated by 3D p-wave tomography, as described below.

### **3.2.3 3-D Tomography**

The 3D tomographic study was based on data from the December, 2007, SEA CALIPSO experiment (Shalev et al., 2010, Appendix A). In the experiment, the research vessel RRS James Cook circled Montserrat while towing an airgun that emitted 4413 shots over 77 hours. Data from 58 land based seismometers were used to construct a 3D P-wave velocity model at depths down to ~4 km (Figure 32).

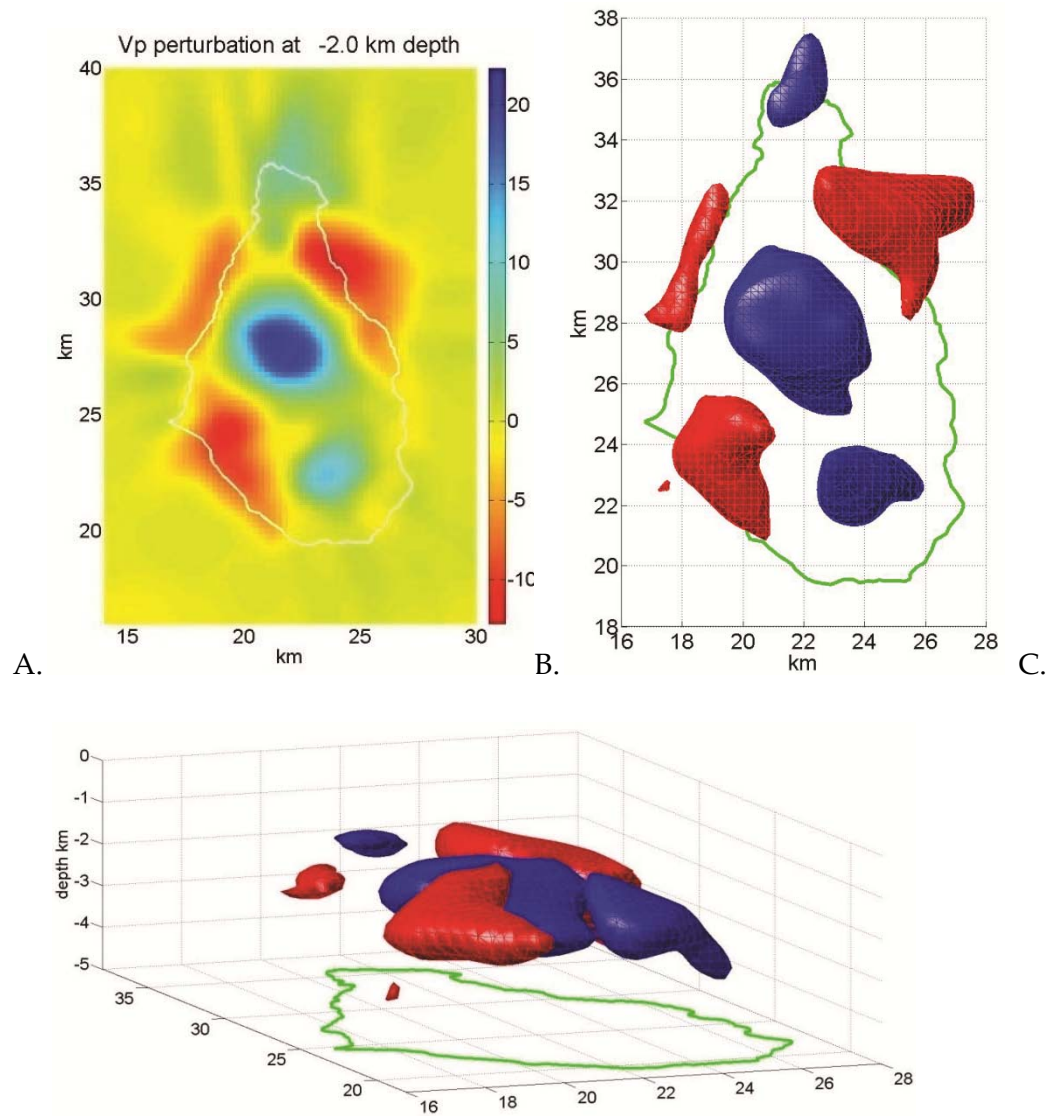


**Figure 32: A. Vp tomography results as perturbation from the average velocity at each depth. Blue is faster velocities; red is slower velocities. Map view at 2 km depth. B, C. 3D isosurfaces of velocity anomalies. The blue surfaces define anomalies that are >6% faster than average. The red surfaces define anomalies that are >6% slower than average. B is the map view, C is viewed from the southwest.**

The low velocity zone to the southwest encompasses SGH and the proposed hydrothermal system. As with the low resistivity data, the tomography indicates that the

lowest velocities are at 1-2 km depth and sloping to the southwest. The correlation between low p-wave velocities and low resistivity is most likely hydrothermal alteration of volcanic debris and deposits to clays. A fault network is the most likely connection to enable circulating fluids throughout this large volume of rock, at least 2 km deep and 2 km across.

### **3.2.4 Permeability at fault intersections: Transfer Zones**

To maintain a high temperature hydrothermal system ( $>250^{\circ}\text{C}$ ), fluid must be able to circulate within the hydrothermal regime, transferring heat by convection. This requires a level of permeability,  $\kappa > 10^{-16} \text{ m}^2$ , found in fractured igneous rocks ( $\kappa = 10^{-15} - 10^{-11} \text{ m}^2$ ), in contrast to unfractured igneous rocks in which  $\kappa = 10^{-16} - 10^{-23} \text{ m}^2$  (Rowland and Sibson, 2004, Figure 1). Thus fractures are the key to fluid circulation and heat transfer. However, fractures in hydrothermal systems are tenuous; permeability changes as precipitated minerals blocks the fluid pathways. Fractures also may be blocked by the thermo-elastic effects of changing temperature in plastic rock. Fracture systems that include active faults are associated with persistently high permeability (Barton et al., 1995; Sibson, 2001).

Fault interactions result in increased permeability in two fundamental places, at intersections and in the intermediate region between non-intersecting but adjacent faults. At fault intersections the permeable sections of the faults combine to enhance fluid flow (Nielson et al., 1996). Where faults are adjacent but not intersecting, the stresses in the intermediate region cause increased fracturing (e.g. Curewitz and Karson, 1997). In both cases, a fracture network forms that supports the formation of voids and increased permeability.

#### **3.2.4.1 Probable location of hydrothermal system on Montserrat**

The faulting found at both Puna and St. George's Hill is primarily extensional, each site occurring along a large normal fault. In southern Montserrat there are fewer data than in Puna, in particular a lack of drilling to document underground fractures and to test if and where there is a large concentration of hot hydrothermal fluid. However there is strong evidence for a high-temperature hydrothermal system and the requisite fracture network. The Belham Valley fault and the Richmond Hill fault are adjacent and may be connected by intermediate faults (Figures 28 and 29), suggesting even at the surface a complex fracture network.

Evidence for the fracture network is also seen at depth. Under St. George's Hill there have been repeated earthquake swarms; known depths range from 2 – 4 km (Figure 30). Low resistivity values suggesting hydrothermal alteration coincide with fault trends at ~1 km (Figure 31). Tomographic results also indicate extensive hydrothermal alteration in the entire region around SGH, producing areas with low p-wave velocity values between 2 – 4 km depth.

Both the PHS and the area around St. George's Hill constitute transfer zones, where stress is shifted between faults. Both the relay ramp and the region of interacting faults is characterized by increased permeability by the formation of a fracture network (Curewitz and Karson, 1997). Evidence for a fracture network at the PHS includes the two directions of fast polarized shear waves (Figure 21) and the high levels of seismicity at depth (Figure 19). Based on the earthquake locations, it appears that the faults dip very steeply down to at least 5 km along the ERZ and to greater depths to the southeast (Figure 19). Seismic reflection data off Montserrat as well as earthquake locations also

suggest that the faulting around SGH is deep enough to coincide with the hydrothermal system.

One important note about the seismicity at fault junctions is that while fractures are associated with fault interactions and resulting stresses, it is likely that to some extent the seismicity occurs in a cloud with unmappable microfaults. Hill (1977) modeled earthquakes swarms as occurring in a network mesh, which would be consistent with a cloud of seismicity that cannot be resolved into specific faults. As is seen in the shallow seismicity at Puna (Figure 19) and under SGH (Figure 30), it is expected that the cloud would have “fuzzy” edges, with the majority of earthquakes near the center and the numbers diminishing with distance.

The same pattern of fracture mesh has been documented as enabling fluid circulation in hydrothermal systems (Rowland and Sibson, 2004; Sibson, 1996; Sibson, 2000). The mesh, i.e. an ever-shrinking pattern of faults to microfaults, is consistent with looking at fractures as a fractal network, which has been documented and quantified by multiple authors (Leary, Sibson, Peacock) and which begs for continued work. For understanding hydrothermal fluid circulation, knowing how numbers of fractures and their intersections can be quantified and modeled is the critical work of the future. These studies will determine the success of the practical applications of the science, both exploring for mineral resources that have precipitated out in hydrothermal fracture systems and turning high-temperature hydrothermal systems into geothermal electricity.

## **Appendix A: 3-D Seismic velocity tomography of Montserrat from the SEA-CALIPSO offshore/onshore experiment**

The appendix includes the text of the following published work, in which I played a major role and was the second author.

Shalev, E., Kenedi, C. L., Malin, P., Voight, B., Miller, V., Hidayat, D., Sparks, R. S. J., Minshull, T., Paulatto, M., Brown, L., and Mattioli, G. (2010) Three-dimensional seismic velocity tomography of Montserrat from the SEA-CALIPSO offshore/onshore experiment. *Geophysical Research Letters* 37, L00E17, doi:10.1029/2010GL042498

### **3-D Seismic velocity tomography of Montserrat from the *SEA-CALIPSO* offshore/onshore experiment.**

Shalev, E.<sup>1,2</sup>, Kenedi, C.L.<sup>1,2</sup>, Malin, P.<sup>1,2</sup>, Voight, B.<sup>3</sup>, Miller, V.<sup>3</sup>, Hidayat, D.<sup>3</sup>, Sparks, R.S.J.<sup>4</sup>, Minshull, T.<sup>5</sup>, Paulatto, M.<sup>5</sup>, Brown, L.<sup>6</sup>, Mattioli, G.<sup>7</sup>,

1. Institute of Earth Science and Engineering, University of Auckland, Auckland, NZ.
2. Earth & Ocean Sciences, Duke University, Durham, NC 27708
3. Department of Geosciences, Penn State University, University Park, PA 16802, USA.
4. Department of Earth Sciences, University of Bristol, Bristol BS8 1RJ, UK
5. National Oceanography Centre, University of Southampton, Southampton, SO14 3ZH, UK
6. Department of Geosciences, Cornell University, Ithaca, New York, USA.
7. Department of Geosciences, University of Arkansas, Fayetteville, AR 72701

### **Abstract**

The *SEA-CALIPSO* experiment in December 2007 incorporated a sea-based airgun source, and seismic recorders both on Montserrat and on the adjacent sea floor. A high quality subset of the data was used for a first arrival P-wave velocity tomographic study. A total of more than 115,000 traveltime data from 4413 airgun shots, and 58 recording stations, were used in this high-resolution tomographic inversion. The experiment geometry limited the depth of well resolved structures to about 5 km. The most striking features of the tomography are three relatively high velocity zones below each of the main volcanic centers on Montserrat, and three low velocity zones flanking Centre Hills. We suggest that the high velocity zones represent the solid andesitic cores of the volcano complexes, characterized by wave speeds faster than adjacent volcanoclastic material. The low velocity zones may reflect porous volcanoclastic material and/or alteration by formerly active hydrothermal systems.



## Introduction

We present a P-wave velocity tomography study on Montserrat, W.I., based on the *SEA-CALIPSO* offshore/onshore active source experiment. (*Seismic Experiment with Airgun-source – Caribbean Andesitic Lava Island Precision Seismo-geodetic Observatory*). Montserrat is a 10 x 16 km volcanic island in the northern half of the Lesser Antilles arc. The Soufrière Hills volcano (SHV) dominates the southern two thirds of the island and has been active and dynamic since July 1995 [Young, 1998]. Various lines of evidence have been used to estimate the depth of over 5 km to a magmatic reservoir, including petrology [Barclay *et al.*, 1998], deformation [Mattioli *et al.*, 1998, Voight *et al.*, 2006], and the approximate base of seismic activity [Aspinall *et al.*, 1998]. We attempted to identify the regions of variable velocity under the island, especially under the volcanic centers, and to inquire whether magmatic storage areas could be recognized under the SHV.

## The seismic tomography experiment

The plan was to install a dense array of seismometers on or near the island, and to encircle the island with a ship towing an eight-component GI airgun with a total capacity of 2600 in<sup>3</sup> shooting at 1 minute intervals. [Voight *et al.*, in prep]. A major focus concerned obtaining high resolution data under the active and hazardous volcano. Since SHV occupies the southeastern part of the island, most stations were located in safe areas in the north and northwest, and the ship's radial tracks were mostly to the south and east (Fig. 1). The short distance between the target zone and the furthest recorder limited the maximum depth of seismic ray penetration below SHV.

Two deployment designs and types of seismic recorders were used on land in *SEA-CALIPSO* [Voight *et al.*, in prep]: 29 Reftek 130 recorders, with 3-component Mark Products L22 2 Hz sensors, and 204 Texans (Reftek 125), with single vertical component Mark Products L28 4.5 Hz sensors. In order not to bias the inversion with the closely spaced Texan reflection geometry, only one in ten Texans was included in the tomographic grid.

The seismic network used in the tomographic inversion consisted of 58 stations, including 25 Reftek 130s, 19 Texans, 7 Ocean-Bottom Seismometers (OBSs) with 4.5 Hz sensors, and 7 permanent Montserrat Volcano Observatory (MVO) broadband stations in the exclusion zone. For the duration of the experiment, all instruments recorded continuously, at 250 or 100 samples per second depending on recorder type. The only exception was a subset of six Texans, part of a refraction line in the Belham Valley, that was shut down for several hours mid-experiment for a data quality test.

The data recorded in the experiment was mostly of high quality with easily identifiable first arrivals (Figure 2). Weak signals were recorded from some of the longer ray paths. The first arrivals formed a smooth progression throughout the section; thus,

even when a few shots did not show the first arrival, the arrival time could still be identified. In this study we analyzed and picked only the first arrivals and did not use secondary phases. These phases are addressed in other works [Paulatto *et al.*, 2010].

## **Data**

The 77 hours of shooting resulted in 4413 shots recorded by 58 stations for a total of 115,158 ray paths. Of all the shots, stations in the north had up to 91% of identifiable first arrivals, while stations around SHV had fewer than 35% identifiable first arrivals due to high attenuation in the younger volcanic deposits. Stations near the coast recorded few first arrivals due to high ambient noise from ocean waves. The data were filtered between 3-15 Hz to correspond with the frequency content of the airgun signal. First arrivals were picked manually and only clear signals were used; thus, uncertainty was assumed to be the same for all first arrivals.

## **Seismic tomography method**

The first-arrival time data were inverted for a 3D P-wave velocity model of Montserrat and the surrounding ocean using the tomography code from *Shalev and Lees* [1998]. This method uses a Cubic B-spline description of the 3D volume, and the LSQR algorithm to invert the data. This inversion method simultaneously minimized both data misfit and model roughness, which allowed the researcher to choose the desired level of smoothness. The inversion also allowed for station and shot corrections. A separate damping parameter was used for each type of inversion unknown: velocity model, station correction, and shot correction.

Although the 3-D velocity structure extended to 1 km above sea level, ray tracing was computed from sources at sea level to the actual elevation of each station. The length of the water section of each path was assumed to be the depth to the sea floor below each shot. A constant velocity of 1.5 km/s was used to calculate travel time in the water.

We began with a 1D velocity model, using Cubic B-spline interpolation to be consistent with the 3-D inversion. The 1D model for this study was derived from the data using the Levenberg–Marquardt non-linear minimization procedure [Press *et al.* 1992]. There were two options for the starting velocity model: a) A single starting model for the whole target area, or b) Two starting models, one for land and one for ocean. We tested both types of starting model using the same damping and smoothing parameters, and while the end results were similar, the final RMS of residuals was smaller with two starting models. Therefore, we derived two 1D velocity models, one each for land and for ocean (Fig. 2). The boundary between land and ocean was defined as the bathymetric line at 200 m water depth. The derived 1D models differed from the ones used for synthetic ray-path modeling. In particular, the final land model was faster than the ocean model at all depths penetrated by first arrival rays; this resulted in a shallower maximum depth for the turning rays, and reduced the imaging depth.

The total target cube for the 3D inversion (see Fig. 1) was 50 x 45 x 8 km. Horizontal velocity grid spacing was 0.5 km in the land area, 1 km for the ocean near the land, and 5 km near the boundaries. Vertical grid spacing was 0.5 km to a depth of 5 km, and 1 km below 5 km. A smaller grid spacing of 0.25 km was tested for the center of the land area but showed no improvement.

To check for resolution of the 3D inversion, we ran a checkerboard test based on the starting 1D velocity models. The cell size of the checkerboard was 1.5 x 1.5 x 1.5 km, with the specified variation  $\pm 12.5\%$ . A consistent recovery of the pattern was observed to a depth of 4 km in the area of good ray coverage under the island. However, the amplitude of the recovered anomalies was only about two-thirds of the starting amplitude. At 5 km depth, some of the checkerboard anomalies retained their shape but most were blended and smeared. There was no reliable resolution below 5 km depth.

Another resolution problem was the tradeoff between station correction and velocity in the top 1 km of the model. The process of allowing for station corrections in the inversion removed most of the variability from the top of the model, and running the inversion without station corrections resulted in a substantially larger residual RMS. The final inversion allows for damped station correction. Nevertheless, it is possible that some velocity anomalies in the top 1 km are not imaged because of this compromise.

## Results

The tomographic inversion converged after 5 iterations. Several sets of damping and smoothing parameters were tested, and the major velocity anomalies were stable regardless of these parameters. The 3D inversion reduced the RMS of the residuals from 167 ms to 80 ms for a variance reduction of 77%. Results of the tomographic inversion are shown in Figure 3 and Figure 4. The maximum lateral variation is about  $2 \text{ km s}^{-1}$ , which is similar to the results obtained from Deception Island [Zandomenighi *et al.*, 2009].

The most notable features in the  $V_p$  structure are high velocity anomalies below all three volcanic centres of Montserrat at about 2 to 3 km depth. The most prominent of these is the anomaly below Centre Hills, with a similar but less intense anomaly under SHV (Fig. 3A). This inversion result was not unexpected, because the average station residual contours in Figure 1 also show positive (fast) residuals for stations near the volcanic centers. The top boundaries of these high velocity anomalies are not clear, due to the tradeoff between station correction and velocity at shallow depth. When the inversion ran without station corrections, the largest fast anomaly under Centre Hills reached the surface, but with higher RMS misfit.

Other large and consistent anomalies are the low velocity regions on the flanks of the volcanic centres. There are three such anomalies to the northeast, northwest, and southwest of Centre Hills. These anomalies are stable regardless of inversion parameters. The east-west cross section (Fig. 3D) shows both a high velocity body under SHV and a low velocity anomaly west of SHV. The appearance that the two anomalies are elongated

down and away from the center of the island may be an artefact of the rays coming from the perimeter to the center. However, the geometry of the main, high amplitude anomalies of Figure 4 is stable.

## Discussion

The acquisition geometry of the SEA-CALIPSO tomographic experiment was laid out to target the possible active concentration of magma at >5 km depth under the SHV. The actual seismic velocities beneath and surrounding Montserrat turned out to be faster than expected, thus turning back most of the refracting seismic energy at depths <5 km. The result was that first-arrival P-wave tomography produced a reliable image of the velocity structure between ~1 and 5 km in depth and extending approximately to the shelf break.

Within this region are six prominent velocity anomalies enclosing perturbations either 6% above or below the average velocities at each depth (Fig. 4). Following *Paulatto et al.* [2010], we suggest that the fast anomalies beneath the three constructional volcanic centers may correspond to solid andesitic structural elements in the volcanic cores. The cores would consist of dense, crystallized rock comprising dome cores, sills, dikes, or irregular-shaped intrusions, and adjacent altered zones with silica precipitation, that are seismically faster than the surrounding material, the latter including either lavas from submarine volcano building, and volcanoclastic deposits (talus, block-and-ash flows, lahars etc.). Crystalline cores are consistent with the work of *Harford and Sparks* [2001], who suggest that recurring intrusions solidify at depths up to ~3 km under SHV. This is supported by other evidence that suggests that dikes may rise to 1.5-2 km under SHV, from shallow storage zones [*Mattioli et al.* 1998; *Hautmann et al.* 2009; *Voight et al.*, this volume]. It is likely that intrusions have some lateral extent [e.g., *Voight et al.* 2006], and that considerable volumes of unerupted magma remain in storage zones during the current eruptive activity. The high velocities observed are consistent with nodules found Montserrat-wide as inclusions in eruption products [*Kiddle et al.*, this volume].

The locations of the low-velocity anomalies northeast of Centre Hills and west of SHV suggest a relationship with the volcanic centers and the features may represent syn-volcanic apron deposits. A potential weakness with this hypothesis lies in the fact that these low-velocity features extend to 3-4 km depth. While the weight of the volcano could have been responsible for some degree of crustal flexure and burial of surface material, it cannot easily account for such a depth. There is evidence for buried volcanoclastic fan deposits at 1.5-2 km depth off the east coast of Montserrat [*Kenedi et al.*, this volume].

Another possibility is that the low-velocity features result from hydrothermal alteration, shown to lower seismic velocities in oceanic rocks [*Carlson*, 2001]. Evidence for hydrothermal circulation beneath the Garibaldi-Richmond-St. Georges Hills includes anomalous seismic activity [*Rowe et al.*, 2004], as well as surface hot springs, hot water

in boreholes, and a warm pond near Richmond Hill [Chiodini *et al.*, 1996]. Tectonic faulting in the Belham Valley [Kenedi *et al.*, this volume] may be related to this hydrothermal activity. Hydrothermally altered rocks occur at the surface in parts of the Silver Hills [B. Voight, unpublished observations]. A recent MT study on Montserrat shows good correlation between these low velocity zones and low resistivity at 1-4 km depth [G. Ryan, personal communication]. Hydrothermal alteration due to geothermal fluid circulation is a frequent phenomenon in volcanic areas, and geothermal systems are commonly several km in diameter, approximately the size of the low-velocity anomalies in Montserrat. The position of the three low-velocity anomalies around Centre Hills may suggest that geothermal activity was more prevalent about 1 – 0.4 Ma, when Centre Hills was active.

### Acknowledgments

We thank the National Science Foundation Continental Dynamics, Geophysics, and Instrumentation & Facilities Programs, the British Geological Survey, Discovery Channel TV, and the British Foreign & Commonwealth Office for funding the SEA-CALIPSO project, the IRIS PASSCAL Instrument Center for providing instrumentation and technical support for the project, and the many people who worked hard aboard the ship or on land to deploy instruments and collect seismic data during December 2007. Thanks also to the good people of Montserrat who allowed us the use of their properties for instrument deployment.

### References

- Aspinall, W.P., A.D. Miller, L.L. Lynch, J.L. Latchman, R.C. Stewart, R.A. White, and J.A. Power, (1998), Soufriere Hills eruption, Montserrat, 1995-1997: volcanic earthquake locations and fault plane solutions, *Geophys. Res. Lett.*, *25*, 18, 3397-3400.
- Barclay, J., M.J. Rutherford, M.R. Carroll, M.D. Murphy, J.D. Devine, J. Gardner, and R.S.J. Sparks, (1998), Experimental phase equilibria constraints on pre-eruptive storage conditions of the Soufriere Hills magma, *Geophys. Res. Lett.* *25*, 18, pp 3437-3440.
- Carlson, R. L. (2001), The effects of temperature, pressure, and alteration on seismic properties of diabase dike rocks from DSDP/ODP Hole 504B, *Geophys. Res. Lett.*, *28*, 20, 3979-3982.
- Chiodini, G., R. Cioni, A. Frullani, M. Guidi, L. Marini, F. Prati, and B. Raco, (1996), Fluid geochemistry of Montserrat Island, West Indies, *Bull. Volcanol.*, *58*, 380-392.
- Harford, C. L. and R. S. J. Sparks, (2001), Recent remobilization of shallow-level intrusions on Montserrat revealed by hydrogen isotope composition of amphiboles, *Earth Planet. Sci. Lett.* *185*, 285-297.

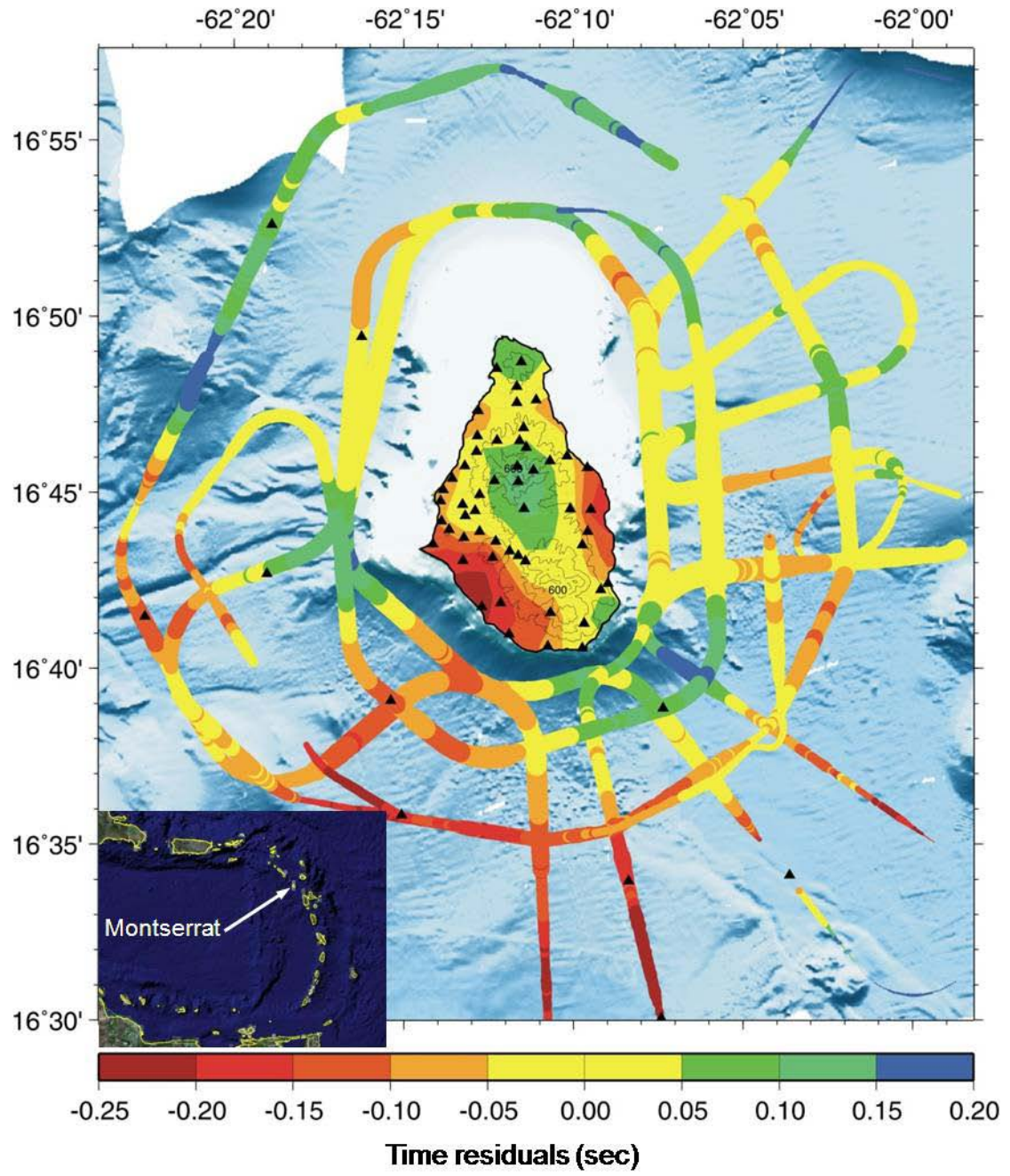
- Hautmann, S., J. Gottsmann, R.S.J. Sparks, A. Costa, O. Melnik, and B. Voight, (2009), Modeling ground deformation caused by oscillating overpressure in a dyke conduit at Soufrière Hills Volcano, Montserrat, *Tectonophysics*, 471, 87-95.
- Kenedi, C.L., R.S.J. Sparks, P.E. Malin, B. Voight, S. Dean, T. Minshull, M. Paulatto, C. Peirce, and E. Shalev, (2010), Active faulting and oblique extension influence volcanism on Montserrat (West Indies): Evidence from offshore seismic reflection profiles, *Geophys. Res. Lett.*, *Special Section on Montserrat*, this volume.
- Kiddle, E., B. Edwards, S. Loughlin, M. Petterson, R. S. J. Sparks, and B. Voight, (2010), Crustal structure beneath Montserrat, Lesser Antilles, constrained by xenoliths, seismic velocity structure and petrology, *Geophys. Res. Lett.*, *Special Section on Montserrat this volume*.
- Mattioli, G.S. T.H. Dixon, F. Farina, E.S. Howell, P.E. Jansma, A.L. Smith, (1998), GPS measurement of surface deformation around Soufriere Hills Volcano, Montserrat from October 1995 to July 1996, *Geophys. Res. Lett.*, 25, 18, 3417-3420.
- Paulatto, M., T.A. Minshull, B. Baptie, S. Dean, J.O.S. Hammond, T. Henstock, C.L. Kenedi, E.J. Kiddle, P. Malin, C. Peirce, G. Ryan, E. Shalev, R.S.J. Sparks and B. Voight, (2010), Upper crustal structure of an active volcano from refraction/reflection tomography, Montserrat, Lesser Antilles. *Geophys. J. Int.*, 180(2), 685-696, doi:10.1111/j.1365-246X.2009.04445.x.
- Press, W.H., S.A. Teukolsky, W.T. Vetterling, and B.P. Flannery (1992), Numerical recipes in C (2nd ed.): the art of scientific computing, Cambridge University Press, New York.
- Rowe, C. A., C. H. Thurber, and R. A. White, (2004), Dome growth behavior at Soufriere Hills volcano, Montserrat, revealed by relocation of volcanic event swarms, 1995-1996, *J. Volc. Geotherm. Res.* 134(3), 199-221.
- Shalev, E., and J.M. Lees, (1998), Cubic B-splines tomography at Loma Prieta, *Bull. Seismol. Soc. Am.*, 88, 256-269.
- Voight, B., et al., The SEA-CALIPSO volcano imaging experiment on Montserrat: Aims, Plans, Campaigns at Sea and on Land, and Lessons Learned. In preparation.
- Voight, B., C. Widiwijayanti, G.S. Mattioli, D. Elsworth, and D. Hidayat, (2010), Magma sponge hypothesis and stratovolcanoes: the case for a compressible reservoir and quasi-steady deep influx at Soufrière Hills Volcano, Montserrat. *Geophys. Res. Lett.*, *Special Section on Montserrat*, this volume.
- Voight, B., A.T. Linde, I.S. Sacks, G.S. Mattioli, R.S.J. Sparks, D. Elsworth, D. Hidayat, P.E. Malin, E. Shalev, C. Widiwijayanti, S.R. Young, V. Bass, A. Clarke, P. Dunkley, W. Johnston, N. McWhorter, J. Neuberg, P. Williams, (2006), Unprecedented pressure increase in deep magma reservoir triggered by lava-dome collapse. *Geophys. Res. Lett.*, 33, 3, L03312.
- Young, S.R., R.S.J. Sparks, R. Robertson, L. Lynch, A.D. Miller, J.B. Shepherd, and W.A. Aspinall (1998), Overview of the Soufriere Hills volcano and the eruption, *Geophys. Res. Lett.*, 25, 18, 3389-3392.

Zandomeneghi, D., A. Barclay, J. Almendros, J. M. Ibañez Godoy, W. S. D. Wilcock, and T. Ben-Zvi (2009), Crustal structure of Deception Island volcano from P wave seismic tomography: Tectonic and volcanic implications, *J. Geophys. Res.*, *114*, B06310, doi:10.1029/2008JB006119.

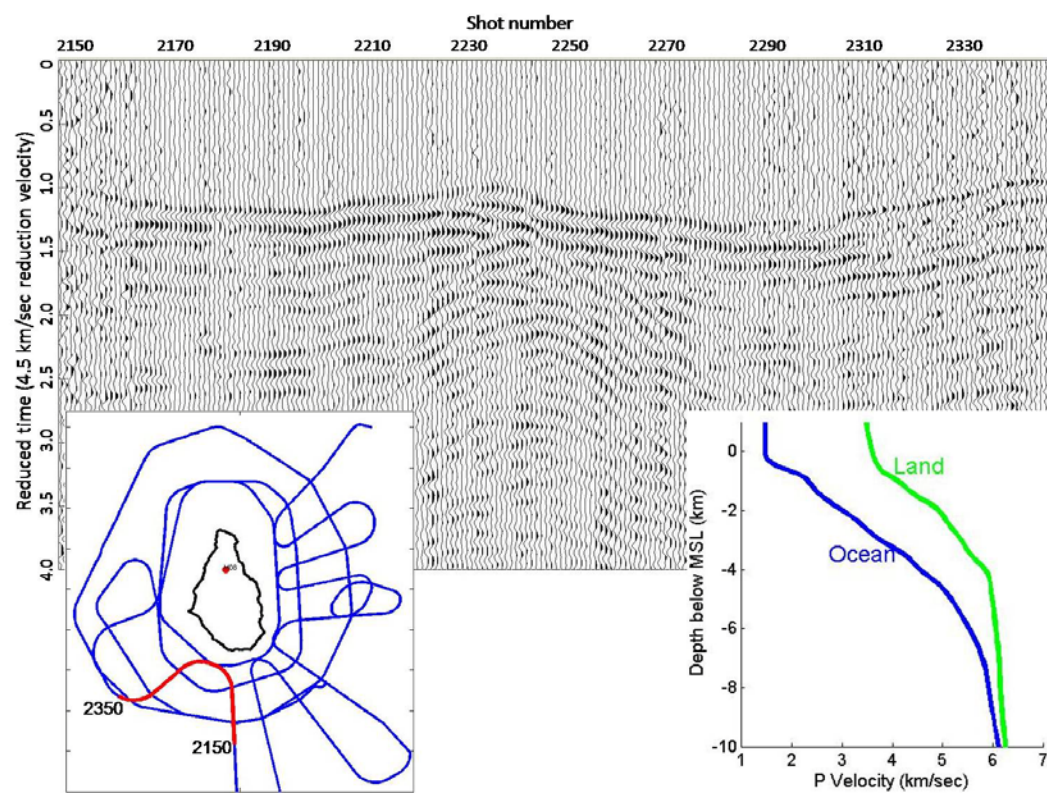
## Figure captions

- Figure 1. Map of SEA CALIPSO 3D tomography area showing bathymetry, topography contours, ship track, station locations, and average time residuals for shots and land based recorders. Black triangles mark the seismic stations included in the tomographic inversion. The stations offshore are ocean bottom seismometers. Colors stand for the average residuals (time computed minus time observed) in seconds where red represents slow and blue represents fast. On land, the colors contour the average residuals; on water, colors represent the average residual for each shot. The width of the ship track line is proportional to the number of seismic stations that recorded the airgun blast from a particular point on the track.
- Figure 2. Example of a record section of the vertical component, as recorded by Station M08 on the north slope of Centre Hills, from shots to the southwest of the island. Reduction velocity = 4.5 km/sec. First arrivals are very clear at approximately 1 sec reduced time. Ship path is shown on the left insert in red. 1-D velocity models for land and ocean are shown in right insert.
- Figure 3. Vp tomography results displayed as perturbation from the average velocity at each depth. Blue represents faster velocities and red represents slower velocities. The top three panels are map view slices through the target volume at depths 2.0 (A), 3.5 (B), and 5.0 (C) km. The black line through the panels marks the location of the cross section (D) across the SHV. The outline of Montserrat is a white line on all map view slices.
- Figure 4. 3-D isosurfaces of velocity anomalies. The blue surfaces define anomalies that are >6% faster than average. The red surfaces represent anomalies that are >6% slower than average. A is a map view. B is a view from the east southeast. C is a view from the south southwest.

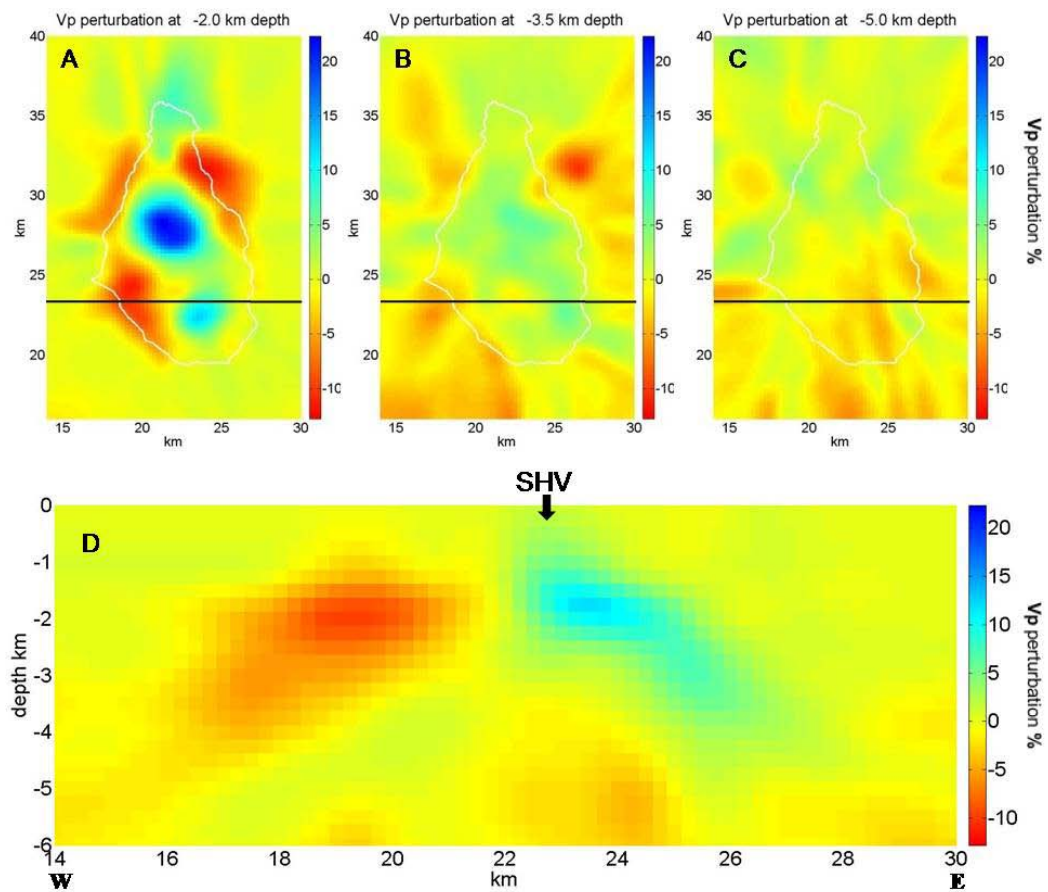




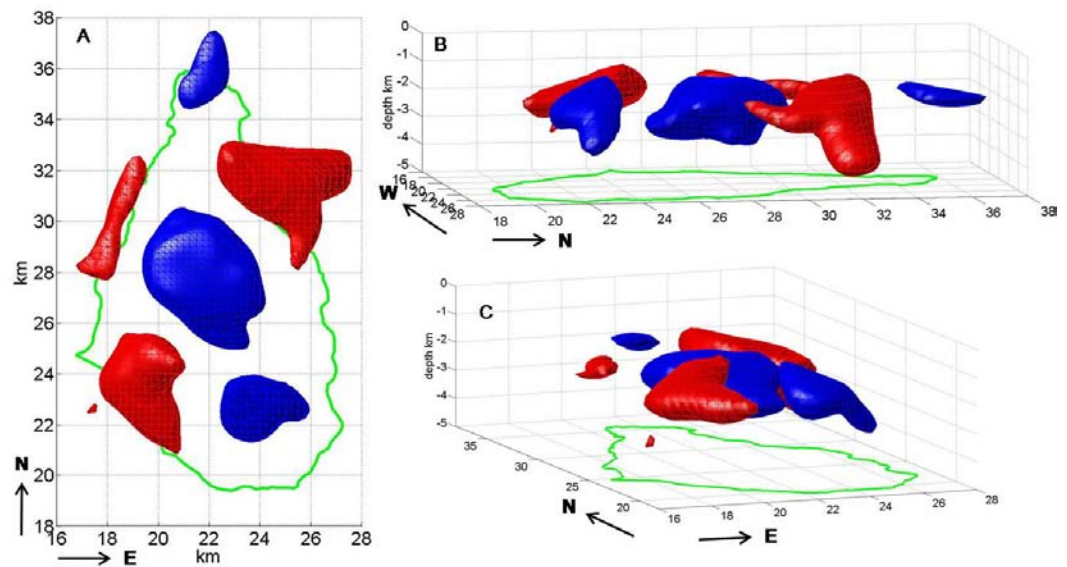
Appendix A: Figure 1.



Appendix A: Figure 2.



Appendix A: Figure 3.



Appendix A: Figure 4.

## References

- Acocella, V., Morvillo, P. and Funiciello, R., 2005. What controls relay ramps and transfer faults within rift zones? Insights from analogue models. *Journal of Structural Geology*, 27(3): 397-408.
- Andrews, D.W.K., 1986. A note on the unbiasedness of feasible GLS, quasi-maximum likelihood, robust, adaptive, and spectral estimators of the linear-model *Econometrica*, 54(3): 687-698.
- Armannsson, H., Gudmundsson, A. and Steingrímsson, B.S., 1987. Exploration and development of the Krafla geothermal area. *Jökull*, 37: 13-30.
- Aspinall, W.P. et al., 1998. Soufrière Hills eruption, Montserrat, 1995-1997: volcanic earthquake locations and fault plane solutions. *Geophysical Research Letters*, 25(18): 3397-3400.
- Barton, C.A., Zoback, M.D. and Moos, D., 1995. Fluid-flow along potentially active faults in crystalline rock. *Geology*, 23(8): 683-686.
- Chiarabba, C. and Moretti, M., 2006. An insight into the unrest phenomena at the Campi Flegrei caldera from Vp and Vp/Vs tomography. *Terra Nova*, 18(6): 373-379.
- Chiodini, G. et al., 1996. Fluid geochemistry of Montserrat Island, West Indies. *Bulletin of Volcanology*, 58(5): 380-392.
- Clarke, D., Townend, J., Savage, M.K. and Bannister, S., 2009. Seismicity in the Rotorua and Kawerau geothermal systems, Taupo Volcanic Zone, New Zealand, based on improved velocity models and cross-correlation measurements. *Journal of Volcanology and Geothermal Research*, 180: 50-66.
- Clifton, A. and Einarsson, P., 2005. Styles of surface rupture accompanying the June 17 and 21, 2000 earthquakes in the South Iceland Seismic Zone. *Tectonophysics*, 396: 141-159.
- Crampin, S., 1981. A review of wave motion in anisotropic and cracked elastic-media. *Wave Motion*, 3: 343-391.
- Crampin, S., 1993. A review of the effects of crack geometry on wave propagation through aligned cracks. *Canadian Journal of Exploration Geophysics*, 29: 3-17.



- Crampin, S. and Lovell, J.H., 1991. A decade of shear-wave splitting in the Earth's crust: what does it mean? what use can we make of it? and what should we do next? *Geophysical Journal International*, 107(3): 387-407.
- Crampin, S. and Peacock, S., 2005. A review of shear-wave splitting in the compliant crack-critical anisotropic Earth. *Wave Motion*, 41: 59-77.
- Cunningham, W.D. and Mann, P., 2007. Tectonics of strike-slip restraining and releasing bends. *Geological Society of London, Special Publications*, 290: 1-12.
- Curewitz, D. and Karson, J.A., 1997. Structural settings of hydrothermal outflow: Fracture permeability maintained by fault propagation and interaction. *Journal of Volcanology and Geothermal Research*, 79(3-4): 149-168.
- Davies, G.F., 1999. *Dynamic Earth*. Cambridge University Press, Cambridge, 458 pp.
- De Matteis, R. et al., 2008. Three-dimensional tomography and rock properties of the Larderello-Travale geothermal area, Italy. *Physics of the Earth and Planetary Interiors*, 168: 37-48.
- Delaney, P.T. et al., 1998. Volcanic spreading at Kilauea, 1976-1996. *Journal of Geophysical Research-Solid Earth*, 103(B8): 18003-18023.
- DeMets, C. et al., 2000. GPS geodetic constraints on Caribbean-North America plate motion. *Geophysical Research Letters*, 27: 437-440.
- Deng, Q., Daning, W., Zhang, P. and Chu, S., 1986. Structure and deformational character of strike-slip fault zones. *Pure and Applied Geophysics*, 124: 203-223.
- Deplus, C., Le Friant, A. and Boudon, G., 2001. Submarine evidence for large-scale debris avalanches in the Lesser Antilles Arc. *Earth and Planetary Sciences Letters*, 192(2): 145-157.
- Dewey, J.F., Holdsworth, R.E. and Strachan, R.A., 1998. Transpression and transtension zones. *Journal of the Geological Society, London*, 135: 1-14.
- Eberhart-Phillips, D. and Oppenheimer, D.H., 1984. Induced seismicity in The Geysers Geothermal Area, California. *Journal of Geophysical Research*, 89(B2): 1191-1207.
- Einarsson, P. and Eiriksson, J., 1982. Earthquake fractures in the district Land and Rangarvellir in the South Iceland Seismic Zone. *Jokull*, 32: 113-120.

- Feuillet, N. et al., 2010. Active faulting induced by slip partitioning in Montserrat and link with volcanic activity: New insights from the 2009 GWADASEIS marine cruise data. *Geophysical Research Letters*, 37(L00E15).
- Feuillet, N., Manighetti, I. and Tapponnier, P., 2001. Active extension perpendicular to subduction in the Lesser Antilles island arc (Guadeloupe, French Antilles). *Comptes Rendus de l'Académie des Sciences, Series IIA, Earth and Planetary Science*, 333(9): 583-590.
- Feuillet, N., Manighetti, I., Tapponnier, P. and Jacques, E., 2002. Arc parallel extension and localization of volcanic complexes in Guadeloupe, Lesser Antilles. *Journal of Geophysical Research*, 107(B12).
- Flude, S., McGarvie, D.W., Burgess, R. and Tindle, A.G., 2010. Rhyolites at Kerlingarfjoll, Iceland: the evolution and lifespan of silicic central volcanoes. *Bulletin of Volcanology*, 72: 523-538.
- Foulger, G.R. and Anderson, D.L., 2005. A cool model for the Iceland hotspot. *Journal of Volcanology and Geothermal Research*, 141(1-2): 1-22.
- Girardin, N., Feuillard, M. and Viode, J.P., 1991. Réseau régional sismique de l'arc des Petites Antilles: Sismicité superficielle (1981 - 1988). *Bull. Soc. Geol. Gr*, 162: 1003-1015.
- Gudmundsson, A., 2006. How local stresses control magma-chamber ruptures, dyke injections, and eruptions in composite volcanoes. *Earth-Science Reviews*, 79(1-2): 1-31.
- Gunasekera, R.C., Foulger, G.R. and Julian, B.R., 2003. Reservoir depletion at the Geysers geothermal area, California, shown by four-dimensional seismic tomography. *Journal of Geophysical Research*, 108(B3).
- Harford, C.L., Pringle, M.S., Sparks, R.S.J. and Young, S.R. (Editors), 2002. The volcanic evolution of Montserrat using  $^{40}\text{Ar}/^{39}\text{Ar}$  geochronology. *The Eruption of Soufrière Hills Volcano, Montserrat, from 1995 to 1999*, 21. Geological Society, London, Memoirs, London, 93-113 pp.
- Hautmann, S., Gottsmann, J., Antonio Camacho, A., Fournier, N. and Sparks, R.S.J., 2010. Volcano-tectonic stressing at Soufrière Hills Volcano, Montserrat, West Indies: Insights from 4-D gravity data. *Earth and Planetary Sciences Letters*, in press.

- Hautmann, S. et al., 2009. Modelling ground deformation caused by oscillating overpressure in a dyke conduit at Soufrière Hills Volcano, Montserrat. *Tectonophysics*, 471: 87-95.
- Hill, D.P., 1977. A model for earthquake swarms. *Journal of Geophysical Research*, 82(8): 1347-1352.
- Jones, A.G. and Dumas, I., 1993. Electromagnetic images of a volcanic zone. *Physics of the Earth and Planetary Interiors*, 81(1-4): 289-314.
- Kenedi, C.L., Shalev, E., Lucas, A. and Malin, P., 2010a. Microseismicity and 3-D mapping of an active geothermal field, Kilauea Lower East Rift Zone, Puna, Hawaii, World Geothermal Congress, Bali, Indonesia.
- Kenedi, C.L., Shalev, E., Malin, P., Kaleikini, M. and Dahl, G., 2008. Results from a borehole seismometer array I: Microseismicity at a productive geothermal field, Kilauea Lower East Rift Zone, Puna, Hawaii. *EOS Transactions AGU Fall Meeting Supplement*.
- Kenedi, C.L. et al., 2010b. Contrasts in morphology and deformation offshore Montserrat: New insights from the SEA-CALIPSO marine cruise data. *Geophysical Research Letters*, 37.
- Khodayar, M., Björnsson, S., Einarsson, P. and Franzson, H., 2010. Effect of tectonics and earthquakes on geothermal activity near plate boundaries: A case study from South Iceland. *Geothermics*, 39(3): 207-219.
- Klein, F.W., 2002. Hypocenter location program HYPOINVERSE-2000. U.S. Geological Survey Open File Report 02-171
- Le Friant, A. et al., 2010. Eruption of Soufrière Hills (1995–2009) from an offshore perspective: Insights from repeated swath bathymetry surveys. *Geophysical Research Letters*, 37: L11307.
- Le Friant, A. et al., 2009. Submarine deposition of volcanoclastic material from the 1995–2005 eruptions of Soufrière Hills Volcano, Montserrat. *Journal of the Geological Society, London*, 166: 1-12.
- Le Friant, A. et al., 2004. Geomorphological evolution of Montserrat (West Indies): importance of flank collapse and erosional processes. *Journal of the Geological Society, London*, 161: 147-160.



- Le Friant, A. et al., 2008. Late Pleistocene teprochronology of marine sediments adjacent to Montserrat, Lesser Antilles volcanic arc. *Journal of the Geological Society, London*, 165: 279-289.
- Leary, P., Malin, P., Shalev, E. and Onacha, S.A., 2010. Aquifer heterogeneity - is it properly assessed by wellbore samples and does it matter for aquifer heat extraction?, Australian Geothermal Energy Conference, Adelaide, Australia.
- Lees, J.M., 2007. Seismic tomography of magmatic systems. *Journal of Volcanology and Geothermal Research*, 167: 37-56.
- Lees, J.M. and Shalev, E., 1992. On the stability of P-wave tomography at Loma Prieta: A comparison of parameterizations, linear and non-linear inversions. *Bulletin of the Seismological Society of America*, 82(4): 1821-1839.
- Li, Y.-G., 1996. Shear wave splitting observations and implications on stress regimes in the Los Angeles basin, California. *J. Geophys. Res.*, 101(B6): 13947-13961.
- Lipman, P.W., Sisson, T.W., Coombs, M.L., Calvert, A. and Kimura, J.-I., 2006. Piggyback tectonics: Long-term growth of Kilauea on the south flank of Mauna Loa. *Journal of Volcanology and Geothermal Research*, 151(1-3): 73-108.
- Lippitsch, R., White, R.S. and Soosalu, H., 2005. Precise hypocenter relocation of microearthquakes in a high-temperature geothermal field: the Torfajökull central volcano, Iceland. *Geophysical Journal International*, 160: 370-387.
- Lou, M. and Rial, J.A., 1997. Characterization of geothermal reservoir crack patterns using shear-wave splitting. *Geophysics*, 62(2): 487-494.
- Lou, M., Shalev, E. and Malin, P.E., 1997. Shear-wave splitting and fracture alignments at the Northwest Geysers, California. *Geophysical Research Letters*, 24: 1895-1898.
- Loughlin, S., 2010. An overview of lava dome evolution, dome collapse and cyclicity at Soufrière Hills Volcano, Montserrat: 2005 - 2007. *Geophysical Research Letters*, 37(L00E16).
- Lucas, A., Shalev, E., Malin, P.E. and Kenedi, C.L., 2010. Using earthquake clusters to identify fracture zones at Puna geothermal field, Hawaii, AGU Fall Meeting, 2010. EOS, San Francisco, CA, USA.

- Marsh, B., Teplow, W., Reagan, M. and Sims, K., 2008. Puna Dacite: Likely Temperature, Viscosity, origin, size, and parent body nature. *EOS Transactions AGU Fall Meeting Supplement*, 89(53).
- Miller, V., Voight, B., Ammon, C.J., Shalev, E. and Thompson, G., 2010. Seismic expression of magma-induced crustal strains and localized fluid pressures during initial eruptive stages, Soufriere Hills Volcano, Montserrat. *Geophysical Research Letters*, 37.
- Moore, R.B. and Trusdell, F.A., 1991. Geologic map of the Lower East Rift Zone of Kilauea Volcano, Hawaii, U.S. Geological Survey Miscellaneous investigations series, pp. map I-2225.
- Morgan, J.K., Moore, G.F. and Clague, D.A., 2003. Slope failure and volcanic spreading along the submarine south flank of Kilauea volcano, Hawaii. *Journal of Geophysical Research-Solid Earth*, 108(B9).
- Nielson, D.L., Forster, C. and Caine, J., 1996. Investigations of fractures in high-temperature geothermal systems, Geothermal Program Review XIV: Keeping Geothermal Energy Competitive in Foreign and Domestic Markets. U.S. Department of Energy.
- Oglesby, D.B., 2005. The dynamics of strike slip step-overs with linking dip-slip faults. *Bulletin of the Seismological Society of America*, 95: 1604-1622.
- Onacha, S.A., 2006. Hydrothermal fault zone mapping using seismic and electrical measurements. PhD Dissertation Thesis, Duke University, Durham, NC, 225 pp.
- Owen, S. et al., 1995. Rapid deformation of the south flank of Kilauea Volcano, Hawaii. *Science*, 267(5202): 1328-1332.
- Owen, S.E. and Burgmann, R., 2006. An increment of volcano collapse: Kinematics of the 1975 Kalapana, Hawaii, earthquake. *Journal of Volcanology and Geothermal Research*, 150(1-3): 163-185.
- Parfitt, E.A. and Peacock, D.C.P., 2001. Faulting in the South Flank of Kilauea Volcano, Hawai'i. *Journal of Volcanology and Geothermal Research*, 106(3-4): 265-284.
- Paulatto, M. et al., 2010. Upper crustal structure of an active volcano from refraction/reflection tomography, Montserrat, Lesser Antilles. *Geophysical Journal International*.

- Peacock, D.C.P., Knipe, R.J. and Sanderson, D.J., 2000. Glossary of normal faults. *Journal of Structural Geology*, 22(3): 291-305.
- Peacock, D.C.P. and Parfitt, E.A., 2002. Active relay ramps and normal fault propagation on Kilauea Volcano, Hawaii. *Journal of Structural Geology*, 24(4): 729-742.
- Powell, C.F., 1938. The Royal Society expedition to Montserrat, B. W. I. Final Report. *Philosophical Transactions of the Royal Society of London*, 237(771): 1-34.
- Prejean, S., Ellsworth, W., Zoback, M. and Waldhauser, F., 2002. Fault structure and kinematics of the Long Valley Caldera region, California, revealed by high-accuracy earthquake hypocenters and focal mechanism stress inversions. *Journal of Geophysical Research*, 107(B12).
- Prejean, S., Stork, A., Ellsworth, W., Hill, D. and Julian, B., 2003. High precision earthquake locations reveal seismogenic structure beneath Mammoth Mountain, California. *Geophysical Research Letters*, 30(24).
- Rea, W.J., 1974. The volcanic geology and petrology of Montserrat, West Indies. *Journal of the Geological Society, London*, 130: 341-366.
- Rial, J.A., Elkibbi, M., Yang, M., 2005. Shear-wave splitting as a tool for the characterization of geothermal fractured reservoirs: lessons learned. *Geothermics*, 34: 365-385.
- Roman, D.C., De Angelis, S., Latchman, J.L. and White, R., 2008. Patterns of volcanotectonic seismicity and stress during the ongoing eruption of the Soufrière Hills Volcano, Montserrat (1995-2007). *Journal of Volcanology and Geothermal Research*, 173(3-4): 230-244.
- Rowland, J.V. and Sibson, R.H., 2004. Structural controls on hydrothermal flow in a segmented rift system, Taupo Volcanic Zone, New Zealand. *Geofluids*, 4(4): 259-283.
- Ryan, G., Onacha, S.A., Shalev, E. and Malin, P.E., 2009. Imaging the Montserrat geothermal prospect using magnetotelluric (MT) and time domain electromagnetic induction (TDEM) measurements, Institute of Earth Science and Engineering, University of Auckland, New Zealand.
- Saemundsson, K. and Johannesson, H., 2003. Geothermal map of Iceland. Iceland Geo-Survey and National Energy Authority, Reykjavik.

- Shalev, E., Kenedi, C.L. and Malin, P., 2008. Results from a borehole seismometer array II: 3-D mapping of an active geothermal field at the Kilauea Lower East Rift Zone. EOS Transactions AGU Fall Meeting Supplement, 89(53).
- Shalev, E., Kenedi, C.L., Malin, P. and Lou, M., in preparation. Crack-density tomographic inversion in Long Valley Caldera, and Geysers, California.
- Shalev, E. et al., 2010. Three-dimensional seismic velocity tomography of Montserrat from the SEA-CALIPSO offshore/onshore experiment. Geophysical Research Letters, 37.
- Shalev, E. and Lees, J.M., 2004. Three dimensional tomographic analysis of the Loma Prieta region. In: R.E. Wells (Editor), *The Loma Prieta, California, Earthquake of October 17, 1989 - Geologic Setting and Crustal Structure*. U.S. Geological Survey, Reston, VA, pp. 127-142.
- Shepherd, J.B., Tomblin, J.F. and Woo, D.A., 1971. Volcano-seismic crisis in Montserrat, West Indies, 1966-67. Bulletin volcanologique, 35(1): 143-163.
- Sibson, R.H., 1996. Structural permeability of fluid-driven fault-fracture meshes. Journal of Structural Geology, 18(8): 1031-1042.
- Sibson, R.H., 2000. Fluid involvement in normal faulting. Journal of Geodynamics, 29(3-5): 469-499.
- Sibson, R.H., 2001. Seismogenic Framework for Hydrothermal Transport and Ore Deposition. Society of Economic Geologists Reviews, pp. 25-50.
- Tang, C., Rial, J.A. and Lees, J.M., 2008. Seismic imaging of the geothermal field at Krafla, Iceland using shear-wave splitting. Journal of Volcanology and Geothermal Research: 315-324.
- Teplow, W. et al., 2008. Dacite melt at the Puna Geothermal Venture Wellfield, Big Island of Hawaii. EOS Transactions AGU Fall Meeting Supplement, 89(53).
- Trofimovs, J. et al., 2006. Submarine pyroclastic deposits formed at the Soufrière Hills Volcano, Montserrat (1995-2003); what happens when pyroclastic flows enter the ocean? Geology, 34: 549-552.
- Trofimovs, J. et al., 2009. Evidence for carbonate platform failure during rapid sea-level rise; ca 14000 year old bioclastic flow deposits in the Lesser Antilles. Sedimentology.

- Trusdell, F.A., Novak, E. and Evans, S.R., 1993. Core lithology State of Hawaii scientific observation hole 4, Kilauea Volcano, Hawaii.
- Voight, B. et al., 2010. Active-source seismic experiment peers under Soufrière Hills Volcano. EOS, Transactions, American Geophysical Union, 91(28).
- Waldhauser, F., 2001. hypoDD: A program to compute double-difference hypocenter locations.
- Waldhauser, F. and Ellsworth, W.L., 2000. A double-difference earthquake location algorithm: Method and application to the northern Hayward fault, California. Bulletin of the Seismological Society of America, 90(6): 1353-1368.
- Weber, J.C. et al., 2001. GPS estimate of relative motion between the Caribbean and South American plates, and geologic implications for Trinidad and Venezuela. Geology, 29: 75-78.

# Biography

## Catherine Lewis Kenedi

Born: Hartford, Connecticut, February, 7, 1970

M.S. University of Michigan Geological Sciences 2003

B.A. Wesleyan University Comparative Religions 1993 Phi Beta Kappa

Kenedi, C. L., R.S.J. Sparks, P. Malin, B. Voight, S. Dean, T. Minshull, M. Paulatto, C. Peirce, and E. Shalev (2010), Contrasts in morphology and deformation offshore Montserrat: New insights from the SEA-CALIPSO marine cruise data, *Geophys. Res. Lett.* 37

Kenedi, C.L., Shalev, E., Lucas, A., and Malin, P. (2010) Microseismicity and 3-D Mapping of an Active Geothermal Field, Kilauea Lower East Rift Zone, Puna, Hawaii. Proceedings of the World Geothermal Congress, Bali, Indonesia.

Lewis-Kenedi C.B., Lange R.A., Hall C.M., Delgado-Granados H. (2004) The eruptive history of the Tequila volcanic field, western Mexico: ages, volumes, and relative proportions of lava types. *Bulletin of Volcanology*, 67: 5, 391 - 414.

Malin P.E., Shalev E., Balven H., Lewis-Kenedi C. (2006) Structure of the San Andreas Fault at SAFOD from P-wave tomography and fault-guided wave mapping. *Geophysical Research Letters*, 33. L13314, doi:10.1029/2006GL025973.

Paulatto, M., T. A. Minshull, B. Baptie, S. Dean, J. O. S. Hammond, T. Henstock, C. L. Kenedi, E. J. Kiddle, P. Malin, C. Peirce, G. Ryan, E. Shalev, R. S. J. Sparks and B. Voight (2010), Upper crustal structure of an active volcano from refraction/reflection tomography, Montserrat, Lesser Antilles, *Geophys. J. International*, doi: 10.1111/j.1365-246X.2009.04445.x.

Shalev, E., Kenedi, C.L., Malin, P., Voight, B., Miller, V., Hidayat, D., Sparks, R.S.J., Minshull, T., Paulatto, M., Brown, L., Mattioli, G. (2010), Three-dimensional seismic velocity tomography of Montserrat from the SEA-CALIPSO offshore/onshore experiment, *Geophys. Res. Lett.* 37, L00E17, doi:10.1029/2010GL042498

Voight, B., Sparks, R. S. J., Hammond, J. O. S., Shalev, E., Malin, P., Kenedi, C. L., Minshull, T., Paulatto, M., Mattioli, G. S., Hidayat, D., Widiwijayanti, C. (2010). Active-source seismic experiment peers under Soufrière Hills Volcano. *EOS, Transactions, American Geophysical Union*, 91:28, 245-247.

Geologic guide to Yellowstone National Park for the National Park Service (1997).

Phi Beta Kappa Honor Society 1993

Sigma Xi Honor Society 2006

Turner Award, University of Michigan